Max-Planck-Institut
für Kolloid- und Grenzflächenforschung

Universität Potsdam

Microfluidics for the study of magnetotactic bacteria
Towards single-cell analysis

Dissertation

zur Erlangung des akademischen Grades
"doctor rerum naturalium"
(Dr. rer. nat.)
in der Wissenschaftsdisziplin Physikalischen Chemie

von

Elisa Cerdá Doñate

eingereicht an der
Mathematisch-Naturwissenschaftlichen Fakultät
Institut für Chemie
der Universität Potsdam

und

Abteilung Biomaterialien
der Max-Planck-Institut für Kolloid- und Grenzflächenforschung

Datum der Disputation: 24. Juni 2020

Hauptbetreuer:	Dr. Damien Faivre
Betreuer:	Dr. Tom Robinson
Gutachter:	Dr. Ilko Bald
	Dr. Jean-Christophe Baret

Zusammenfassung

Magnetotaktische Bakterien gehören einer heterogenen Gruppe gramnegativer Bakterien an, welche die Fähigkeit zur Synthese intrazellulärer magnetischer Nanopartikel teilen. Diese Partikel, genannt Magnetosomen, sind von einer Doppellipidschicht umgeben und ordnen sich in linearen Ketten an. Die Bakterien haben ein einzigartiges Maß an Kontrolle über die Biomineralisation dieser Nanopartikel, welche sich in der genau bestimmten Größe und Form zeigt. Diese besonderen Eigenschaften haben die Aufmerksamkeit auf ein besseres Verständnis der Magnetosomensynthese durch die Bakteriengezogen. Darüber hinaus besitzen die Bakterien durch die Magnetosomenkette ein magnetisches Dipolmoment, welches sie befähigt auf ein Magnetfeld zu reagieren, wodurch sie sich im Magnetfeld der Erde ausrichten können. Auch diese Eigenschaft hat großes Interesse geweckt, besonders um den Einfluss eines Magnetfeldes auf das Schwimmverhalten der Mikroorganismen besser zu verstehen.

Die meisten bisherigen Studien an diesen Organismen wurden in klassischen Systemen mit großen Populationen durchgeführt. Solche Studien haben den Nachteil, dass das heterogene Verhalten vieler verschiedener Individuen gemittelt wird und daher individuelle Variationen nicht berücksichtigt werden. Zusätzlich ist jedes einzelne Bakterium einer großen Population einer anderen Mikroumgebung ausgesetzt, welche sein Verhalten beeinflusst, das aber durch die Verwendung traditioneller Methoden nicht erfasst werden kann. In dieser Arbeit werden verschiedene mikrofluidische Plattformen vorgestellt, um diese Einschränkungen zu überwinden und die Möglichkeit zu bieten, sogar einzelne magnetotaktische Bakterien in einer definierten Umgebung studieren zu können.

Als erstes wird eine Sediment-ähnliche mikrofluidische Plattform vorgestellt, die den Zweck hat, die natürliche poröse Umgebung der Bakterien zu imitieren. Die Plattform erlaubt es mit Hilfe von Durchlichtmikroskopie zu sehen, dass Bakterien in einer gedrängten Umgebung eine verbesserte Navigation im Bereich der Erdmagnetfeldstärke ($B = 50\,\mu T$) haben, im Vergleich zu keinem ($B = 0\,\mu T$) oder einem höheren Magnetfeld ($B = 50\mu T$).

Zweitens wurde ein mikrofluidisches System zum Eingrenzen einzelner Bakterien in einer physisch definierten Umgebung entwickelt. Das System erlaubt mit Hilfe von Durchlichtmikroskopie die Untersuchung des Einflusses und des Zusammenspiels von Wandkrümmung, Magnetfeld und Bakteriengeschwindigkeit auf die Bewegung eines eingegrenzten Bakteriums und zeigt, wie die Bewegungspfade der Bakterien von diesen drei Faktoren abhängen.

Drittens wurde eine mikrofluidische Plattform hergestellt, die die Durchführung von semi *in-vivo* Magnetosomenkeimbildung mit einer Auflösung von einzelnen Zellen mittels Röntgenfluoreszenz ermöglicht. Signale, welche von einer kompletten Magnetosomenkette herrühren, können in individuellen Bakterien beobachtet werden.

Abschließend wurde die Kinetik der Eisenaufnahme eines einzelnen Bakteriums durch einen fluoreszierenden Reporter mit Hilfe von konfokaler Mikroskopie untersucht. Zwei verschiedenen Ansätze wurden dabei verwendet: eine der bereits vorgestellten Plattformen, sowie riesige Lipidvesikel. Es wurde beobachtet, dass die Eisenaufnahmerate zwischen verschiedenen Zellen variiert und wie sich damit übereinstimmend Magnetosomen innerhalb von Stunden bilden.

Diese Arbeit zeigt damit wie mikrofluidische Technologien für die Untersuchung magnetotaktischer Bakterien in unterschiedlichen Bereichen eingesetzt werden können, und welches Level an Auflösung erreicht werden kann, indem mit einzelnen Zellen gearbeitet wird.

Abstract

Magnetotactic bacteria comprise a heterogeneous group of Gram negative bacteria which share the ability to synthesise intracellular magnetic nanoparticles surrounded by a lipid bilayer, known as magnetosomes, which are arranged in linear chains. The bacteria exert a unique level of control onto the biomineralization of these nanoparticles, which is seen in the controlled size and shape they have. These characteristics have attracted great attention on understanding the process by which the bacteria synthesise the magnetosomes. Moreover, the magnetosome chain impart the bacteria with a net magnetic dipole which makes them susceptible to interact with magnetic fields and thus orient with the Earth's magnetic field. This feature has attracted as well much interest to understand how the swimming motility of these microorganisms is affected by the presence of magnetic fields.

Most of the studies performed in these bacteria so far have been conducted in the traditional manner using large populations of cells. Such studies have the disadvantage of averaging many different individuals with heterogeneous behaviours and fail to consider individual variations. In addition, in large populations each bacterium will be subjected to a different microenvironment that will influence the bacterial behaviour, but which cannot be defined using these traditional methods. In this thesis, different microfluidic platforms are proposed to overcome these limitations and to offer the possibility to study magnetotactic bacteria in defined environments and down to a single-cell resolution.

First, a sediment-like microfluidic platform is presented with the purpose of mimicking the porous environment they bacteria naturally dwell in. The platform allows to observe via transmitted light microscopy that bacterial navigation in crowded environments is enhanced by the Earth's magnetic field strengths (B = 50 μT) rather than by null (B = 0 μT) or higher magnetic fields (B = 500 μT).

Second, a microfluidic system to confine single-bacterial cells in physically defined environments is presented. The system allows to study via transmitted light microscopy the interplay between wall curvature, magnetic fields and bacterial speed affect the motion of a confined bacterium, and shows how bacterial trajectories depend on those three parameters.

Third, a microfluidic platform to conduct semi *in vivo* magnetosome nucleation with a single-cell resolution via X-ray fluorescence is fabricated. It is shown that signal arising from magnetosome full chains can be observed individually in each bacterium.

Finally, the iron uptake kinetics of a single bacterium are studied via a fluorescent reporter through confocal microscopy. Two different approaches are used for this: one of the previously mentioned platforms, as well as giant lipid vesicles. It is observed how iron uptake rates vary between cells, as well as how these rates are consistent with magnetosome formation taking place within some hours.

The present thesis shows therefore how microfluidic technologies can be implemented for the study of magnetotactic bacteria at different degrees, and the level of resolution that can be attained by going into the single-cell scale.

Acknowledgments

It is simply not possible to hand in this thesis without briefly mentioning those who made this thesis possible. First of all, I have to thank Damien Faivre and Tom Robinson for allowing me to have undertaken this journey where I came to meet magnetotactic bacteria and microfluidics, as well the IMPRS doctoral school for funding my project. Also, a special mention to PDMS. I still can't figure out whether it has been part of this thesis, or if it was actually the thesis itself. In any case, you have nested the most ambiguous feelings in me.

Thanks as well to everyone I have come across in Damien's and Tom's groups for contributing to a wonderful time in the lab: lab work in good company is certainly something to appreciate. Same applies to collaborations: special thanks to Agnesito, Mohammad and Dan; working with you has definitely been a pleasure. Special thanks as well to Mathieu and Felix, not to have broken the Helmholtz coils microscope on my head. Your patience has probably granted you canonization. Special thanks as well to the wonderful office mates I have had the pleasure to share the office with: Sara, Matthias and Chuang. You have made office time simply great. Another big Dankeschön to Christine, I cannot thank you for all the dedication you have put into the lab and all the help.

And, of course, to all of you who have made life sunnier in that ridiculously sunny and vibrant place called Golm: Morenito, Morenito, Morenito, Patricia, Patricia, Patricia, Agnesito, JC and the thesis police, Melisandre, Don José, Rikhiachen, Ana, Alessandro, Eddie, Emilia, Alberto, Inés, Alex, Chuang, Sarahyán, Anna Pohl, Dionís, César, Erika… You have made this thesis be forged among diamonds to be polished, little forests, ponqués, biotechnologies and ethymologies, killer tomatoes, novas eras per l'astronomia, brócolis reivindicadores and Luftballoons. A big gracias as big as from Castellón to Frankfurt (Oder).

And finally, thanks as well to my family for their infinite questions of "But what do you exactly do, then?" and faces confessing "Why did we even ask the question? Will someone make her shut up, please?", and all those "But when do you come back home?", "But you are done with your thesis, right?" going over one year, and the almighty "Is that actually useful?", even though my favourite remains my grandmother's "But do you seriously receive a salary for being the whole day playing inside a laboratory? What a nonsense". And of course, le Mochito had to be here as well, even though he won't appreciate it because he believes this section is ridiculously pointless. Tut mir leid, pero estás aquí. He has found this thesis una problemación a la par que un sufrecimiento, but him and Pablito (whose smile is eternal) have deserved an invitation to an Asian restaurant (well, not Pablito because he always finishes the biscuits) as they have made days brighter (even though the word nanobactéries makes you lose points). And also thanks to a mother-in-law who has made sure all this time that not a single thing was missing in our flat.

PS.: A fairly indecent amount of *Magnetospirillum gryphiswaldense* cells were sacrificed during the course of this thesis. Thank you, guys, for not rebelling too much against me.

Table of contents

List of figures

List of tables

List of abbreviations

BSA	Bovine serum albumine
CAD	Computer aided design
CCW	Counterclockwise
CW	Clockwise
DiD	1,1'-dioctadecyl-3,3,3',3'-tetramethylindodicarbocyanine
DNA	Deoxyribonucleic acid
EDTA	Ethylenediaminetetraacetic acid
FAD	Flavin adenine dinucleotide
FMN	Flavin mononucleotide
GM	Growth medium
GOPTS	(3-glycidyloxypropyl)trimethoxysilane
GUV	Giant unilamellar lipid vesicle
HEPES	4-(2-hydroxyethyl)-1-piperazineethanesulfonic acid
ICP	Inductively coupled plasma
LUV	Large unilamellar lipid vesicle
MAI	Magnetosome island
microCT	Micro–computed tomography
MS	Mass spectrometry
MTB	Magnetotactic bacteria
NADH	Nicotinamide adenine dinucleotide
NADPH	Nicotinamide adenine dinucleotide phosphate
OATZ	Oxic-anoxic transition zone
OD	Optical density
PBS	Phosphate-buffered saline
PDMS	Polydimethylsiloxane
PE	Phosphatidylethanolamine
PEG	Polyethylene glycol
PFTE	Polytetrafluoroethylene
PLL	Polylysine
PMMA	Poly(methyl methacrylate)
POPC	1-palmitoyl-2-oleoyl-glycero-3-phosphocholine
PVA	Polyvinyl alcohol

RCF	Relative centrifugal force
RT	Room temperature
SUV	Small unilamellar lipid vesicle
TEM	Transmission electron microscopy
UV	Ultraviolet
XRF	X-ray fluorescence

1. Introduction

1.1. Biomineralisation and magnetotactic bacteria

Biomineralization can be described as the process by which living organisms are able to generate minerals [1]. Far from being an exception in nature, such process can be found in the three biological domains (Eukarya, Bacteria and Archaea). It often involves a protective or supportive function within the organism, e.g. bones or shells, and is most commonly mediated by calcium. However, other elements, such as iron, are also key players in certain biomineralization processes which we shall address in the present study, and play different roles in the organism [2].

The biomineralization process represents the paradigm of how organic elements can control the assembly of inorganic structures with precisions which reach the nanoscale level. Not only the precision of such processes has generated great interest in the materials science field, but also the fact that many of the biomineral phases are not encountered naturally isolated from organic matter as they are thermodynamically less favoured than other naturally-occurring minerals [3].

Magnetotactic bacteria (MTB) were first reported in 1963 [4], rediscovered in 1975 [5], and have since been an object of study due to their remarkable ability to synthesise strings of intracellular iron oxide and sulphide, namely magnetite and greigite (Figure 1). These are single-domain nanoparticles, individually enveloped by a lipid bilayer, known as magnetosomes [6, 7]. Interestingly, this ability to synthesise the magnetosome chain is biochemically orchestrated as it is genetically controlled by a set of genes known as the magnetosome island (MAI) [8, 9]. MTB are not limited to a single species nor a single phylum, but are phylogenetically diverse, being found in different phyla, such as Proteobateria, Nitrospirae, and Omnitrophica [10]. However, all known MTB share the ability to swim and live within the sediment. Their magnetosome chains provide them with a net magnetic dipole that allows it to orient with the Earth's magnetic field, which helps the bacteria to navigate the sediment to find its preferred oxic conditions [5]. Despite the fact that all know MTB are aquatic swimming organisms and that all bear a magnetosome island within their genomes, it is remarkable that the synthesis of magnetosomes is species-specific [11]. Each species synthesises magnetosomes with a precise shape [12] and within a very narrow size range [12], indicating that the bacterium specific machinery exerts a high degree of control over the biomineralisation process [13].

The fact that such "simple" organisms are able to control the synthesis of magnetosomes with such a degree of precision, makes them an ideal candidate to study at its simplest the different mechanisms that govern the biomineralisation process, and how it impacts the behaviour of the microorganism. Traditionally, both the MTB swimming [5, 14-16] as well as the magnetosome biomineralisation have usually been studied in bulk [8, 17-19]. However, bulk studies fail to recognise population heterogeneities as individual variations are masked by population averages. For example, as observed by TEM images, it is known that, within a same culture, not all MTB are able to synthesise magnetosomes [8]; yet, when studying magnetosome production or iron uptake, it is

considered that all cells are equal, resulting in a lack of knowledge on whether the iron uptake takes place in a discrete on/off way with constant values, or rather in a continuous manner spanning over a range of rates. Such scenarios cannot be answered while cells are not assessed individually. Nevertheless, standard laboratory techniques have usually relied in the use of cell population measurements for decades, meaning that the gold standards do not target single-cells heterogeneities, but populations in a homogeneous manner. Therefore, if a higher level of variability within a bacterial population is to be acquired, new techniques and platforms are to be made available for such studies which target single bacterial cells. The present thesis proposes a series of new platforms to study MTB at the single-cell scale by using an alternative strategy to the standard ones used for MTB, namely microfluidics.

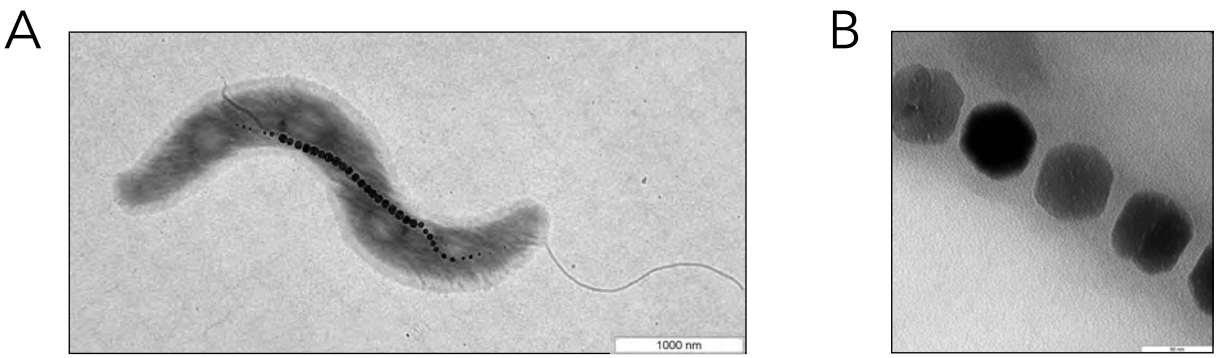

Figure 1. Transmission electron microscopy (TEM) images of *M. gryphiswaldense* MSR-1. The first image shows one bacterium harbouring a magnetosome chain (A), whereas (B) shows a more detailed image of the magnetosomes.

1.2. Microfluidics

Microfluidics refers to the science dealing with fluids constrained in micrometer-sized environments [20], which emerged during the late 80s and early 90s [21-25], taking advantage of the advances made in the microelectronics industry, from which the fabrication techniques had been borrowed and on the basis of which they have been developed. Since its origins, microfluidic research has blossomed and has been applied to various areas, having been used for basic and applied research in the fields of biology [26], chemistry [27] and physics [28]. In the field of biology, microfluidic systems have been developed to study antibiotic resistances [29], cell division [30], chemotaxis [31], as well as applied for the fabrication of DNA microarrays [32], protein crystallisation platforms [33] to glucose detection systems [34], to name just a few examples.

In contrast to the macroscale world, microfluidics takes advantage of a series of effects that become apparent in the microscale, when diffusion starts dominating over convection and surface effects start becoming non-negligible. A key feature of microfluidics is that liquid flows in the laminar regime, being characterised by low Reynolds numbers, which describes the dominance of inertial forces to viscous forces. This gives rise to defined flow trajectories that can be easily predicted, in contrast to turbulent regimes, characterised by high Reynolds numbers, which result in instabilities (Figure 2). This allows the creation of defined chemical gradients in the microchannels. Other features that characterise microfluidics rely on the miniaturisation possibilities that these

systems offer, allowing for simple storage, as well as the low reagent consumption taking place in these systems due to the small volumes used. In addition, they offer multiplexing capabilities, i.e. the ability to perform parallelised measurements. Moreover, these systems allow an increased control not only in the flow paths, but also in other useful parameters, such as temperature or dissolved molecule concentration gradients.

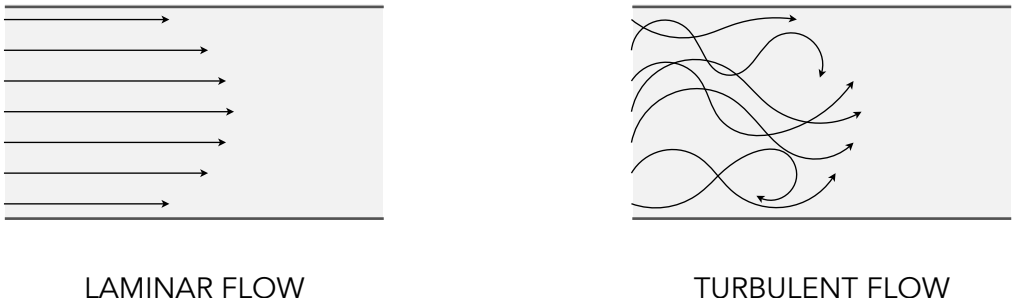

Figure 2. Streamlines for a laminar and a turbulent flow. The sketch shows a laminar flow inside a channel (left), where streamlines advance in an ordered predictable manner, in contrast to a turbulent flow (right), where streamlines are not predictable.

On terms of fabrication, the manufacture of microfluidic devices is as diverse as the applications which they are meant for, as each project will call for a series of requirements that will impact on the final characteristics of the device and, inevitably, on the materials used. Such characteristics range from the transparency of the material, to its compatibility to solvents, porosity, permeability, flexibility, stability, machinability, integrability, automatisation and cost. Suitable for these requirements, many different materials have been implemented in microfluidic platforms, ranging from traditional materials, such as silicon [35] and glass [36], to polymers, such as PMMA [37] or SU-8 [38], to hydrogels [39] and even paper [40]. However, if one material has become the gold standard in microfluidics, it is PDMS [41], a silicon rubber, due to its easy implementation as well as its ability to create rapid prototypes. Moreover, the optical transparency of this material to visible light, its simple coupling to glass surfaces, its flexibility, its gas permeation characteristics and its biocompatibility have led to its use as a standard material for the development of new platforms in the life sciences field.

In this thesis, different microfluidic platforms are developed to suit several needs dealing with the study of MTB cells at different levels, ranging from the physical to the chemical microenvironment, with a special focus on the single-cell scale. These platforms enable the investigation of their swimming behaviour as well as their iron uptake at a resolution that cannot be obtained by standard bulk methods. Throughout the chapters of this thesis, it will be shown how, starting from a very simple microsystem, it is possible to modify different features which result in fairly different and versatile platforms. For this, traditional materials (glass and PDMS) will be mainly used, even though alternative options will be presented as well. It will also be discussed where popular and established gold standards can become limiting, and what alternative platforms can offer.

The structure that follows this introduction is arranged as follows. First, the specific objectives of this work are specified. Then, a general materials and methods section with the general background common to all the microsystems is given. After this, five chapters are presented, each one detailing a microfluidic platform for a given purpose, after which the thesis concludes with a general discussion and conclusion.

2. Objectives

The scope of this thesis was to develop a series of microfluidic platforms to study different aspects of the microenvironment of *Magnetospirillum gryphiswaldense* MSR-1 at the single-cell scale. Therefore, the ultimate goal of this thesis was to develop platforms to perform measurements on this organism with a finer level of precision compared to previous bulk measurements.

This general aim is divided in the following specific objectives:

1. Development of a microfluidic platform that mimics the physical microenvironment that magnetotactic bacteria encounter in their natural environment (the sediment).

2. Development of a microfluidic platform to study the dynamics of magnetosome formation at the single-cell scale through X-ray fluorescence, that is, studying the inner bacterial chemical microenvironment.

3. Development of a microfluidic platform to study iron uptake in magnetotactic bacteria by fluorescently monitoring the outer chemical microenvironment.

4. Determination of the iron uptake kinetics of *M. gryphiswaldense* MSR-1 at the single-cell scale using micrometer-sized compartments (i.e. lipid vesicles).

3. General materials and methods

In this section the general materials and methods used during the entire thesis are explained. However, for specific details or variations that are not shared among the different platforms, please refer to the *Materials and methods* sections of each chapter. This section mainly refers to the bacterial culture methods, the microsystem fabrication, and the general microscopy settings. The materials are indicated at the beginning of each method section.

3.1. Bacterial culture

For the MSR-1 growth medium preparation all chemicals were purchased from Roth. (Germany), except for calcein, which was acquired from Merck (Merck). The bacterial strain used throughout this thesis was *Magnetospirillum gryphiswaldense* MSR-1. However, different culture conditions were used for different experiments, namely different temperatures, shaking speeds, medium composition, containers and volumes. The culture conditions are briefly explained below, whereas their exact composition and parameters is summarised in Table 1 to facilitate their comparison. The purpose of each growth medium formulation as well as the specific details can be found in the following lines.

Independently of the method used to grow the bacteria, the bacterial growth was determined by reading the optical density of the suspensions at λ = 565 nm (OD_{565}). Cell magnetism was estimated by measuring the C_{mag} ('coefficient of magnetically induced differential light scattering') parameter (Figure 3). The C_{mag} parameter was first introduced in 1995 [42] and relies on how light is scattered depending on the orientation of the cells in relation to the direction of a light beam (Figure 3). Additionally, cell magnetism and potential contaminations were evaluated by visualising the bacteria in the optical microscope and placing a magnet next to them to observe their swimming direction.

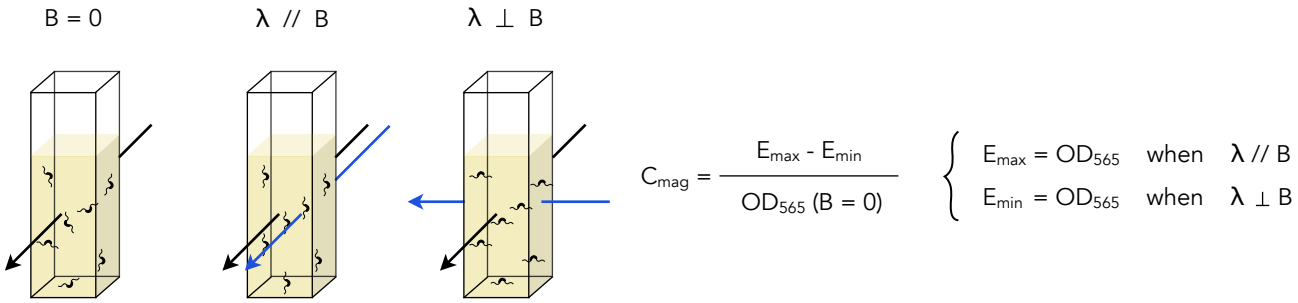

Figure 3. Measurement of the C_{mag} parameter. Sketch showing the measurement of the bacterial optical density without the presence of a magnetic field (OD_{565}), with a magnetic field parallel to the spectrophotometer light path (E_{max}), and perpendicular to the light path (E_{min}). The magnetic field is created by placing a magnet above the cuvette. The C_{mag} parameter is calculated by dividing the difference in optical densities in the presence of a parallel and a perpendicular magnetic field by the optical density when no field is present.

Standard growth medium

MSR-1 standard growth medium was prepared with the reagents indicated in Table 1 and 2 [43], and was used as routine culture composition. The pH of the medium was adjusted to 7.0 with NaOH. The medium was then distributed in anaerobic Hungate culture tubes of 14 mL capacity, filling them with 10 mL of growth medium each and leaving the remaining 4 mL empty. Since *M. gryphiswaldense* is a microaerophilic microorganism, the medium in each test tube was degassed with a mixture of 99% N_2+ 1% O_2 to create microaerobic conditions. Right after degassing the test tubes, they were sealed with both rubber and screw taps, and were subsequently autoclaved.

Agar-supplemented growth medium

This growth medium is analogous to the standard MSR-1 growth medium, but is supplemented with 0.1% agarose to jellify the medium, so that it is possible to select for bacterial swimmers through the creation of an aerotactic band. Typically, bacteria are inoculated at the bottom of the tube and an O_2 gradient is allowed to form. The bacteria will form an aerotactic band, which is then re-inoculated at the bottom of another agar-supplemented tube. This second band is then cultured in standard growth medium; bacteria grown in these conditions are used for the motility studies.

Low iron growth medium

To devoid the bacteria of magnetosomes, low iron growth medium was prepared in an analogous way to the standard MSR-1 growth medium, but omitting any iron source (Fe(III)-citrate, trace elements, soya peptone and yeast extract). Bacteria are passaged twice in this medium to create an iron starvation state.

Microwell growth medium

To perform the fluorescent assay, low iron growth medium supplemented with $FeCl_3$ to 50 μM and calcein to 25 μM was used. This medium was sterilized-filtered as autoclaving could have compromised calcein stability.

GUV growth medium

For the GUVs, a growth medium analogous to the microwell growth medium, but supplemented with PVA up to 1% (w/v) was used. PVA was used as densifying agent, as explained in *Chapter 8*. This growth medium was filter-sterilised previous to the addition of PVA; and PVA was homogenised by vortexing.

3.2. Microfluidic system design and and fabrication

For the design of microfluidic systems, the software AutoCAD 2015 was used. For the fabrication of the master moulds, silicon wafers (100 mm diameter, 525 μm thickness) were purchased from Siegert Wafer (Aachen, Germany); film masks from Microlitho (Essex, UK); the chrome mask from Compugraphics (Jena, Germany); the photoresist SU-8 3010 from MicroChem Inc. (Germany); the developer mr-Dev 600 from Microresist Technologies (Germany), and the organosilane for master mould coating 1H,1H,2H,2H-perfluorodecyltriethoxysilane 97% from abcr (Karlsruhe, Germany). Spincoating was performed with a WS-650MZ-23NPPB spincoater (Laurell Technologies, North Wales, USA), and UV lithography with a mask aligner UV-KUB 3 (Kloé, France).

Table 1. Growth media composition. Composition of the different growth media (GM) used throughout the thesis. All the alternative growth media are variations of the standard MSR-1 growth medium.

COMPONENTS	CONCENTRATION				
	Standard GM	Low iron GM	Motility selection GM	Microwell GM	GUV inner solution GM
HEPES (pH 7)	10 mM	10 mM	10 mM	10 mM	10 mM
Na-pyruvate	27 mM	27 mM	27 mM	27 mM	27 mM
$NaNO_3$	4 mM	4 mM	4 mM	4 mM	4 mM
KH_2PO_4	0.74 mM	0.74 mM	0.74 mM	0.74 mM	0.74 mM
$MgSO_4 \cdot 7H_2O$	0.6 mM	0.6 mM	0.6 mM	0.6 mM	0.6 mM
Fe(III)-citrate	50 µM	—	50 µM	—	—
$FeCl_3$	—	—	—	50 µM	50 µM
Trace elements	See Table 2	—	See Table 2	—	—
Soya peptone	0.3 % (w/v)	—	0.3 % (w/v)	—	—
Yeast extract	0.01 % (w/v)	—	0.01 % (w/v)	—	—
Calcein	—	—	—	25 µM	25 µM
PVA	—	—	—	—	1 % (w/v)
Agarose	—	—	0.1 % (w/v)	—	—
PARAMETERS	Standard GM	Low iron GM	Motility selection GM	Microwell GM	GUV inner solution GM
Temperature	28 °C	28 °C	RT	RT	28 °C
Aeration	Microaerobic	Microaerobic	O_2 gradient	Aerobic	Anaerobic
Magnetic field	Earth	Earth	Vertical	Earth	Earth
Culture volume	10 mL	10 mL	10 mL	pL	pL
Autoclavable	Yes	Yes	Yes	No	No

Table 2. Trace elements. Composition and concentration of the trace elements used in the growth medium [43].

COMPONENT	CONCENTRATION (µM)
Disodium EDTA	15.50
$FeSO_4 \cdot 7H_2O$	7.50
H_3BO_3	0.50
$MnCl_4 \cdot 6H_2O$	0.50
$CoCl_2 \cdot 6H_2O$	0.50
$NiCl_2 \cdot 6H_2O$	0.10
$CuCl_2 \cdot 2H_2O$	0.01
$ZnSO_4 \cdot 7H_2O$	0.50
$Na_2MoO_4 \cdot 2H_2O$	0.15

For the fabrication of microfluidic systems, PDMS Sylgard 184 silicone elastomer kit was purchased from Dow Corning (Wiesbaden, Germany). Spincoating was performed with a WS-650MZ-23NPPB spincoater (Laurell Technologies, North Wales, USA). Surface activation was carried in an oxygen plasma cleaner (Harrick Plasma, Ithaca, USA). To punch the inlets and outlets, 1.0 mm (for the control layer) and 1.5 mm (for the fluidic layer) diameter biopsy punchs were purchased from pfm medical (Köln, Germany). For the operation of the microfluidic systems, liquid flow was supplied to the fluidic layer with PFTE tubing (I.D. = 0.8 mm) purchased from Saint-Gobain Performance Plastics Isofluor GmbH (Germany), whereas the 1 mL plastic syringe to which it was connected was purchased from Braun (Germany). The Tygon tubing (I.D. = 1 mm) to supply with pressure the control layers was purchased from VWR (Germany), whereas the pressure control unit was performed either with an analogical home built one or with an electronic one purchased from Fluigent (Germany). The metal connectors used for the inlet and outlet connections were home built.

3.2.1. General process

PDMS-based microfluidic devices are generally fabricated by means of soft lithography. Lithography refers to the process of printing onto a surface, whereas soft lithography refers to the process as well known as replica moulding, which consists on applying a viscous polymer (such as polydimethylsiloxane (PDMS)) onto a patterned surface and allowing the polymer to cure. The polymer then becomes a solid and is removed from the mould forming a negative of the mould pattern. On the other hand, prior to do the replica moulding process, a mould needs to be created. Such a mould is traditionally a silicon wafer onto which a defined pattern has been creating; in this case, the most common used process is photolithography. Briefly, a photosensitive polymeric layer is applied on top of the silicon wafer and then UV-photolithography is applied to pattern the polymeric layer, also known as a photoresist.

3.2.2. Master mould fabrication

The aforementioned patterned surface necessary to mould the PDMS microchannels is usually referred as *master mould*. Even though master moulds could be virtually made of any material supporting the required features and moulding with PDMS, they are generally produced on silicon wafers coated with a patterned layer of photoresist, legacy of the microelectronics industry. The fabrication process comprises the following steps: pre-baking, photoresist deposition, UV-light exposure, post-exposure bake, development, hard bake and, additionally, silanisation. The steps are explained as follows in Figure 4.

The whole process begins with a bare silicon wafer. First, the wafer has to be cleaned, from any potential organic matter that might be adhered to the surface. This can be achieved by wet methods, such as cleaning with piranha solution (a mixture of H_2SO_4 and H_2O_2), or dry methods, such as baking at 200 °C during at least 30 min. The latter method, known as ***pre-bake***, was the one implemented for the fabrication of wafer throughout the thesis as it was found to be sufficient.

Once the wafer has been cleaned, the following step consists on depositing a thin layer of photoresist on top of the wafer (***photoresist deposition***). The photoresist layer is on the micrometer range, which can go from a few to hundreds of micrometers; in order to achieve a precise thickness throughout the whole wafer, the layer is deposited by spincoating (Table 3). The photoresist height will define the depth of the final microfluidic channels.

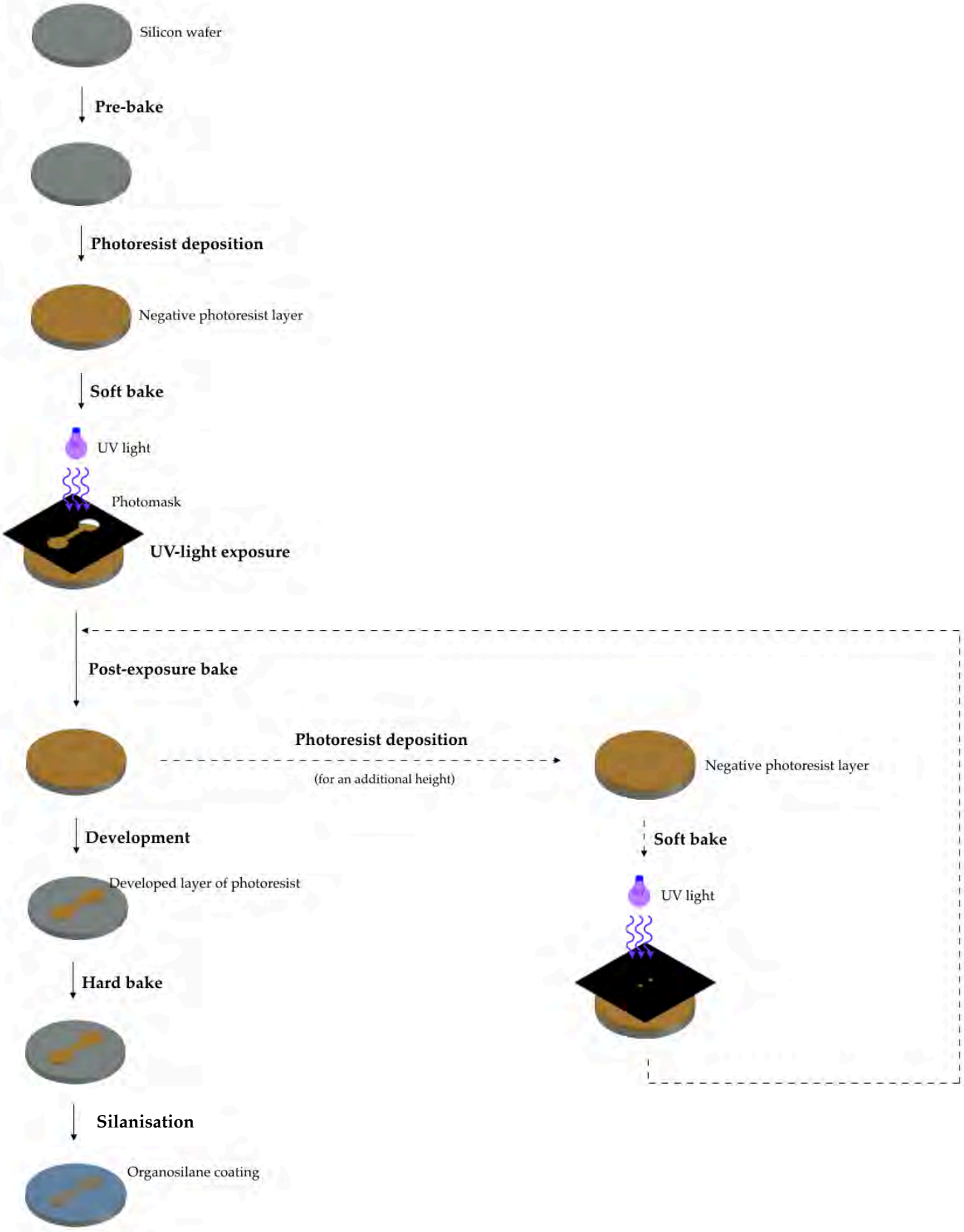

Figure 4. Master mould fabrication. Flow chart depicting the procedure to create a master mould for soft lithography purposes. The column on the left shows the standard steps carried to create a pattern with microchannels having a single height. If the microchannels are to have more than one height, there is an iteration of the photoresist deposition and exposure to be performed for each extra height (indicated by the dashed arrows).

Table 3. SU8 3010 spin parameters. Spin speeds and times used for the fabrication of the master moulds.

SU 3010 SPIN PARAMETERS		
Target height (μm)	First step	Second step
10 (when spincoated on top of the silicon wafer)	500 rpm, 15 s	3,000 rpm, 30 s
10 (when spincoated on top of another layer of SU8)*	500 rpm, 15 s	3,250 rpm, 30 s
20 (when spincoated on top of the silicon wafer)	500 rpm, 15 s	925 rpm, 30 s

*This only used for the fabrication of master mould with two heights.

Once the photoresist has been spincoated, the wafer is baked to allow residual solvent evaporation. The baking times and temperatures depend on each photoresist formulation and layer thickness; the parameters are provided by the manufacturer. This process is known as ***soft bake***.

Once the photoresist has been fixed onto the wafer, the photoresist is exposed to UV light through a photomask (***UV-light exposure***). Here a photolithographic process takes place. The photoresist is a light sensitive resin; these polymers can be divided into two groups depending on the way they are affected by light: negative photoresists (the resin gets cross-linked upon exposition to certain wavelengths) and positive photoresists (the resin gets dissolvable upon exposition to certain wavelengths). In this thesis, a popular series of negative photoresists, SU-8, have been used to create the photoresist layer. The other essential component during the photolithography is the photomask; which is basically an element composed of alternate black and transparent areas forming a pattern which allow to shine the light with a certain pattern (the light passes through the transparent areas, while it will be blocked in the black ones), such as the microchannel pattern. The photomask can be a quartz plate patterned with a layer of chrome, or a polymer film patterned with ink; the chrome masks are usually used when higher resolutions (low micrometer scale, less than about 5 μm) are needed. If a negative photoresist is to be used, the are where the channels are meant will be transparent in the photomask. It should also be noted that the exposure time will depend on the energy of the light source, which is provided by a mask aligner, as well as on the thickness to be achieved. Again, the exposure parameters are provided by the manufacturer.

Following the UV-exposure, the photoresist needs to be hardened by an additional bake, known as the ***post-exposure bake***. The purpose of this additional bake is to finish the photoreaction previously started initiated during the UV-light exposure. Again, the temperatures and times are defined by the photoresist formulation and thickness, and are provided by the manufacturer. At this point, it is possible to see the exposed pattern on the resin by eye.

After the post-exposure bake, the photoresist has to be developed, that is, in the case of a negative photoresist, the photoresist that has not been cross-linked as it has not been exposed to UV-light is removed by submerging the wafer onto a developer solution, and the wafer is rinsed with acetone and dried with N_2. This step is known as ***development***. After the development, the exposed features become visible on the wafer

surface. These features are the ones that will be used to mould the microchannels during the soft lithography process.

After the development, a final baking step at 200 °C during 30 min can be performed to avoid the presence of cracks on the photoresist surface. This final baking is known as ***hard bake***. Following this, the photoresist heights are usually measured; in this thesis the photoresist heights were directly measured with a white-light interferometer, or indirectly by measuring the heights of the resulting PDMS microchannels with a fluorescent solution with a confocal microscope.

A last step is recommended, but not necessary, (***silanisation***) before it is used to mould PDMS. The final step consists on coating the master mould with an organosilane to prevent PDMS sticking to the mould. Eventually, after many uses, PDMS will start sticking onto the mould, but the surface functionalisation greatly slows down this process. The master moulds produced in this thesis were coated by vapour deposition by placing the master moulds along with 50 µL of organosilane into a desiccator, creating vacuum to allow the organosilane to evaporate overnight. Following this, the master moulds are ready to use.

The process described above applies for a master mould where the microchannels have a single height. However, if more complex structures are to be fabricated, it is possible to create microchannels with an additional height by spincoating a new layer of photoresist following the previous post-exposure baking (in this case, the target height to be spincoated is usually set to a 90% of the intended height as the second photoresist layer gets thicker than if it were directly spincoated on the clean wafer) (Table 3). Then, the wafer with the newly spincoated layer is exposed through another photomask, which has a different pattern than the previous one, and is then subjected to a post-exposure bake followed by its subsequent development, hard bake and silanisation. It should be noted that, to ensure the proper UV irradiation through the new photomask onto the already-irradiated wafer, the photomask has to be carefully aligned with the wafer; for this, alignment masks are usually added onto the photomasks.

The aforementioned fabrication process is generally performed in a clean room to avoid dust particles getting deposited onto the wafer surface, as well as certain light conditions. However, if no clean room is at hand, and depending on the accuracy needed, it is as well possible to fabricate the master moulds in a standard wet lab. The elements required for the fabrication are mainly: laminar flow bench, fume hood, oven, hot plates, spincoater and mask aligner.

3.2.3. Photomask design

The photomasks that are used for the UV-light irradiation for the photoresist patterning are generally designed with a computer aided design (CAD) software. In this thesis, all the photomasks were designed with AutoCAD. To fabricate each set of microchannels, as many photomasks as different heights are present in the microchannel are needed; that is, for a single-height microchannel, only one photomask is needed, whereas, for a two-height microchannel, two photomasks are needed, and so on. When a microchannel with different heights is to be fabricated, as explained before, the second photomask has to be aligned (in x-y) with the already-exposed wafer in a very precise way. To achieve this precision, a set of *alignment marks* are included in the photomask

design (Figure 5). These marks allow to properly position the new photomask on top of the wafer by superimposing them (Figure 5C). When designing the photomasks, a number of rules and considerations were followed:

1) The designs were fitted to a 4 inches (10.16 cm) in diameter silicon wafer.

2) The patterns should not be placed directly close to the border of the wafer as this part is more prone to show a higher photoresist height variability than the center.

3) In the case of single-layered microfluidic systems, as many patterns as necessary can be fitted in the mask. This cannot be done for double-layered microfluidic systems due to space restrictions (explained in the soft lithography process section). When designing the photomask for the fluidic layer of a double-layered microfluidic system, a space of at least 0.5 mm between devices should be present to facilitate the control layer alignment and bonding.

4) The perimeter of the microfluidic system area was defined with a rectangle to facilitate dicing apart the microsystems during the soft lithography process. This rectangle will appear in the photomask as transparent line (Figure 6).

5) A thick circumference with the size of the wafer was as well delineated to make the process of photomask alignment easier. This circumference will appear in the photomask as thick transparent line (Figure 6).

6) Moreover, and most importantly, when designing the photomask for the control layer of a double-layered device, the patterns should be scaled up by a factor of 1.016 to compensated for PDMS shrinkage after peeling.

7) Any microchannel and/or feature should have smooth edges rather than sharp ones to avoid PDMS getting stuck in corners when fabricating the microsystems.

8) The inlets and outlets should be located far enough both from the microchannels and the microsystem edge to avoid piercing the microchannels and/or the PDMS edge when punching the inlet and outlet holes. Also, they should be placed with enough space from each other and in an even manner to avoid tubing (for external flow or pressure) crowding.

9) Finally, another consideration has to be taken into account when considering the microchannel height that is intended: the aspect ratio of the microchannels should stay above a low aspect ratio of 1:10 (height:width) and below a high aspect ratio of 4:1 to avoid the microchannels' collapse and PDMS getting stuck in the master mould features.

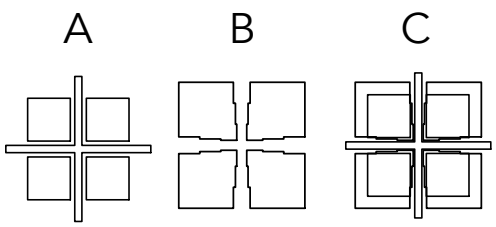

Figure 5. Alignment marks. A shows an alignment mask corresponding to the bottom-most layer, whereas B corresponds to the top-most layer. C shows the resulting superimposition of both patterns. The defined areas appear as transparent regions in the printed mask. It is not needed to implement the alignment marks for silicon wafers that only need to be UV-exposed once, that is, master moulds featuring one single height.

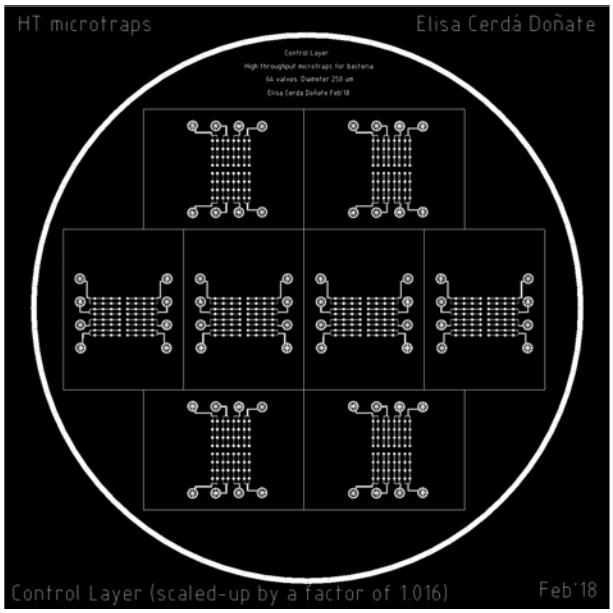

Figure 6. Photomask for a microfluidic control layer. The images shows a photomask with the ink or chrome-covered part in black; the transparent areas are represented in white. The thick transparent circumference is used to delimit the silicon wafer area as well as to assist positioning the wafer during the UV exposure. The thin transparent rectangle perimeters are used to assist dicing the microsystems apart during the soft lithography process.

3.2.4. Soft lithography

The master mould is used to mould the microchannels with PDMS via soft lithography (Figure 7). PDMS is a silicon rubber which is initially provided as two viscous components: a base (the monomer) and a curing agent (the crosslinker) that need to be mixed and cured to give the final polymerised silicon. The components are generally mixed in a ratio 10:1 base:curing agent, which is then degassed to remove air bubbles, and this viscous mixture is poured onto the master mould and is subsequently cured in the oven (the curing parameters are specified at the end of this section). After this, the PDMS is peeled from the master mould yielding the negative of the pattern imprinted on master mould. The inlets and outlets of the microsystem are then punched. Thens, a glass coverslip is cleaned first with ethanol and then with water. Following to this, both the glass coverslip and PDMS slab surfaces are activated in a plasma cleaner (parameters specified at the end of the section) to obtain reactive groups in the surface. They are subsequently brought into contact to create a covalent bond between the glass coverslip and the PDMS, thus sealing the microchannels, whose bottom will be the glass coverslip (it should be noted that materials other than glass can as well be implemented, but that the one whose use is most widespread is glass), and are then placed on a hot plate to improve the bonding. After this, the microchannels are ready to use.

This process applies to the creation of microfluidic systems composed by a single layer of microchannels. However, it is as well possible to create multiple-layered microfluidic devices, which have sets of channels built at different heights. In the present thesis, apart from single-layered microfluidic devices, double-layered devices were fabricated, having two independent sets of microchannels at two different heights separated by a thin PDMS membrane. For the creation of these devices, two different master moulds are used: one for the fluidic

layer (bottom channels) and another for the control layer (top channels). In such case, the the PDMS slab for the control microchannels is produced in the same way described in the previous paragraph, but it is not bonded to a glass slide. In parallel, PDMS is spincoated onto the fluidic master mould up to a height of some tens of micrometers and the thin film is cured in the over. Once the thin film has been cured, it is plasma activated along with the top channel PDMS slabs, and they are then aligned under an optical microscope and brought into contact to create a covalent bond between the two PDMS surfaces. After this, some non-polymerised PDMS mixture is added onto the wafer to fill the spaces between devices and help the peeling process afterwards. The newly poured PDMS is cured in the oven and, once it has been cured, the whole assembly is peeled from the fluidic master mould and the microfluidic devices are diced apart. Then, the inlets and outlets for the fluidic layer are punched in the device and, as for the single-layered devices, the PDMS slab and a clean glass slide are plasma activated and brought into contact to seal the microchannels. After this, the double-layered microfluidic system is ready to use.

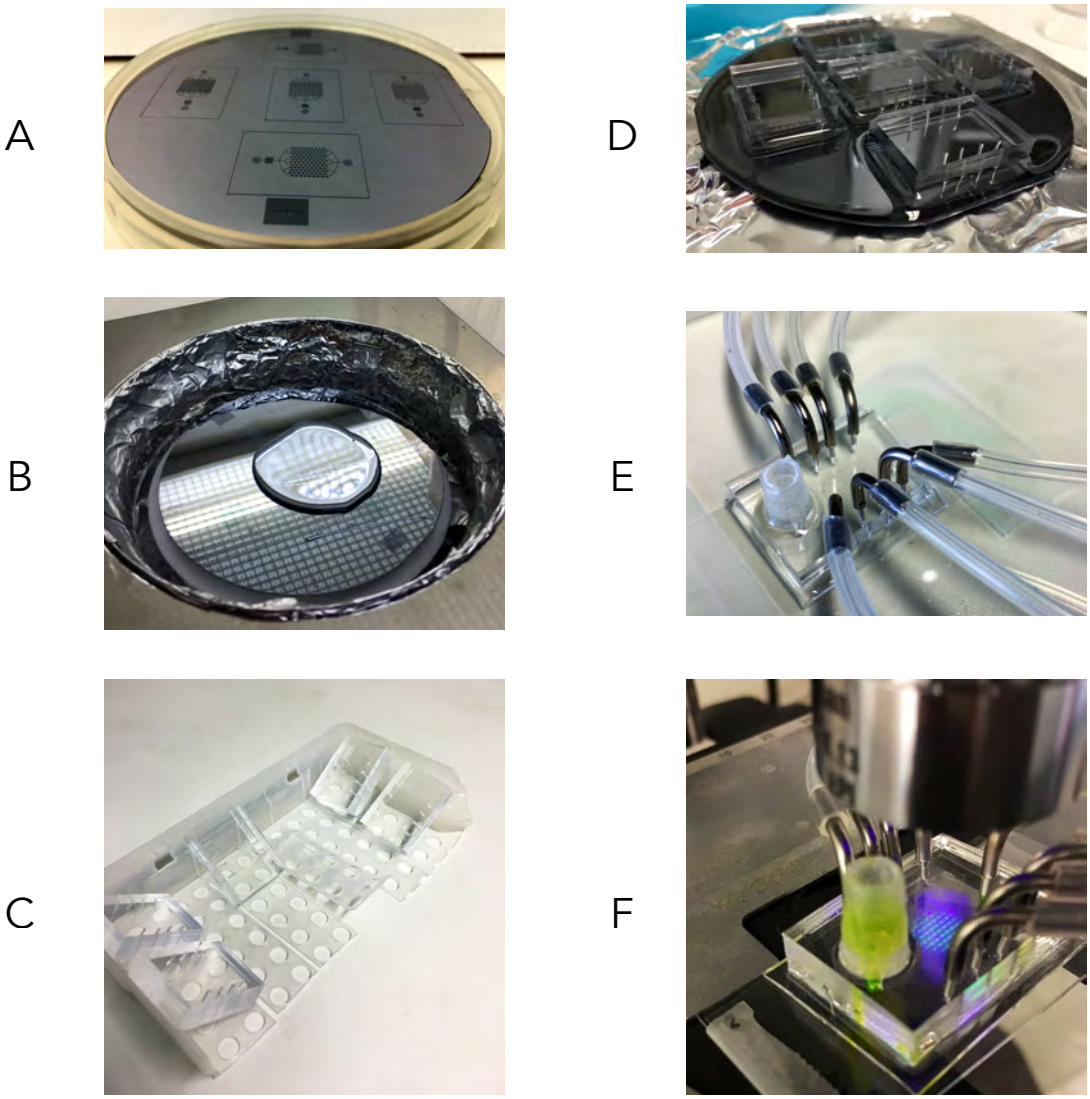

Figure 7. Microsystem fabrication by soft lithography. (A) Master mould for the microchannels. (B) Poured PDMS onto master mould prior to spincoating to create a PDMS thin film. (C) Cured PDMS slabs ready for plasma activation. (D) Cured PDMS slabs bonded to a thin layer of PDMS (this step is only necessary in double-layered microsystems). (E) Tubing connected to microsystem. (F) Microsystem mounted onto the microscope stage.

In the present thesis, non-polymerised PDMS was always cured at 80 °C during 2 h, except when curing a thin layer of PDMS, for which 1 h at 80 °C was used. PDMS 40 µm-thick thin layers were spincoated with a WS-650MZ-23NPPB spincoater (Laurell Technologies, North Wales, USA) using a first step of 30 s at 500 rpm, and a second step of 60 s at 2,000 rpm. PDMS and glass coverlips were activated with a plasma cleaner (Harrick Plasma, Ithaca, USA) during 1 min at 0.8 mbar at full power. After bonding, the microsystems were placed on a hot plate at 60 °C for 5 min.

3.3. Microscopy

3.3.1. Transmitted light microscopy imaging

Transmitted light imaging was performed via phase contrast in a custom-built microscope bearing three sets of Helmholtz coils (Figure 8) allowing to cancel out the Earth magnetic field as well as to apply magnetic fields in different directions and intensities to the sample [15].

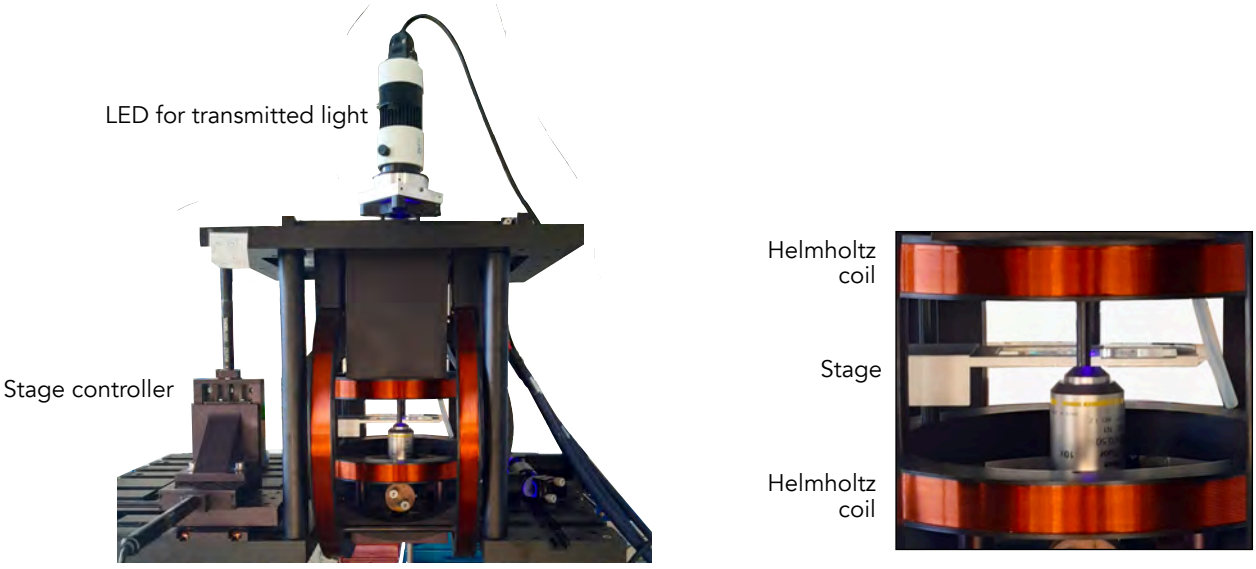

Figure 8. Home-built inverted light microscope with 3D Helmholtz coils set-up. The microscope stage and the objective are located among three pairs of Helmholtz coils (in orange); each pair being placed in one direction. The Earth's magnetic field is cancelled in the central space among the coils. The non-magnetic stage is made of aluminium and is motorized in x-y-z by a stage controller. For transmitted light images, light is shone from an LED source, and light is collected through the inverted objective. The image is then captured by a camera placed behind the set-up (not shown in the image).

3.3.2. Fluorescence confocal imaging

Calcein fluorescence was observed by confocal microscopy (SP8 DMi8, Leica) (Figure 9). For quantitation and imaging purposes, a 63x objective (water immersion, N.A.=1.2, Leica) and a 488 nm excitation laser were used. The fluorescence signal was acquired between 498-580 nm. The scanning speed was set to 600 Hz, and the line averaging was set to 4. Time lapse images were recorded with a frequency of 10-30 min. Calcein fluorescence was quantified with the LasX Leica software.

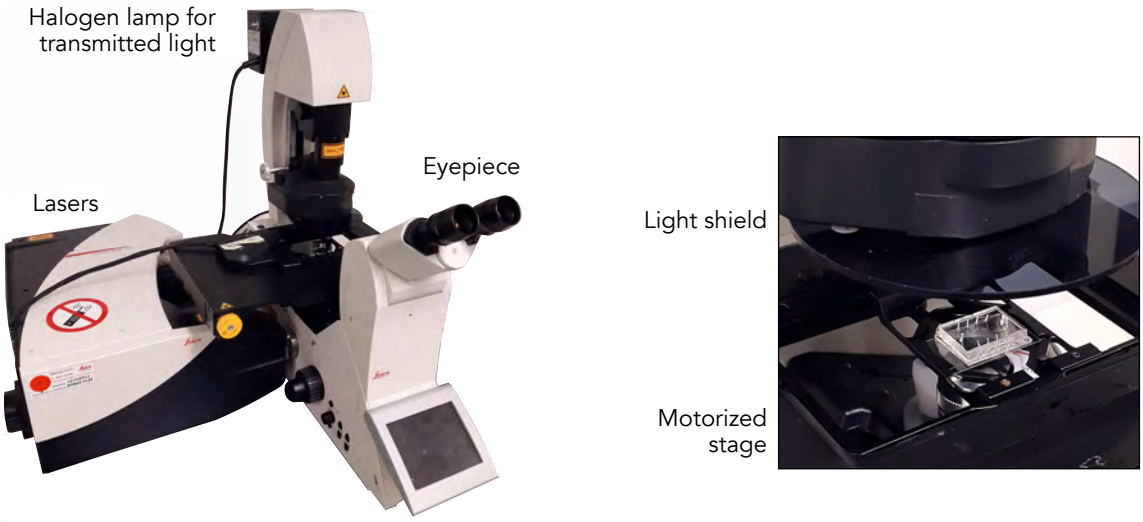

Figure 9. Confocal microscope set-up. Transmitted light images can be obtained with a halogen lamp as well as with lasers. Fluorescence (reflected light) images can be obtained via a mercury lamp (not shown in the image) or with lasers. For confocal imaging, lasers' reflected light is detected either by photomultipliers or by a hybrid detector, whereas lasers' transmitted light is detected by another photomultiplier exclusive for transmitted light. For non-confocal imaging, the transmitted light from the halogen lamp, or the reflected light from the mercury lamp is detected by a camera. The microscope stage is motorised in x-y-z. On the right image, a mounted simple microfluidic system is shown.

3.3.3. Transmission electron microscope imaging

Transmission electron microscope (TEM) imaging was performed to complement the observation of the cells and image the magnetosomes. To prepare the samples, 20 µL of growth medium with bacteria were deposited on a TEM grid and allowed to settle down for 30 min before washing them twice with milliQ water and drying them with paper wipe. TEM images were taken with a transmission electron microscope (EM912, Zeiss) at an accelerating voltage of 120 kV with a magnification of 4,000-10,000x.

3.4. Bulk fluorescence measurements

Bulk fluorescence measurements were recorded with a Fluoromax-4 spectrofluorometer (Horiba Jobin Yvon Inc.) with a 10 mm path length quartz cuvette (Hellma, Sigma-Aldrich) at an excitation wavelength of 488 nm, excitation slit width of 1 nm, emission wavelength between 495-600 nm, emission slit of 3 nm, and an integration time of 0.01 s.

4. Mimicking the physical microenvironment: a sediment-like microfluidic system

This microfluidic platform arises from a collaboration with Paul Zaslansky, Mohammad Charsooghi and Agnese Codutti. The aim of the collaboration project was to establish a platform that mimics the physical boundaries from the sediment that MTB encounter in their natural environment to understand how magnetotaxis influences the navigation in a complex porous environment as well as to understand the interaction of the bacteria with the sand grains. The natural sediment X-ray microtomography (microCT) images were taken by Paul Zaslansky, microfluidic systems were designed and fabricated by myself, measurements with bacteria and data analysis was performed by Mohammad Charsooghi, whereas the simulations were performed by Agnese Codutti.

4.1. Introduction

The first observation of magnetotactic bacteria was reported by Bellini [4], who found this new type of bacteria when examining a drop of wastewater from a hole excavated in the ground. Bellini withdrew samples from various sites: the already mentioned ground wastewater, as well from sediment from drainage tanks, permanent puddles, swamps, marshes and shallow lakes. Yet, in all of them, he observed the ubiquitous and notorious presence of these bacteria, mainly anaerobic, that naturally swam always in the same direction: towards the geomagnetic North pole. However, his observation did not reach the international scientific community. A decade later, though, MTB came to international knowledge when Blakemore reported as well the presence of such microaerobic [44] or strictly anaerobic bacteria in marine sediments at concentrations of 200 to 1,000 cells per milliliter [5]. He noted the presence of flagella in the bacteria, which allowed them to swim, as well as the presence of intracytoplasmatic membrane vesicles. The latter were of particular interest as they contained iron-rich nanoparticles, and showed a unique arrangement into linear chains inside the bacterium, which imparted a net magnetic moment to the cell, allowing it to orient with magnetic fields. This confirmed the theory that Bellini had developed upon observation of the bacteria: the bacteria were acting as tiny magnetic compasses. Upon this re-discovery, Blakemore gave them the name of magnetotactic bacteria (MTB), from which he reported at least five distinct species [5].

Both Bellini as well as Blakemore found the bacteria in samples retrieved from sediment. It is noteworthy to mention that the appearance, discovery and isolation of novel MTB has been repeatedly linked to the sampling of sediments belonging to the beds of different water bodies [45-49]. This reads true even for MTB found in extreme environments, such as moderately thermophilic MTB, alkaliphilic MTB [50], halophylic MTB [51] or piezophylic MTB [52].

From the current knowledge, it appears that MTB take sediments as their natural habitat. It is in the sediment, where the bacteria use their magnetic field sensing to align themselves with the geomagnetic field lines and find their optimal chemical conditions in the oxic-anoxic transition zone (OATZ). During the past years, attention has been drawn to the fact that environmentally collected MTB from the Northern hemisphere usually swim persistently towards the North geomagnetic pole (North seekers), whereas those collected in the Southern hemisphere swim towards the South geomagnetic pole (South seekers), both of them designated as polar MTB. It is important to note that upon sustained cell culture in lab conditions (generally based on pure liquid medium with no sediment grains), this behaviour can get lost in favour of axial cultures, which differ from polar bacteria in the sense that axial bacteria do not have a preferred swimming direction [53]: while they still swim parallel to the magnetic field lines, they do not show any preference towards any pole, hinting that environmental pressure is probably present to keep magnetotaxis.

That said, these features point to the fact that MTB's very own nature and organisation is tightly bound and adapted to the environment they inhabit. However, most research that has been performed on MTB has taken place in conditions that despite being favourable for their optimal growth, are certainly not the conditions they encounter in nature. Until the moment, only one study has addressed MTB in sediment in lab conditions in 1L sediment-filled jars [54]. For this reason, if a deeper understanding of the motion and ecological meaning of these bacteria is to be gained, more studies need to be performed in their natural habitat, sediment, rather than in systems such as aerotactic bands in capillaries [15], drops [55], tubes [55], or in bulk, as they certainly do not resemble the milieu MTB face in nature. This means that removing the natural microenvironment might, on the long term, be detrimental for the study of the MTB and their data collection and interpretation, as an extrapolation of such lab-derived data might not quite fit the actual MTB behaviour in their natural environment, and might incur in misleading conclusions.

However, studying the bacteria in the sediment is not simple at all as sediment is a heterogeneous system defined by complexity at the physical, chemical and biological level. Sediment is conformed by grains of any nature embedded in a water matrix that create an intricate 3D maze of pores and channels where cues such as temperature or chemical gradients overlap and get intertwined yielding a highly complex system where there are far too many different parameters to be precisely controlled. Moreover, as sediment is not transparent to light, observations of swimming bacteria in it are generally precluded.

This scenario calls for a system where complexity can be implemented, controlled, reproduced and understood, as well as where standard optical microscopy techniques can be applied. In this context, and with the motivation of understanding the bacterial interaction with the sediment, a microfluidic platform mimicking the sediment is presented in this chapter to understand the impact of the physical microenvironment on bacterial motion.

4.2. Objectives

The objective of this project is to design a microfluidic platform that mimics the MTB natural environment, the sediment, which is characterised by a crowded boundary-rich environment, so that it becomes possible to study the motion and interaction of the bacteria with it, and how it is affected by the presence of magnetic fields.

4.3. Materials and methods

4.3.1. Materials

M. gryphiswaldense bacteria, growth medium, master mould and microfluidic system components are specified in the *General materials and methods* section. Besides this, a sediment sample from Wublitz lake (Potsdam, Germany) provided by Damien Faivre was used to model the microchannels.

4.3.2. microCT scan of the sediment

A sediment sample was placed in a plastic cuvette of 4 mm in diameter, with a layer of water covering the top of it. The scan was performed by SkyScan 1172 scanner with the following settings (X-ray voltage = 89 kV, 112 µA, image pixel size =1.56 µm, exposure = 1400 ms, rotation step =0.150 °, frame averaging). Raw data were reconstructed using NRcon software (Version 1.6.10.4) with the following parameters: pixel size = 1.56202 µm, reconstruction angular range = 360.00 °, angular step = 0.1500 °, ring artefact correction = 10, smoothing = 0, filter cutoff relative to Nyquist frequency = 100, filter type description = Hamming (α=0.54), beam hardening correction = 70%.

4.3.3. Silicon wafer production, microsystem fabrication and experimental set-up

A master mould with 10 µm deep features was produced with a chrome mask to obtain high resolution features down to 1-2 µm. The microchannels were moulded with PDMS and were then bonded to a glass coverslip. Previous to its use, the microsystem's central channel was filled with MSR-1 standard growth medium and was incubated at room temperature for at least 30 min to minimise any concentration change in the growth medium during the measurements. Subsequently, a drop of MSR-1 standard growth medium containing bacteria was placed in the inlet and the bacteria were allowed to swim without flow into the microchannel to avoid bacterial translation due to convection. Different magnetic fields (B = 0, 50, 500 µT) intensities were applied parallel to the microchannel length. Bacteria were imaged with a 10x objective using phase contrast microscopy (Figure 10).

4.3.4. Simulations

In the simulation, the bacteria are described as active brownian particles with different states of motion (runs and changes of direction) [56]. For axial bacteria, the length of the runs can be modulated by the oxygen gradient to perform chemotaxis. Moreover, the bacteria posses a magnetic moment and thus feel the passive alignment from the external magnetic fields. The sand environment is described as a set of cylinders on which the bacteria feel steric repulsion and an effective torque simulating hydrodynamic reorientation. The set of cylinders is obtained fitting with circles the real-sand microCT-scan slices. The output of the simulation are the 3D trajectories of the single bacteria, which can be compared directly to the experimental output.

4.4. Results

4.4.1. Microfluidic system design

The microfluidic systems were designed from slices obtained from a microCT scan of a sediment sample coming from Wublitz lake (Potsdam, Germany). The microfluidic systems were made out of PDMS, except for the bottom, which was a glass coverslip, and were based on a generic structure composed of three parallel microchannels where the content of the central microchannel varied among different designs, whereas the lateral microchannels remained constant (Figure 10). The width of the microchannels was 1,330 µm for the central microchannel and 100 µm for each of the lateral ones. The PDMS boundary wall among them was set to 25 µm. The length for the patterned part was roughly 3.5 mm. The height of the microchannels was set to 10 µm, as larger dimensions would not allow to restrict the bacteria as much as possible to two dimensions, which is detrimental for tracking purposes as for deeper microchannels the bacteria will get out of focus and their trajectories will be lost during imaging. By restricting the z-direction, the bacteria get more confined, but focusing with the microscope objective can still be performed. Moreover, the rationale behind setting the height to 10 µm originates from the need of comparison with the microfluidic system described in the following chapter, which, despite complementing this platform, was designed previously and featured a height of 10 µm.

In terms of length and width, the width of the PDMS walls separating the lateral channels to the central one tried to be kept as thin as possible whereas ensuring its proper fabrication. For this purpose, 25 µm was taken as a safe thickness. Also, it should be noted that the inlets were placed close enough to the start of the patterned channel (1.5 mm) to allow bacteria to rapidly reach the patterned area exclusively by their own propulsion, as the experiments were designed to be initially performed with no liquid flow. For this, it was taken into account the swimming speed of *M. gryphiswaldense* MSR-1, which has been reported to be in the range of 15-20 $\mu m \cdot s^{-1}$ [15]. To avoid liquid flow, prior to the measurements, the microchannel was first filled with growth medium and, only afterwards, a drop containing bacteria was added to the inlet so that bacteria are allowed to swim until the sediment network, and a drop containing only growth medium was added to the outlet.

The central microchannel can be used with or independently from the lateral microchannels, which are meant to provide the microsystem with a stream of air and a stream of nitrogen. By flowing a stream of each gas in the lateral microchannels, an oxygen gradient can be created as one gas will be providing 21% oxygen, whereas the other will provide 0% oxygen, as PDMS is permeable to both gases [57]. In this way, an oxygen gradient comparable to the one encountered in the sediment in the OATZ can be implemented in the microchannel. The laterals channels are therefore designed to have a microsystem where it is possible to implement redox gradients, that is, the lateral channels are meant to provide an added layer of complexity by modifying the chemical microenvironment. However, this option has not been explored yet with this specific platform.

The central microchannel is actually the main one constituting the microsystem and the one giving the opportunity to study the physical microenvironment, it constitutes the flow microchannel whose purpose is to host a bacterial suspension to study the motion of the bacteria. The particularity of the central is the pervasive presence of PDMS pillars of different architectures. These pillars were moulded from the sediment grains coming from the lake sediment microCT scan stacks. Therefore, the central channel mimics the physical microenvironment

the bacteria are subjected to in their native habitat. Apart from this, an analogous microsystem with an empty channel was as well designed as negative control to compare for the differences arising between a packed crowded boundary-filled environment and a bulk-like one.

Moreover, another set of microfluidic systems was as well fabricated which had analogous central channels to the ones described above. However, these alternative microchannels did not host the sediment particles, but an approximation to them created by converting the sediment particles into circles of the same

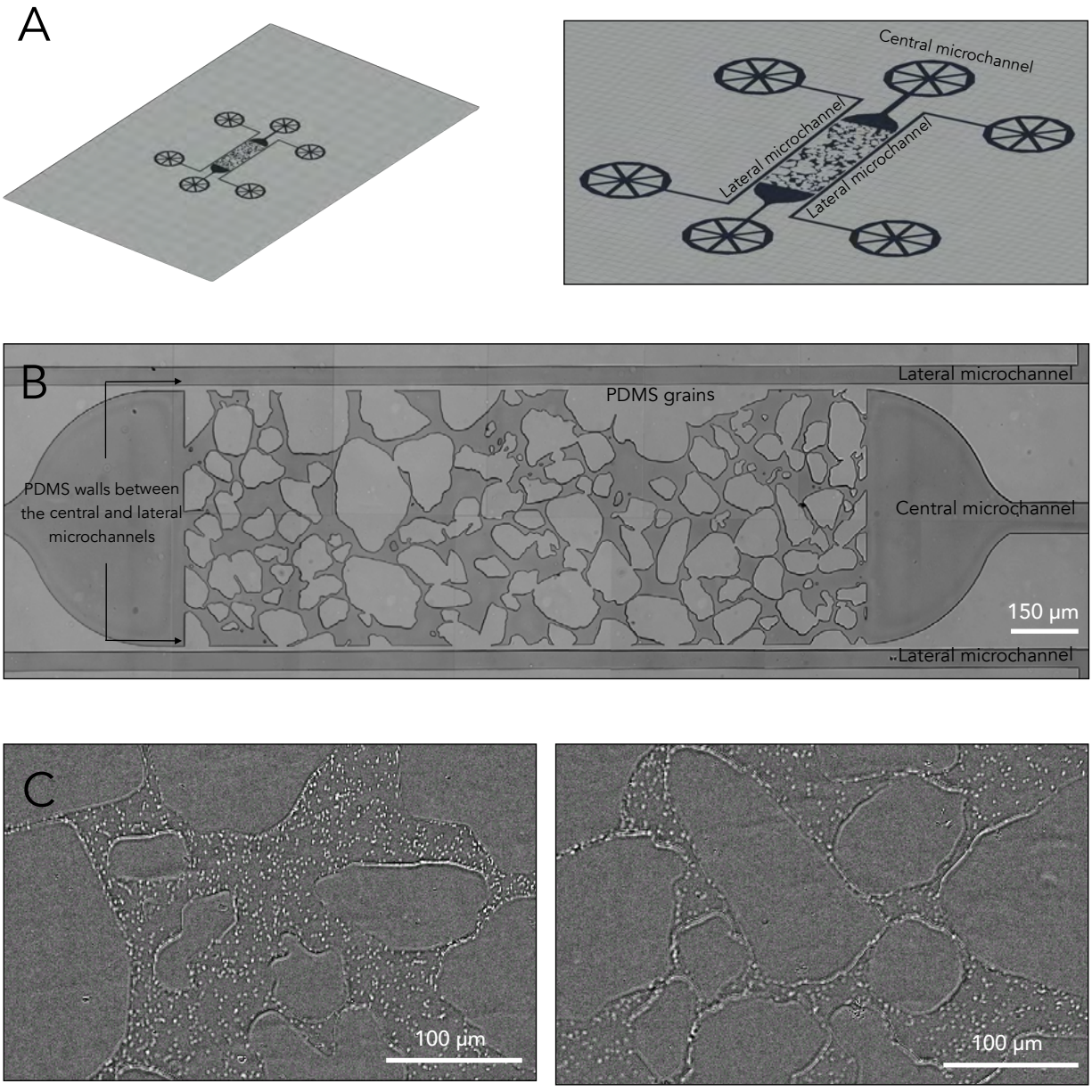

Figure 10. Microfluidic system structure. (A) Different close-ups showing the microfluidic system structure. The first one shows the PDMS area around the microchannels. For visualisation purposes, only the 10 µm heigh slice where the microchannels are located is shown, whereas both the bulk PDMS slab that would go on top of the depicted area as well as the glass slide that would go beneath have been omitted from the sketch. In the sketches, both the central channel filled with sediment as well as the mirrored lateral channels can be seen. (B) Transmitted light image of one sediment-filled microchannel. (C) Transmitted light images showing bacteria (white dots) inside the sediment microchannel.

area. The purpose of these alternative microchannels was creating an alternative microsystem where both the particle packaging as well as the particle area were comparable to the genuine sediment-like microchannels, but which could be simulated by numerical methods, as the rough shapes of the actual sediment granules would have added too much complexity to the simulations. Therefore, these microchannels were designed as a means to bridge the actual measurements in a sediment-like environment with the numerical simulations, so that an easier comparison is achieved.

Finally, it should be noted as well that the sediment grain network as well as its circle approximation in the microchannels were manually curated: 1) any structure that would potentially derive into an air pocket after microchannel bonding was erased from the design, 2) any duct with a narrower opening than 2 μm was trimmed up to a predetermined size of 5 μm to ensure proper fabrication and water flow, and 3) any dead-end path was as well opened to enable liquid flow as well as bacterial navigation.

4.4.2. Experimental results and numerical simulations

As an example of the results this microfluidic platform yields, some experiments and experimental simulations carried by Mohammad Charsooghi and Agnese Codutti, respectively, are presented now.

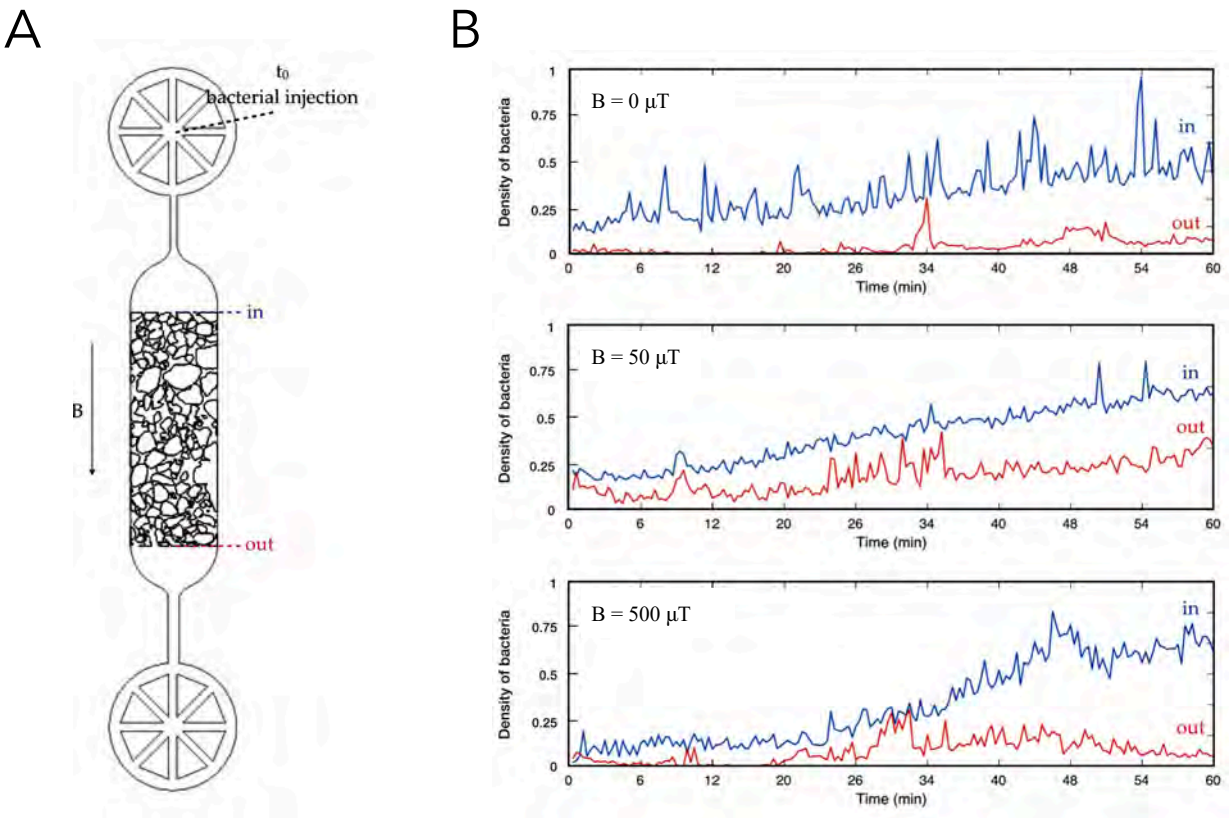

Figure 11. Experimental bacterial positioning under different magnetic fields strengths. (A) Experimental description showing the the points where the bacteria where injected (t_0), and the locations in which the number of bacteria was monitored over time at the beginning (in) and exit (out) of the microchannel. The magnetic field was applied parallel to the microchannel. (B) Amount of bacteria over time at the entrance and exit of the sediment network for three different magnetic field intensities (B = 0, 50 and 500 μT).

The experiments consisted on adding a drop of bacteria at the microfluidic channel inlet and record the number of bacteria present at the beginning and at the exit of the sediment network over time under different magnetic fields (Figure 8). The experiments show that the number of bacteria at the beginning and at the end of the network increase over time. However, after 1 h there is a substantial increase in the amount of bacteria that reach the end of the microchannel only for a magnetic field strength of 50 μT (that is, the Earth magnetic field strength), compared to a 10-times stronger field and no field at all, where in both cases less bacteria navigate until the end of the microchannel.

The numerical simulations reproducing the trajectories of bacteria in the sediment microchannel with and without sediment at the previously mentioned magnetic field intensities and with and without field, are shown in Figure 12. It can be observed that the sediment-like simulations are performed in the channels with the circular approximations. The simulations show that applying a magnetic field restricts the bacterial navigation in the y direction as the field strength increases. Moreover, it is observed that for any magnetic field strength, the overall bacterial net displacement is more pronounced when no sediment is present, even though this difference is not as pronounced when no magnetic field is present as when there is a magnetic field. Also, it is observed that the highest net displacement takes place for 50 μT in both cases.

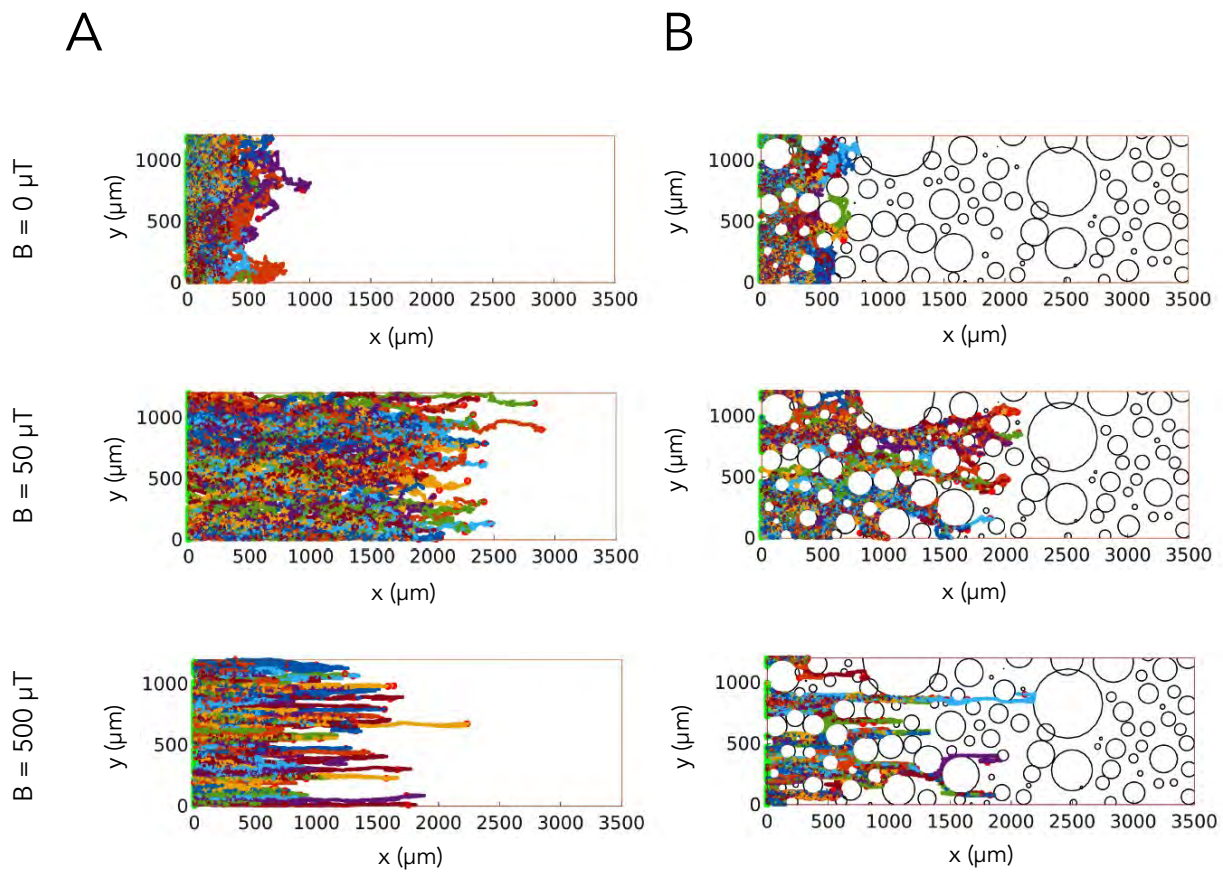

Figure 12. Simulation of bacterial trajectories under different fields. Simulated bacterial trajectories in an empty (A) and sediment-like (B) microchannel for three different magnetic field intensities (B = 0, 50 and 500 μT). Position 0 in the x axis indicates the entrance of the microchannels. The simulated microchannels had the same dimensions as the fabricated microchannels. Each coloured line represents the trajectory of a single bacterium.

4.5. Discussion

4.5.1. Mimicking the sediment: resemblance and divergence to the natural sediment

The hereby presented microfluidic system attempts to simulate the physical microenvironment *M. gryphiswaldense* encounters on its natural habitat. However, how does it differ from the natural one? It needs to be acknowledged that sediment is a highly complex environment where physicochemical parameters get intertwined in various ways, making it difficult to study as it is not a homogeneous medium. For that reason, simpler approximations have to be put into play where analysis becomes more manageable. The first characteristic that makes the study of the bacteria swimming in the sediment complicated is probably the opaque nature of many sediment particles to visible light, which complicates the visualisation of the bacteria. Consequently, if operating with optical microscopes, alternative materials transparent to visible light, such as glass, PDMS, PMMA or SU-8, have to implemented; but their physicochemical characteristics will be different compared to the actual sediment, which is moreover not composed of a single and homogeneous material.

Sediment is generally classified as a function of two parameters, one based on a physical perspective whereas the other based on a chemical one: grain size and composition. According to the Udden-Wentworth grain size scale, sediment can be classified as clay (<3.9 μm), silt (3.9-63 μm), sand (63 μm - 2 mm) or conglomerate (>2 mm) [58]. This indicates that the lake-bed sediment analysed by microCT is composed by silt and clay. However, there might be a slight overestimation of the analysed particle size given the impossibility to resolve overlapping grains as individual structures.

As it can be observed in Figures 10-12, there is a size and shape distribution of the sediment grains. On this ground, the set of techniques and materials that have been used for the fabrication of the microsystems (photolithography on SU-8 through a chrome mask, and PDMS-based soft lithography) are advantageous to create a set of different sizes and shapes, where roughness can be represented in the low micrometer range. Given the resolution of soft lithography, this technique can be used for the creation of sediment-like structures down to coarse clay grains, that is, coarse mud. If the fabrication of finer grains of mud is needed, other techniques with higher resolution would then be needed.

It should be as well noted that the use of soft lithography limits the structural complexity of the z-axis provided by a 3D porous structure as the sediment (known as connectivity), as it is only possible to introduce pillars or holes per PDMS layer. The sediment, though, is composed by grains, which have complex 3D structure. Therefore, the technique used here limits the resolution that can be achieved in the third axis. More complex 3D structures could be achieved by fabricating multilayered devices where layers of different configurations would be stacked on top of each other to provide a complex 3D structure. Nevertheless, this strategy is not recommended as the layer alignment is generally performed manually under a microscope, meaning that a perfect alignment of the layers is complicated to achieve, especially for small features. This would end up on a higher structural variation within *identical* microsystems as there would always be small stacking mismatches. Despite the fact that one single-height PDMS-based microsystems present a strong limitation in terms of implementing a third direction, it should be as well acknowledged that this is, from another perspective, an advantage in the sense that it reduces the possibility of getting bacteria out of focus which would then be lost while tracking. Therefore, for tracking purposes, this reduced complexity in the z-direction is actually beneficial for the sake of data analysis and

control over the system. Nevertheless, if more complex 3D structures with variations in the z-axis are aimed, alternative fabrication techniques such as stereolithography can be implemented. Alternatively, another strategy that has been used to provide a third dimension is the sintering of packed glass beads [59].

Another major parameter which has been usually disregarded is the stiffness of the material. It is now acknowledged that the material stiffness can trigger different bacterial behaviours which can decide the fate of adhering to a surface or not [60]. PDMS has a Young's modulus of 0.0013-0.003 GPa [61], compared to that one of glass 50-90 GPa [62]. The sediment particles' Young's modulus will have very varied stiffness depending on their inorganic or organic nature. Consequently, the stiffness of the material should as well be considered for fabrication purposes as it can alter the bacterial interaction with it and, consequently, its swimming behaviour.

The sediment is as well usually defined by its chemical composition. The material will have not only a direct impact on the material stiffness, but also on the chemical surface it will display, and this is another parameter that needs to be contemplated, as it will have a direct impact on the way the bacterium interacts with the surface via electrostatic attractions. As a result, the surfaces of the materials employed for the fabrication of the microsystems should as well considered. However, if the surface of the material does not display the desired properties, it can be contemplated to passivate the surface to achieve the required chemical characteristics, as various moieties can differently affect the bacterial interaction with the surface [63]. In the case of PDMS, we face a material of hydrophobic nature whose surface group can be turned into hydroxyl groups by different treatments, such as plasma activation, making it possible to obtain a more hydrophilic surface that can be functionalized. It should be borne in mind that this hydrophilicity is transient and that decreases over time [64, 65]. Glass, on the other hand, has a net negative charge, which can repel the bacterium, as this one has as well a net surface negative charge due to the polysaccharides present on the outer membrane [66].

Another point to consider is the presence of chemical gradients in the sediment, namely the redox potential gradient, mainly caused by the oxygen gradient, even though others such as sulphur one will be as well present. Both the sulphur and oxygen gradients can be considered steady gradients over time, as they will be always present. However, decomposing matter will provide transient gradients of different nutrients which will generate as well an impact on the bacterial navigation due to the diverse chemotactic behaviour in *Magnetospirillum* species, which bear one of the widest sets of chemoreceptors known to date with 44 different chemoreceptor coding sequences in *M. magneticum* AMB-1 [67]. The steady gradients can be implemented within the microchannels with a gradient generator, as it is envisaged for the presented microsystem through, for example, the positioning of an aerobic microchannel and an anaerobic microchannel flanking the microchannel where the gradient is to be generated. For the implementation of such gradients, PDMS is specially attractive as it is highly permeable to gases such as O_2 and N_2 [57], thus making it a good candidate if this sort of gradients are required [68], given the fact that MTB swimming direction is governed as well by the oxygen gradient, behaviour known as magnetoaerotaxis [16, 55]. Other gradients and variations are present in sediment, such day/night oscillations, which can trigger a different set of chemical reactions as well as phototactic behaviours, and presumably could be implemented as well in the microsystems.

From a biological perspective, bacteria do not tend to naturally live in axenic cultures, but complex communities where they cohabit with other species. A faithful reproduction of such ecological niches could only be achieved by withdrawing a sample from nature and directly transferring the species into the microsystem. The

network structure that interconnects these species will of course be lost when working in axenic cultures. Moreover, the bacterial densities at which the bacterial are inserted in the microsystem are not necessarily the same density at which organisms are encountered in fresh water bodies, where their density might be 10 times lower than the one used to add bacteria in the medium [69].

4.5.2. Experimental results and numerical simulations

The presented experimental and simulated results have been shown as a means to understand which sort of measurement can be performed with this platform and the information that can be extracted from them. As seen in the experiments and in the simulations, the used platform was different: one with sediment grains whereas the other with circular approximations, as explained previously. However, in the future, additional measurements will be performed as well in the simulated designs to analyse how it compares to the simulations and to the matching real sediment experiments. Despite of this, from both results it can be seen that 50 μT represents an optimum for the bacterial navigation in comparison with no field and a field ten times stronger. It should be noted that *M. gryphiswaldense* was first isolated from a river sediment in Greifswald (Germany), where the Earth's magnetic field is close to 50 μT [70], reason for which such magnitude was chosen. Therefore, the measurements would be in line with the current theory that MTB have their magnetic moments optimised to have advantages for the magnetic field strength of the place where they dwell [71]. It should be taken into account that MTB can be found in a myriad of locations on the globe, each of these locations bearing different magnetic field strengths and pointing directions [50, 52]. The present platform could be therefore easily implemented to study different MTB species under different magnetic field strengths and directions to check whether there are optimal field strengths for each species in a sediment-like environment, and whether they correlate to their natural habitat, thus reinforcing the idea that all MTB have their dipoles optimised for their ecological niches. From the present results, it is seen that indeed the lack of magnetic field does not help navigation, and that a too strong magnetic confines too much the trajectories in 1D, therefore restricting the avoidance of obstacles and impeding a net advance.

This system could also be used to investigate how non-magnetic MTB interact with the sediment with or without oxic gradients and to determine their orientation capacity. It should be noted that the isolation of MTB from the environment relies on magnetic separation methods, but it is known that several MTB, such as *M. gryphiswaldense*, can remain non-magnetic and viable over several generations without losing their ability to produce magnetosomes if no available iron is present in the environment (such iron-starvation method has been used in later chapters of this thesis). Despite this, it appears to be an evolutionary pressure on keeping the magnetosome chain, thought to be due to this advantage to orientate in the sediment and find the preferred redox conditions, so such advantage could as well be tested with this platform.

On top of this, once the oxic gradient is implemented, the platform could be of use to study how displacements of the Earth's magnetic field could affect the positioning of the bacteria in the water column, as well as whether power generators in rivers and seas could alter bacterial navigation in their ecological niches [72]. In the same fashion, it could be used to explore whether there are given sediment sizes and packings that affect the bacterial navigation and whether this has any impact on the advantage provided by magnetotaxis. Overall, it could be used to extract different parameters to predict the environments MTB can inhabit.

To date, as it was mentioned at the beginning, despite the fact that the MTB swimming has been extensively studied in different platforms, most of them address bulk situations even though they rely on glass slides, microcapillaries or droplets, which do not represent the bacterial natural environment [15, 16, 73]. Some of the platforms that have been studied are microfluidic, but again, failed in the same sense [74]. To date, only one study has directly addressed the question on how a coarse environment affects the motion of MTB [75]. In such study, they report a microsystem with hexagonal pillars with homogenous or heterogeneous sizes as well as varying packings to study another *Magnetospirillum* species. The system, though, has 10 μm or wider gaps between the hexagonal pillars, and only the flat surfaces of the hexagons are encountered by bacteria. The system here presented, however, offers a more varied microenvironment with concave and convex surfaces that adjusts more to the actual environment encountered by the bacteria. Yet, both systems are still purely based on the physical microenvironment of the bacteria. We expect, though, to implement in the future an oxic gradient that can be superimposed in the microsystem so that it becomes possible to study the interaction between a magnetic field, a crowded environment and a chemical gradient, to understand how the interplay of these factors affect bacterial motion, which is of major interest to fully understand their ecology, as well as they swimming behaviour if they are to be used as targeted microswimmers in crowded environments.

It also has to be pointed out that when experiments become more complicated by adding new parameters (such as chemical gradients), there is a chance that the experiments and simulations will have divergent results or lower matches, as not all the parameters in the simulation might be totally tuned. Specially, when moving towards a scenario where bacteria not only interact with the physical microenvironment, but also with the chemical one (with aerobic gradients and aerotactic behaviours), both interactions will need to be very well defined to properly assess the process that is taking place. To properly define and understand such interactions, a deeper level of sediment-bacterium interaction has to be addressed, that is, the interaction between a single bacterium and the sediment needs to be understood. For that reason, the following chapter addresses a complementary microfluidic platform that seeks to simplify the study of such interactions.

4.6. Conclusion and outlook

In the present chapter a PDMS-glass microfluidic platform to mimic the physical microenvironment of *M. gryphiswaldense* in its natural environment, the sediment of fresh water bodies, has been presented. The central points to the presented platform are that 1) it allows for the 2D reproduction of the sediment topology with a resolution in the lower micrometer range and for performing tracking experiments with the optical microscope, and 2) it mimics the physical boundaries that bacteria encounter in the natural microenvironment in sediment.

In the future, it is expected to implement an oxygen gradient to study the interplay of magnetotaxis, aerotaxis and a crowded environment at different angles. However, to gain a deeper understanding of the bacterial interaction with the sediment, the present system might still be too complicated as there is still a wide area where the bacteria can swim to, thus going away from the field of view or passing nearby other bacteria. Consequently, in the following chapter a complementary microfluidic system which drastically reduces the level of complexity of the physical microenvironment is presented.

5. Reducing the microenvironment complexity: confinement of single-cells in microwells

This microfluidic platform arises from a collaboration with Mohammad Charsooghi and Agnese Codutti. The aim of the collaborative project was to establish a platform that allows the study of isolated MTB single cells in confinement to understand how the bacterial swimming speed, the wall curvature, and magnetic fields affect the bacterial swimming trajectories. The microfluidic system design, fabrication and analysis were performed by myself; bacterial swimming measurements by M.C. and myself; image processing by M.C., data analysis by M.C. and A.C., and simulations by A.C.. This chapter complements the previous one by dealing with bacterial swimming, magnetotaxis and bacterium-wall interactions at the single-cell scale.

5.1. Introduction

In the previous chapter, a sediment-mimicking platform to study the physical (and potentially the chemical) microenvironment impact on bacterial motion was described. However, as it was already hinted, to exactly study the interaction with the sediment, that is, with solid boundaries, both at a physical and at a chemical level, and to acquire the ability to make predictions in such systems, it becomes necessary to further simplify the system.

The sediment-like system allows the study of how bacteria interact with the different particle surfaces. Yet, from particle to particle the microenvironmental variation is high, as sediment particles have different size, roughness, curvature and packing. Moreover, there are other bacteria present in the microsystem, whose presence might affect the swimming trajectories of the other bacteria hydrodynamical and/or biochemically, and which as well can hinder the tracking of individual bacteria.

Studying the swimming behaviour of MTB in sediment has implications both for MTB and magnetically actuated artificial microswimmers. Apart from the study of MTB themselves in their natural environment, several applications of these entities can be envisaged, such as bioremediation (as for example, for heavy metal recovery), targeted cargo for antibiotic delivery into biofilms [76], or navigation in capillaries for tumour targeting [77]. Such applications, though, require a fine tuning of the microswimmer motion if these are to be directed to specific locations. Many of these scenarios present restricted environments that will confine bacterial trajectories, such as mud in wastewater, pores in biofilms, cylindric capillaries, pores in sediment, etc. It is therefore crucial to understand how each of these confined scenarios will affect the microswimmer trajectories and to establish accurate simulations of them.

Therefore, a platform where it could be possible to decouple several of the parameters that will impact the swimming behaviour and where such parameters can be easily defined and tuned would be highly beneficial to further understand how these entities interact with their physical microenvironment. For that reason, in the present chapter a microfluidic system is proposed where individual bacteria can be trapped in micrometer sized containers of defined sizes and volumes, such that no interaction between cells exists. This removes any hydrodynamic and biochemical cell-to-cell interaction, and allows to attribute any changes in the swimming behaviour to tunable external parameters (wall curvature and magnetic field) and to a parameter intrinsic to the bacterium (its swimming speed).

The microfluidic platform that is presented in the following pages tackles the presented problem and is, as the previous one, based on glass and PDMS. Nevertheless, in contrast to the previous one, this microsystem is a double-layered device, which permits a supplementary level of control over the system (actuation via pressure) that will allow single-cell entrapment in picoliter-sized cylindric volumes.

5.2. Objectives

The objective of this chapter is to design a microfluidic platform that allows to isolate single magnetotactic bacterial cells in picoliter volumes of defined size and shape, and track them over time to study their swimming dynamics and interaction with walls under different magnetic fields.

5.3. Materials and methods

5.3.1. Materials

M. gryphiswaldense bacteria, growth medium, master mould and microfluidic system components are specified in the *General materials and methods* section.

5.3.2. Silicon wafer production, microsystem fabrication and experimental set-up

An actuable double-layered microfluidic device was fabricated for the confinement of single-cells. As explained in the *General materials and methods* section, the fabrication of double-layered microfluidic devices requires two master moulds: one for the control layer and another for the fluidic layer, which were fabricated according to the standard methods previously defined. The master mould height for the control layer was set to 20 µm. On the other hand, the master mould for the fluidic layer, though, was created as a double-height mould, with heights 10 µm + 10 µm accounting for 10 µm high microchannels featuring 10 µm high cylindrical indentations in the microchannel ceiling (which upon actuation and contact with the glass bottom become the microwells). Soft lithography for two-layered microsystems was done according to the *General materials and methods* section, and the PDMS membrane thickness to separate the fluidic layer from the control layer was set to 20 µm, which means that, when spincoating the fluidic layer, a target height of 40 µm was sought, accounting for the sum of the fluidic layer height (10 µm + 10 µm) and the PDMS membrane thickness (20 µm).

For the operation of the microfluidic system, both the fluidic and the control layer were filled with growth medium by centrifugation (10 min at 900 RCF). The inlet of the fluidic layer was connected to a syringe via a needle, PFTE tubing and a metal connector; the syringe being placed on a syringe pump to deliver the required

amount of liquid onto the microfluidic device. The eight inlets of the control layer were connected through metal connectors and Tygon tubing to a pressure system, either a custom-built one with on/off valves (Figure 13), or an electronic one with pressure delivery regulation.

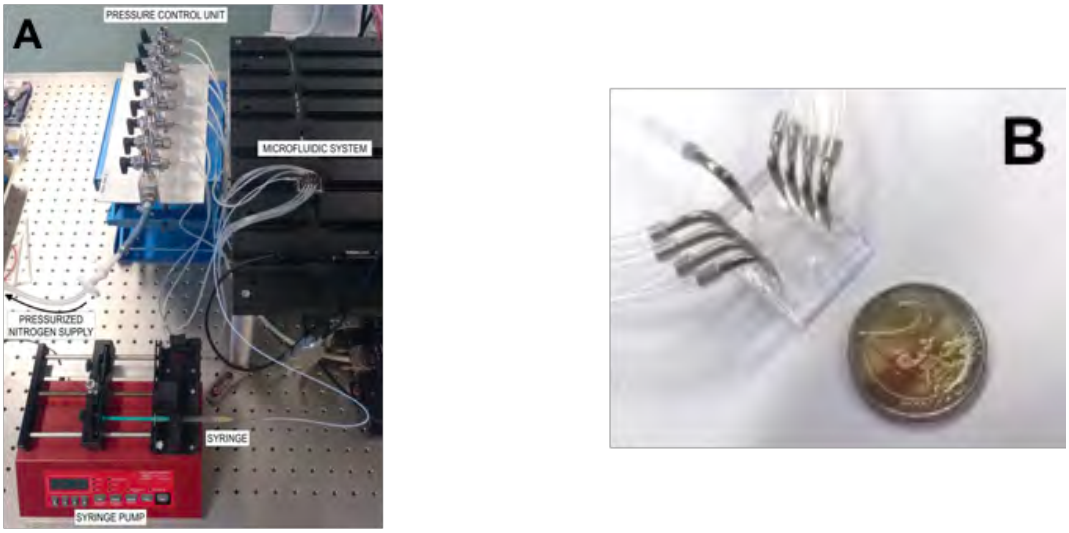

Figure 13. Microfluidic system set-up. (A) Microsystem connected to the liquid supply (syringe) and the control pressure unit. (B) Microsystem connected to the liquid supply in the fluidic inlet (central connector) and to the control pressure unit (eight lateral connectors).

5.3.3. Bacteria trapping and image acquisition

A bacterial suspension with the required OD_{565} was loaded into the microfluidic device at a speed of 5 µL/min. Once the bacterial suspension had reached the fluidic channels, the flow was stopped and the valves were actuated with a pressure of 1.75 bar, thus confining bacteria in the microwells. Five different microwell sizes (15, 25, 35, 50, and 90 µm in diameter) were examined. Each experiment was recorded for 40 seconds (2,000 frames with 50 fps). The experiments were repeated 5-8 times independently, with different microwells and bacteria for each trap size, which corresponds to roughly 104 total trajectory points. For the trap sizes 15, 25, and 35 µm, microwells with only one bacterium were selected to avoid bacterium-bacterium interactions. However, for sizes 50, and 90 µm the movies were recorded with a maximum of 2 and 3-4 bacteria inside, respectively. The microwells were opened and washed out every 10 minutes with fresh medium with bacteria to ensure no changes in medium composition nor bacterial physiology due to confinement.

Prior to each measurement, the magnetotactic behaviour of the bacteria was inspected by applying a rotating magnetic field of 1 mT to the sample. Only bacteria showing a magnetic field-dependent response were recorded for the measurements. The rotating magnetic field was shown not to alter the posterior swimming behaviour of the bacteria.

5.4. Results

5.4.1. Microfluidic system design and operation

As described in Figure 14, the trapping concept of the bacteria within the microwells relies on the elastic properties of PDMS thin membranes when a force is applied, which allow the vertical displacement of the fluidic layer ceiling along with its indentations until the glass bottom of the fluidic layer. When bacteria are present in the fluidic layer and the control layer is pressurised, the bacteria falling below the indentations get confined in the spaces created by the indentation upon contact with the glass bottom (Figure 14D). From now onwards, such confined volumes will be referred to as microwells. The actuation of the valves to close the microwells and confine the bacteria was achieved in less 500 ms (Figure 15), which allowed to start the measurements virtually instantaneously after the valve actuation.

While the microwells height was kept constant to 10 μm, their width was varied to obtain diameters ranging from 15 to 80 μm (Figure 16), which yielded in most cases microwells with diameters bigger than the expected values. However, the size of the fabricated microwells was consistent for every size (Table 3).

5.4.2. Bacterial trapping

The number of trapped bacteria per microwell followed a Poisson distribution (Figure 17), such that the concentration of bacteria (OD_{565}) in the growth medium supplying the microsystem could be modified depending on which microwell diameter was to be studied, in order to achieve a higher probability of getting one bacterium per microwell. For this reason, to perform the measurements, an OD_{565} of 0.2 was used for microwell diameters of 15 and 23 μm, 0.1 for diameters of 30 μm, and 0.05 for diameters of 45 and 80 μm.

As an example of the results this microfluidic platform yields, some results on the confined bacteria swimming are presented now. The experiments consisted of supplying the microfluidic system with growth medium containing the aforementioned density of *M. gryphiswaldense*, and then confining the bacteria inside the microwells. Microwells containing one single bacterium were chosen to subject the bacterium to different magnetic fields and then, its trajectory was analysed. There are two things to point out. The first is that magnetic swimming bacteria had been previously cultured in agar tubes (see *General materials and methods* section) to select for swimmers, had been allowed to form magnetosomes, and had then been again selected for magnetic swimming bacteria with a magnet. Moreover, previous to each measurement the magnetism of the bacterium had been ensured by applying a rotating magnetic field in the trapped bacterium and observing whether it responded to it. The second thing to consider is that, previous to any measurement, the microchannels had been filled with growth medium and allowed to incubate at room temperature during at least 30 min. Moreover, during the experiment course, the microwells were opened and new growth medium with bacteria was flushed to allow for exchange every 10 min. The reason for the incubation and the medium exchange was simply taken as a measure to ensure proper bacterial physiology throughout the whole experiment, and will be further commented in *Chapter 7*.

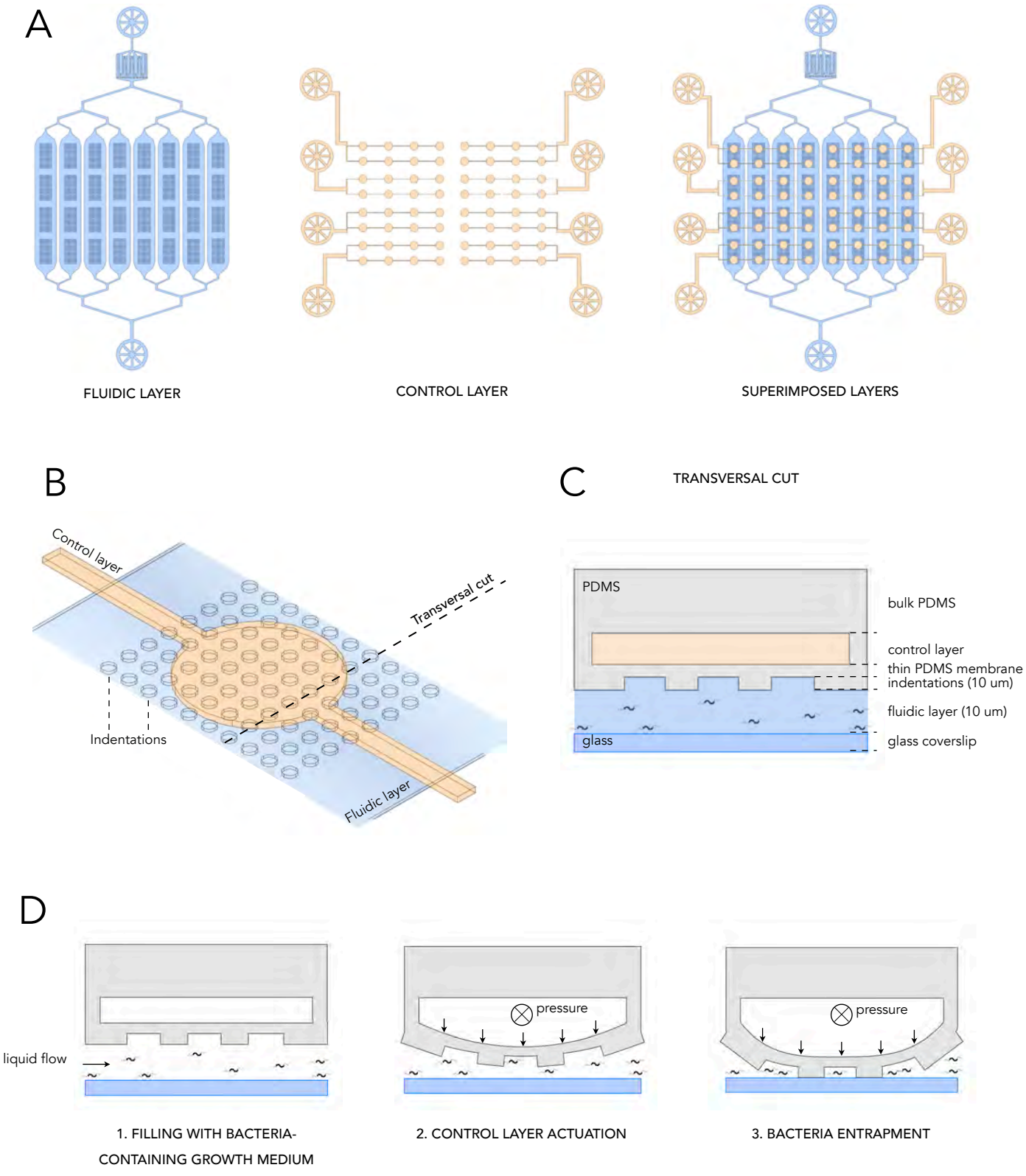

Figure 14. Microsystem structure and mechanism of action. (A) Sketches of the fluidic (blue) and control (cream) layer and their superimposition after device assembly. The fluidic layer features one inlet and one outlet, whereas the control layer features eight inlets and no outlets. (B) Zoomed sketch showing how the control layer (cream) and the fluidic layer (blue) are perpendicularly positioned with respect to the each other. The control layer present a valve which falls directly on top of an array of indentations present on the ceiling of the fluidic layer. (C) Transversal view of a cut in the microsystem (bold dashed line in B) that shows the architecture and order of the control later, PDMS membrane, indentations and fluidic layer. The colours are the same as in A. Please, bear in mind that the sketch has not been made to scale. (D) Transversal view showing the actuation mechanisms of the microwells. When pressure is applied on the top layer, the water that fills the microchannels is pushed creating a deflection of the PDMS membrane. When the pressure is high enough, the PDMS membrane is deformed such that the indentation enter in contact with the glass bottom trapping any bacteria below.

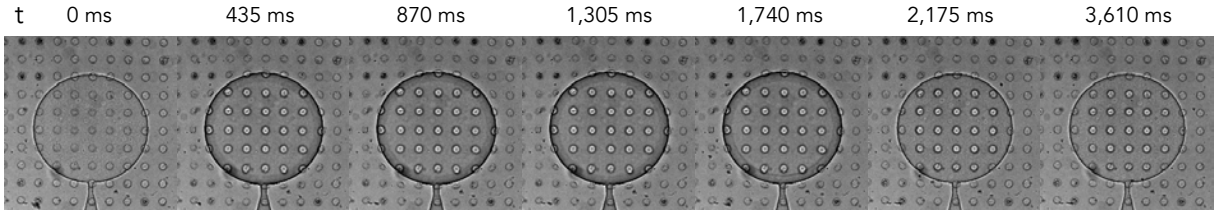

Figure 15. Actuation of a control valve. Transmitted light images showing the actuation of the valve (closure of the microwells) and the opening of the microwells over time for a pressure of 1,750 mbar. It is observed that, upon actuation, the valve changes its contrast compared to the fluidic layer, and that the contact area (that is, where the ceiling of the fluidic layer touches the glass bottom) appears as a lighter area in the centre of the valve surrounded by a darker rim where no contact takes place. As reference, the microwells are 30 µm in diameter.

Table 4. Theoretical and experimental microwell dimensions. Diameters and heights obtained from the measurement of the calcein filled microwell stacks. For each size, n = 11.

		Theoretical microwell diameter (µm)				
		15	**23**	**30**	**45**	**80**
Measured microwell diameter	Mean (µm)	14,85	26,52	35,80	52,13	90,88
	SD (µm)	1,04	0,44	0,42	0,65	1,05
		Theoretical height = 10 µm				
Measured microwell height	Mean (µm)	11,19	11,52	11,62	10,73	8,50
	SD (µm)	0,38	0,28	0,28	0,31	0,36

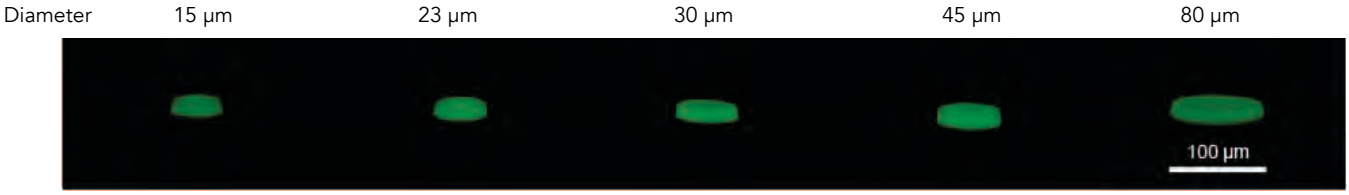

Figure 16. Reconstruction of the different microwell sizes. The microwells had been filled with calcein to obtain fluorescent stacks for the microwell reconstruction.

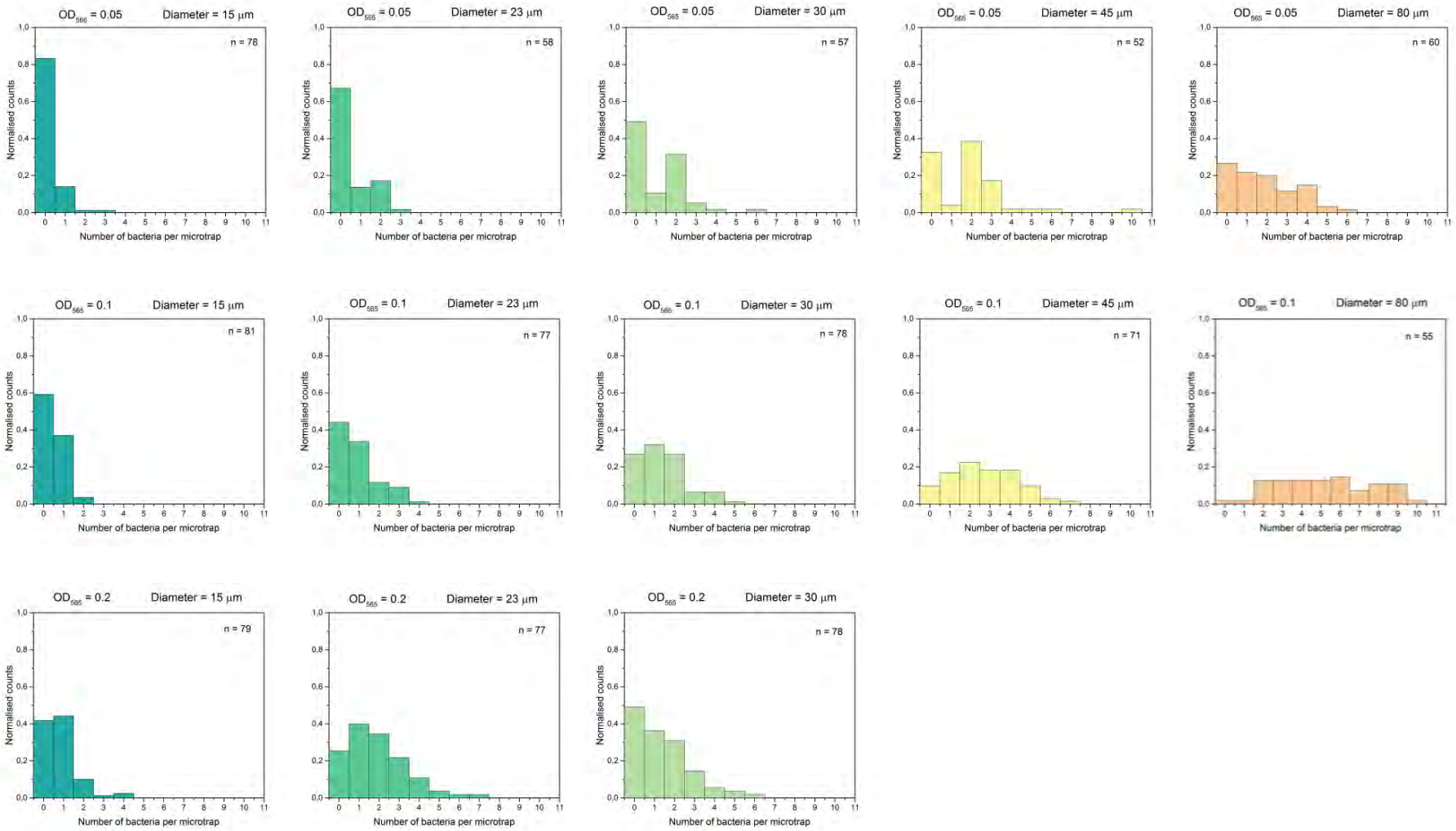

Figure 17. Normalised counts of bacteria per microwell for different microwell diameters and bacterial densities. The histograms show the amount of bacteria per microwell for different microwell diameters (15, 23, 30, 45 and 80 µm from left to right) in each column, and optical densities (OD_{565} = 0.05, 0.1 and 0.2, from top to bottom) in each row. The histograms for the biggest diameters for the most concentrated sample are missing as in such cases the high concentration of bacteria made complicated the quantification of bacteria per microwell.

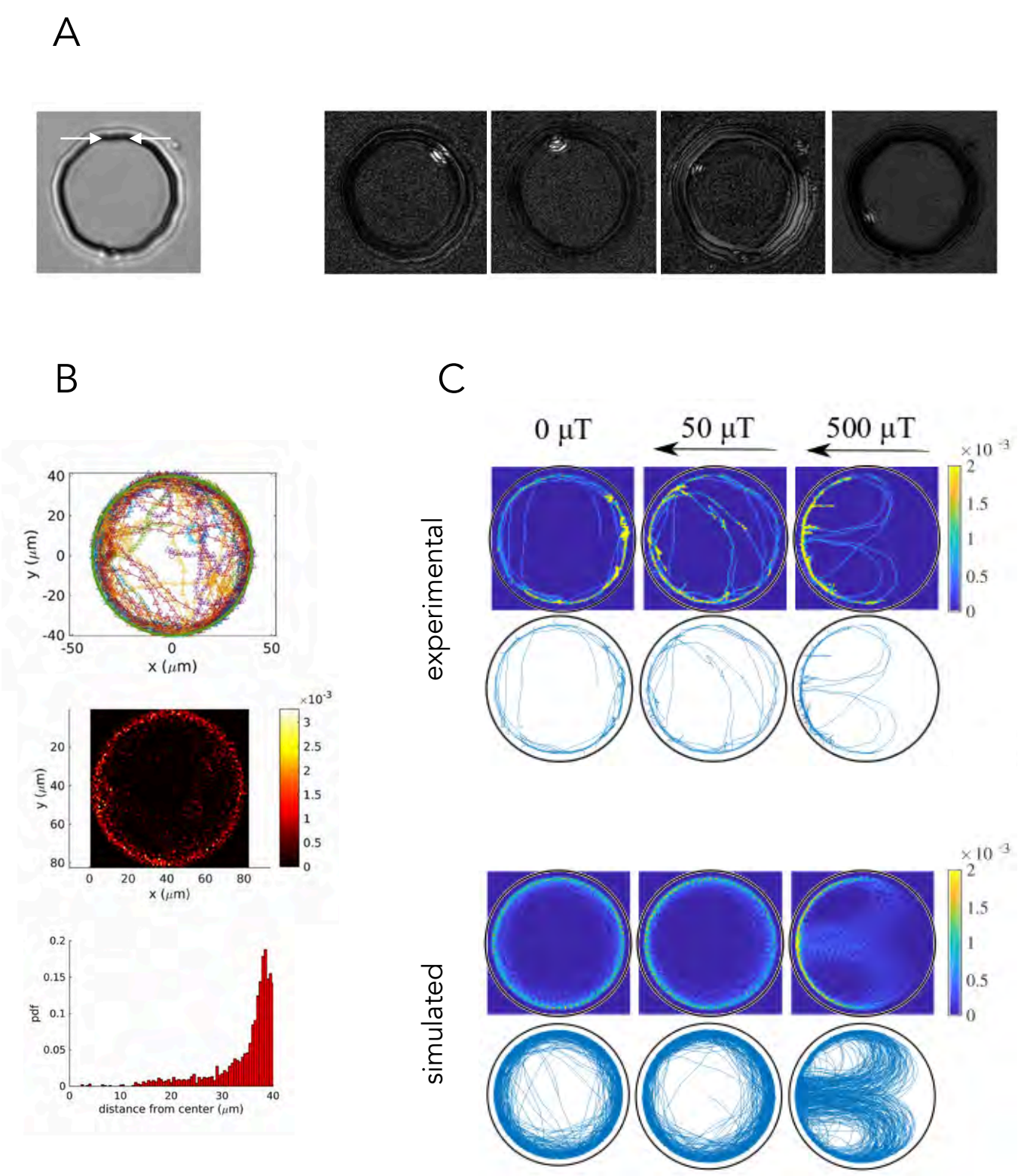

Figure 18. Bacterial trajectories in the microwells. (A) On the left, transmitted light image of a microwell bearing a single bacterium. The bacterium edges are pointed by the arrows. On the right, different frames of the same microwell after background subtraction. The bacterium can be then spotted in white. The diameter of the microwell was 15 μm. (B) On the top, trajectories performed by a bacterium under no magnetic field in a 80 μm diameter microwell. In the middle, heat plot showing the frequency with which the bacterium was present in the different locations of the microwell. On the bottom, distribution showing the frequency with which the bacterium could be found at different distances from the centre of the microwell. (C) On top, experimental trajectories performed by a bacterium confined in a 80 μm diameter microwell under different magnetic fields (B = 0, 50 and 500 μT). On the bottom, simulated trajectories performed by the same bacterium in an analogous microwell. The figures were provided by Mohammad Charsooghi and Agnese Codutti.

Interestingly, upon entrapment, the bacteria showed for every microwell diameter a swimming pattern with trajectories mainly curved, following the microwell wall (Figure 18). This was in stark with the observed in bulk, which are linear with some turns known as U-turns [78]. The bacteria trajectories were seen to be mainly confined to the microwell walls, that is, the bacteria tended to swim close to the microwell edges with fewer runs going through the middle of the microwell, even though enough space was available for the bacterium in the centre of the microwell. However, the runs through the centre of the microwell were observed to increase with increasing microwell sizes (data not shown). Moreover, it was observed that the confinement of the trajectories performed by the bacterium was not only defined by the wall curvature and the swimming speed, but were as well dependent on the strength of the magnetic field. Overall, it was observed that increasing swimming speeds, increasing wall curvatures (decreasing microwell diameters) and increasing magnetic fields contributed to the bacterium confinement (data not shown). Furthermore, the bacterial confinement with different magnetic fields resulted in swimming patterns due to a deviation of the initial trajectory of the bacterium, which was forced to spend more time in the centre of the microwell. Consequently, it was seen that certain areas that were frequently occupied by bacteria at lower or without magnetic fields, were devoid of bacteria upon application of a high magnetic field, whereas in some previously empty areas the bacterial presence became more prominent (Figure 18C).

5.5. Discussion

Other double-layered platforms similar to this one, but with different purposes, such as lipid vesicle trapping or bioanalyte detection, have previously been fabricated [79-82], being this one inspired in a system for trapping lipid vesicles [81]. Some platforms to confine single motile objects (both living and inert) have as well been developed [83, 84]. Such systems share similarities to the presented on as they created as well cylindrical volume for micropropellers. Such propellers featured different propelling mechanisms (a motile algae vs. laser-actuated silica microspheres), whereas the microsystems were made out of PDMS or SU-8. Also, the trapping mechanisms were virtually different as no actuable microfluidic system is involved, but rather relied on sandwiching. In any case, such platforms allow to compare the swimming dynamics of two different microorganisms highly dissimilar in shape (spherical for the algae *vs.* spirillum for the present bacterium) and whose propelling strategy is as well different (pusher *vs.* puller, respectively), as well as with the laser-propelled (pushed) spherical geometry. Interestingly, the comparison shows that these different systems do actually behave in a comparable manner when challenged with this specific confinement. This can be relevant when designing microswimmers or exploiting other microorganisms for targeted cargo-delivery as for such environment, when working in such a size range, any of both geometries (spherical or spirillum) and propelling strategies could be adopted, meaning that there would be more flexibility in propeller geometry choice. However, the use of magnetotactic bacteria allows to exert an additional level of control by magnetically actuating the microswimmers. In the case of the bacteria, their exact magnetic moment might be difficult to assess, making synthetic micropropellers more adequate if a homogeneous magnetic moment is required, but compared to a micropropeller, these bacteria are intrinsically motile, meaning that no external actuation is required for their motion to occur.

From an application side, the circular shape of the microwells is interesting as it is the shape of many pores, as well as capillaries. Moreover, it is especially easy to fabricate via soft lithography as the shape does not have edges. On the other hand, if other shapes are to be studied (squares, triangles, etc), a chrome mask might be needed, as the edges will require a higher resolution that might not be achieved through a film mask.

Independently of this, it should be noted that the platform offers a hint on swimming heterogeneity, as it allows to spot bacterial speed differences over individuals, and how this speed will impact on its sensing of the magnetic field and its ability to interact with the wall. Interestingly, from the experimental swimming pattern from the bacterium in Figure 18C, it can be determined that the bacterium is polar and that it is a North seeking one. Moreover the pattern observed indicated that it swam both in a clockwise (CW) and in a counterclockwise (CCW) direction. The interesting thing from this platform is that in the presence of a magnetic field, if a bacterium is magnetic and polar, it can be clearly defined whether the bacterium is swimming CW or CCW (Figure 19). This makes it is possible to use the platform as well to study with a single-cell resolution the time spent by one bacterium in both modes when in a constant oxic concentration, where no gradients are present. CW and CCW swimming motions are of special importance for these bacteria as they generally swim linearly. This means that when they want to swim back and forth, they will not re-orient themselves and swim always with a given cell pole ahead, but will rather reverse the flagellar propulsion without re-orienting their bodies, and the front pole will become the rear one, and vice-versa. For this reason, the present microfluidic platform could be used to study the time spent in both modes in aerobic or in anaerobic conditions. Moreover, the fact that bacteria with different polarities present different trajectories when subjected to certain magnetic field intensities, and that their trajectories get even more confined could be exploited in the future for targeted swimming of the bacteria in pores or capillaries, as their trajectories can be partially predicted according to their polarity, meaning that it is possible to confine the bacteria to differential areas of the volume in a timely-ordered manner.

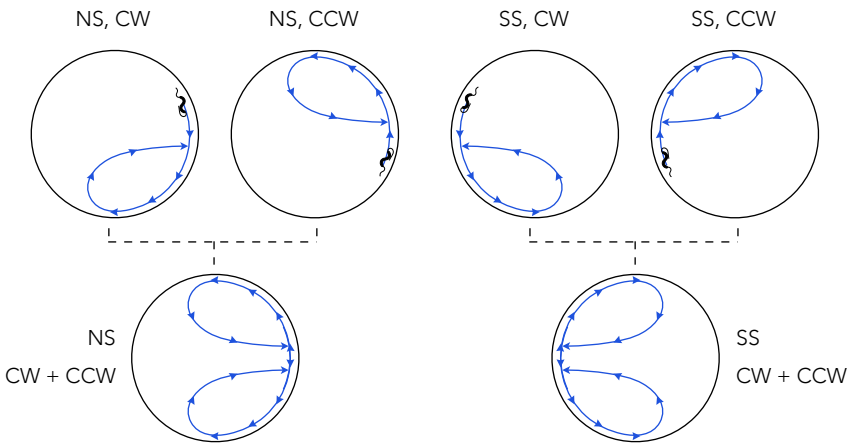

Figure 19. Bacterial trajectories for polar *M. gryphiswaldense*. The sketches depict the different trajectories that a North-seeking (NS) and a South-seeking (SS) magnetic bacterium would perform when responding to magnetic fields. In addition, the trajectory that would take place if the bacterium is swimming by moving its flagella clockwise (CW) or counterclockwise (CCW) is depicted. The overlay of the CW and CCW trajectories for each bacterial polarity is shown in the two bottom sketches.

As it was indicated before, during the course of an experiment, the microwells were opened and flushed with fresh growth medium to ensure the growth medium composition did not vary inside the microwells (this subject is further addressed in *Chapter 7*). There are two things to to consider in this regard: concerning the volume of the microwells, we know that even in the smallest microwells (15 μm in diameter), the amount of nutrients is sufficient and that waste accumulation is not enough to compromise the bacterial motility and viability within the experiment timespan (in *Chapter 8*, it is observed that smaller volumes can sustain bacterial motility for several days). For this reason, it can be ruled out that the size of the microwells will have any impact on the viability. However, as PDMS can absorb some hydrophobic molecules [85] and there can be osmolarity shifts due to water vapour evaporation [86], it was preferred to replace the growth medium periodically every 10 min to ensure that the growth medium composition and concentration inside the microwells is always constant for the measurements.

Finally, as discussed in the previous chapter, the surface chemistry as well as roughness of the microsystem material can have a significant effect on the bacteria interaction with the surface, which on its turn can lead to different swimming behaviours (such as swimming or adhesion) depending on the Young's modulus and the surface chemistry: if there is a strong interaction with the surface, the swimming speed of the bacterium could be slowed down. Consequently, and for the future, this platform could eventually be used by functionalising the glass and PDMS surfaces with different coatings such that different surface chemistries are screened within the same constant physical microenvironment. This would allow to extract a set of parameters to understand how different surface chemistries can affect the bacterial interaction. This could be used to gain a broader understanding on how the bacteria will behave upon encountering certain obstacles with certain characteristics, and also to understand the swimming in more complex environments, like the sediment, where different surface chemistries are encountered.

5.6. Conclusion and outlook

In the present chapter, a double-layered PDMS-based microfluidic device was designed to isolate single magnetotactic bacteria in defined volumes to study the interaction between the swimming speed, the magnetic field and the wall curvature without having any interaction from other bacteria and to simplify the tracking of the bacterium. The device was based mainly in two separate sets of microchannels that could be actuated to create an array of microwells. In the same way the microsystem was implemented to study *M. gryphiswaldense*, it could be potentially implemented to study other MTB species as well as other microswimmers (natural or synthetic) in very defined conditions where it it possible to isolate them and track them individually over time. Moreover, given the defined and miniaturised size and shape of the microwells as well as the possibility to isolate single-cells, other uses can be envisaged for such platform, such as the realisation of bioassays in single-cells, as it is discussed in *Chapter 7*.

6. Visualising the intracellular chemical microenvironment: towards *in vivo* studies of magnetosome formation

The present microfluidic platform was designed to visualise the dynamics of magnetosome formation in individual *M. gryphiswaldense* MSR-1 cells through through X-ray studies. For X-rays studies, the microfluidic system has to be repurposed and adapted to the synchrotron set-ups. This project arises from a collaboration with Daniel Chevrier. The microsystems were designed by myself; the microsystem fabrication, by both; the X-ray fluorescence (XRF) measurements, by both, and the XRF data analysis by Daniel Chevrier.

6.1. Introduction

In the previous chapters, two different devices arose from the need to understand the bacterial interaction with its microenvironment at the physical level to study the swimming characteristics attributed by magnetotaxis. Magnetotaxis, though, would never be possible without the presence of the magnetosome chain inside the bacterium. The magnetosome formation process has been extensively studied and much is currently known about the conditions that trigger magnetosome synthesis, the level of control the bacterium exerts onto the nanoparticles' formation, the iron mineral intermediate phases, or the proteins involved in the process [2, 13, 87].

Yet there are still major discrepancies on what looks like a very simple question: how long does it take for a magnetosome chain to be synthesised? Simple as it looks, this unknown still generates controversy as claims in very different time scales (from minutes to hours) have been presented [18, 88-90]. This lack of consensus which, with little doubt, emerges from the lack of having identical starting conditions or a highly controlled environment, calls for a strategy to properly clarify what is the actual time delay necessary to synthesise a magnetosome chain.

Having a clear view of the time scale it takes to synthesise the magnetosome chain can give information about the rate at which the cellular machinery works, the time it takes to nucleate and mature the iron nanoparticles, and how different conditions can have an impact this rate.

To date, most of the studies performed on magnetosome growth dynamics have been performed as *ex situ* end-point measurements usually via TEM [18, 88, 91, 92], as a routine technique for magnetosome observation, which allows for individual assessment of the magnetosome content in each cell. Besides TEM, other techniques such as X-ray dichroism or small angle X-ray scattering have been as well used to study magnetosome biomineralization [19, 90], but these techniques usually require high amounts of sample, which makes impossible to resolve magnetosome biomineralization with a single-cell resolution. Moreover, the mentioned techniques do not allow for *in vivo* dynamic measurements as the samples need to be retrieved from the culture, sometimes processed (drying, fixing) and then analysed. Consequently, there is a time delay decoupling the iron uptake, the

formation of the magnetosomes, and their observation. To temporally resolve the formation process and understand its kinetics it would be therefore ideal to observe *in vivo* in one single-cell through the whole formation process. However, it should be taken into account that MTB are motile by nature, so that they have a tendency to swim when free. This implies that tracking a specific one during a whole measurement might be complicated, and that data acquisition might be compromised by the continuous bacterium repositioning. Nevertheless, such individually resolved measurements have already been attempted by using *in situ* liquid cell TEM [93, 94]. However, as the techniques used for this purpose heavily rely on high energy sources, *in vivo* measurements are highly compromised due to damage caused by ionising radiation [95].

In this context, this chapter addresses the construction of a microfluidic platform aiming to reduce the gap between the actual state of the art and the ideal target experiment by providing a microfluidic system where magnetosome synthesis can be studied *in situ* in immobilised living single-cells. The platform pursues to decrease the time gap decoupling bacterial harvesting and magnetosome examination while preserving bacterial viability until the moment of the measurement. This allows to extract end-points of magnetosome synthesis in an individual-directed fashion and over the course of time, expecting that this gives a picture of the different frames that constitute the synthesis of magnetosomes. It is therefore shown how by adapting one part of the previous microfluidic system, a platform for the study of magnetosome synthesis by X-ray fluorescence (XRF) can be manufactured. By playing with the different microchannel dimensions, design, coating strategies and microsystem materials, it is shown how the previous microwell design can be adapted to fit a synchrotron configuration to study the bacteria in a completely different way, both from the instrumental perspective as well as from the information to be gained from the measurements. By doing some slight adjustments, we glide from the physical perspective dealing with the interaction of single-cells with their environment towards the chemical study of the intracellular environment of single-cells from a chemical perspective, to study the iron nucleation and the formation of magnetosomes.

6.2. Objectives

The objective of this project is to adapt a previous microfluidic platform to make it compatible with XRF studies and synchrotron set-ups to immobilise magnetotactic bacteria and perform semi *in vivo* XRF measurements to study magnetosome formation at the single-cell level.

6.3. Materials and methods

6.3.1. Materials

As microsystem substrates, Kapton film (150 µm thick) and Si_3N_4 windows (10x10 mm; 200 µm thick (Si), 200 nm thick (Si_3N_4)) were used and purchased from DuPont (Germany) and Plano (Germany), respectively. Poly-L-lysine (PLL) (0.01% (w/v) in milliQ water, sterile-filtered) for bacterial immobilisation was purchased from Sigma-Aldrich (Germany). (3-mercaptopropyl)trimethoxysilane and (3-glycidyloxypropyl)trimethoxysilane (GOPTS) were purchased from Merck. *M. gryphiswaldense* bacteria, growth medium, master mould and microfluidic system components are specified in the *General materials and methods* section.

6.3.2. Facilities

I14 Hard X-Ray Nanoprobe beamline in Diamond synchrotron (Didcot, Oxfordshire, UK).

6.3.3. Silicon wafer production and microsystem fabrication

The master mould was produced with a film mask to obtain features 10 μm deep, and soft lithography was subsequently employed to create the microsystem PDMS-based part; a more detailed explanation on both processes is described in the *General materials and methods* section. The bottom of the microsystem was constituted by a Kapton 150 μm thick film or a Si_3N_4 window.

It is important to point out that, in this chapter, microsystems made out of PDMS-Kapton, as well as PDMS-Si_3N_4 were used. In order to bond the PDMS slabs to the Kapton substrates a modified protocol based on silanisation was used [96]. PDMS and Kapton were plasma activated during 1 min and were subsequently immersed during 20 min in 1 % (v/v) (3-mercaptopropyl)trimethoxysilane in methanol and in 1% (v/v) GOPTS, respectively. They were then washed with milliQ water and dried under a stream of N_2. Both functionalised surfaces were then brought into contact and irradiated with UV light for 10 min to allow the formation of a covalent bond; the assembly was then placed under some weight during at least 1 h. In the case of the PDMS-Si_3N_4 microsystems, the substrate was first coated by depositing a PLL drop (0.01% (w/v)) on top of the substrate, and was allowed to dry. Once dried, the coated substrate and the PDMS slab were plasma activated and subsequently brought into contact to covalently seal the microchannels and get the finished microsystem.

6.3.4. Surface coating and bacteria immobilisation

The bacteria were immobilised into the surface through a PLL coating. In the case of Kapton-PDMS microsystems, a 0.01% (w/v) PLL solution was incubated inside the microsystems during 20 min and was then rinsed twice with HEPES 10 mM pH 7.0 previous to their filling with bacteria. The PLL functionalisation of the Si_3N_4-PDMS microsystems has been described just above, and was performed even days before using the devices. Growth medium containing *M. gryphiswaldense* cells was loaded into the device at a flow rate of 0.01 $\mu L \cdot min^{-1}$, flow was stopped and bacteria were allowed to settle onto the PLL. Once the bacteria had been immobilised, fresh growth medium devoid of bacteria was supplied at a constant flow rate of 0.01 $\mu L \cdot min^{-1}$ during the whole length of the experiment, which would be running for several hours (>6 h). Bacteria with or without magnetosomes could be both immobilised depending on the sort of measurements that were to be performed: for studying magnetosome growth, iron-starved bacteria were immobilised to ensure that no magnetosomes are present at the start of the measurement.

6.3.5. Set-up and spectra acquisition

The microsystem was connected via the inlet and outlets through metal connectors plugged into PFTE tubing. The inlet tubing was connected to a plastic syringe mounted on a syringe pump. The syringe was filled with fresh medium and was used to constantly feed the microchannels with fresh medium at a flow rate of 0.01 $\mu L \cdot min^{-1}$ during the course of the whole experiment. The medium going through the outlet tubing was collected into an Eppendorf tube. Moreover, a constant N_2 flow was constantly applied throughout the whole measurement on top of the microsystem to reduce the O_2 concentration in the microsystem.

The XRF mapping in the Diamond Nanoprobe beamline was performed with an incident energy of 9 keV with a 100 nm beam, with the X-ray fluorescence signal being collected with a 4-element detector from the incident energy down to 1 keV. High resolution maps were taken with a 2.5 µm x 2.5 µm scanning area, a step size of 50 nm and a pixel dwell time of 10 ms per point.

6.4. Results

6.4.1. Microfluidic system design and set-up

The two microfluidic systems presented in this chapter had their base made in two different materials (Kapton and Si_3N_4) other than a common glass coverslip. Standard glass coverslips are 170 µm, but have a high content of zinc in their composition, and might bear as well other impurities, thus interfering with the XRF readouts [97]. Kapton (a polyimide) and Si_3N_4 windows are typically used for XRF measurements as they do not present the same interference problem as standard glass coverslips.

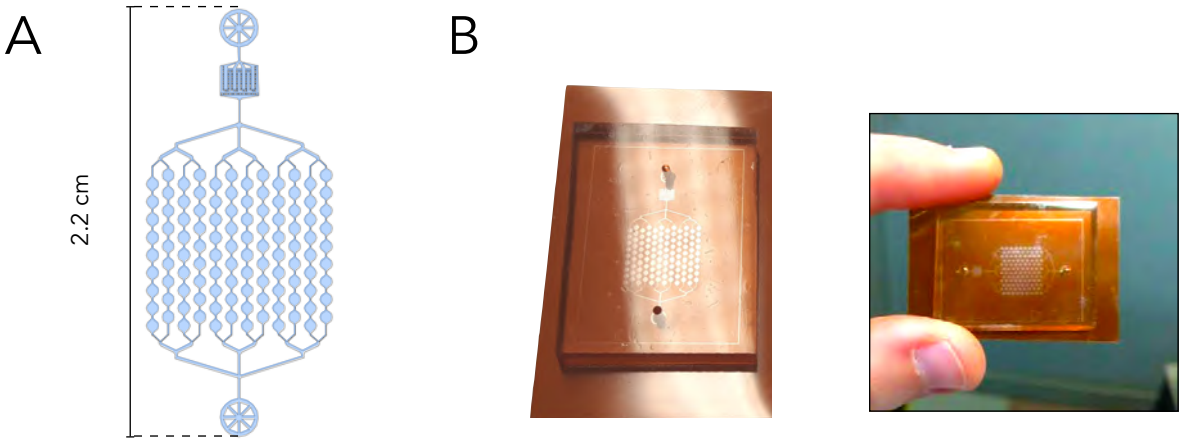

Figure 20. Kapton microsystem design. (A) Sketch of the microsystem. The blue area represents the microchannels. (B) Pictures of the microsystem composed by PDMS-Kapton. The Kapton has an orange colour.

The microchannel height should to be as shallow as possible to reduce the background signal coming from the growth medium present in the excitation volume. In this case, the height was always kept to 10 µm as this height had been created previously in the lab with no problem. Therefore, the thinner the fluidic layer, that is, the layer with growth medium where the bacteria are immobilised, the lower the background that will be acquired, as no iron signal will be coming from the bulk PDMS. It should be noted that originally the microfluidic systems were envisaged for the BESSY mySpot beamline (Figure 20), which allows for much bulkier microsystems than the Diamond Nanoprobe beamline. However, the latter one can offer a resolution down to 50 nm, in comparison to the mySpot beamline, which could achieve a resolution down to 1.5 µm. Consequently, the experimental set-up and the microsystem design had to be adapted to be compatible with the Nanoprobe beamline (Figure 21), which had very restrictive space limitations and was therefore not compatible with the original microsystems. It is important to note that different synchrotrons have different set-ups to which the

A

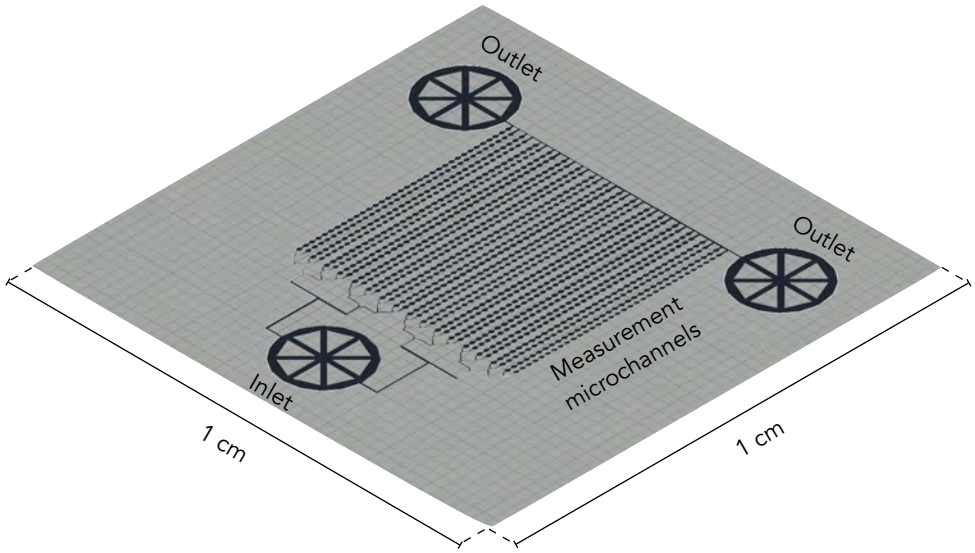
Outlet
Outlet
Measurement microchannels
Inlet
1 cm
1 cm

B

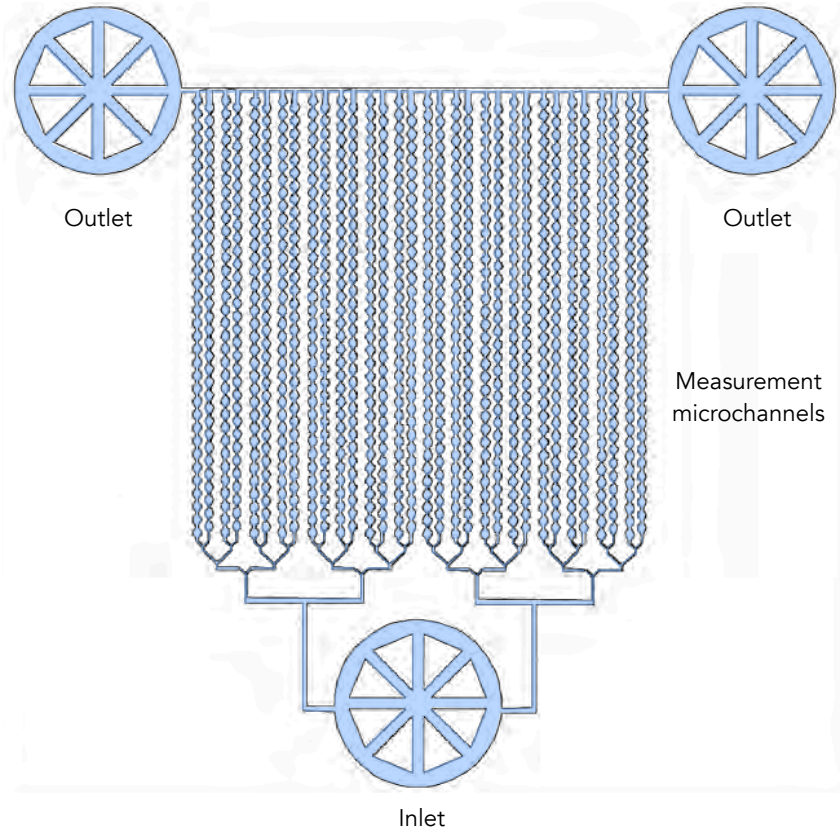
Outlet
Outlet
Measurement microchannels
Inlet

C

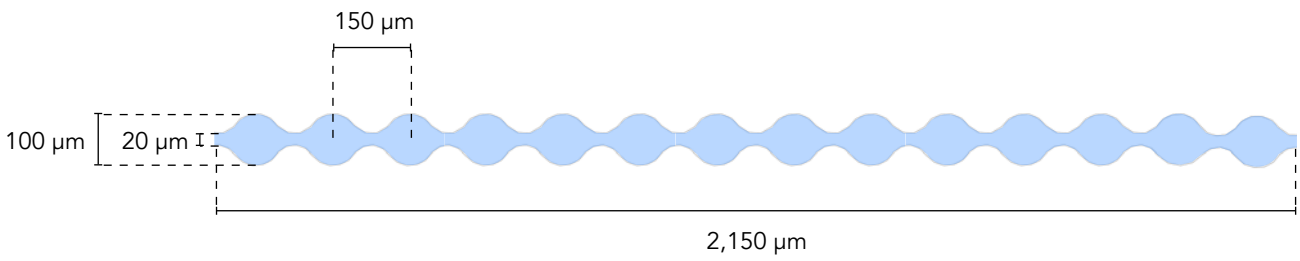
150 µm
100 µm
20 µm
2,150 µm

Figure 21. Si_3N_4 microsystem design. (A) Sketch of the microsystem. Slice of the same height as the microchannels representing the PDMS in grey, and the microchannels in black. (B) Top view of the microchannels (shown in blue). A set of 32 measurements microchannels featuring microchambers is presented. An inlet is used to supply the medium, and the flow is retrieved by two outlets. (C) Zoomed region of a measurement microchannel showing the microchamber-shape it features. The microchamber enables an easier navigation of the microsystem to distinguish regions of PDMS *vs* regions of liquid.

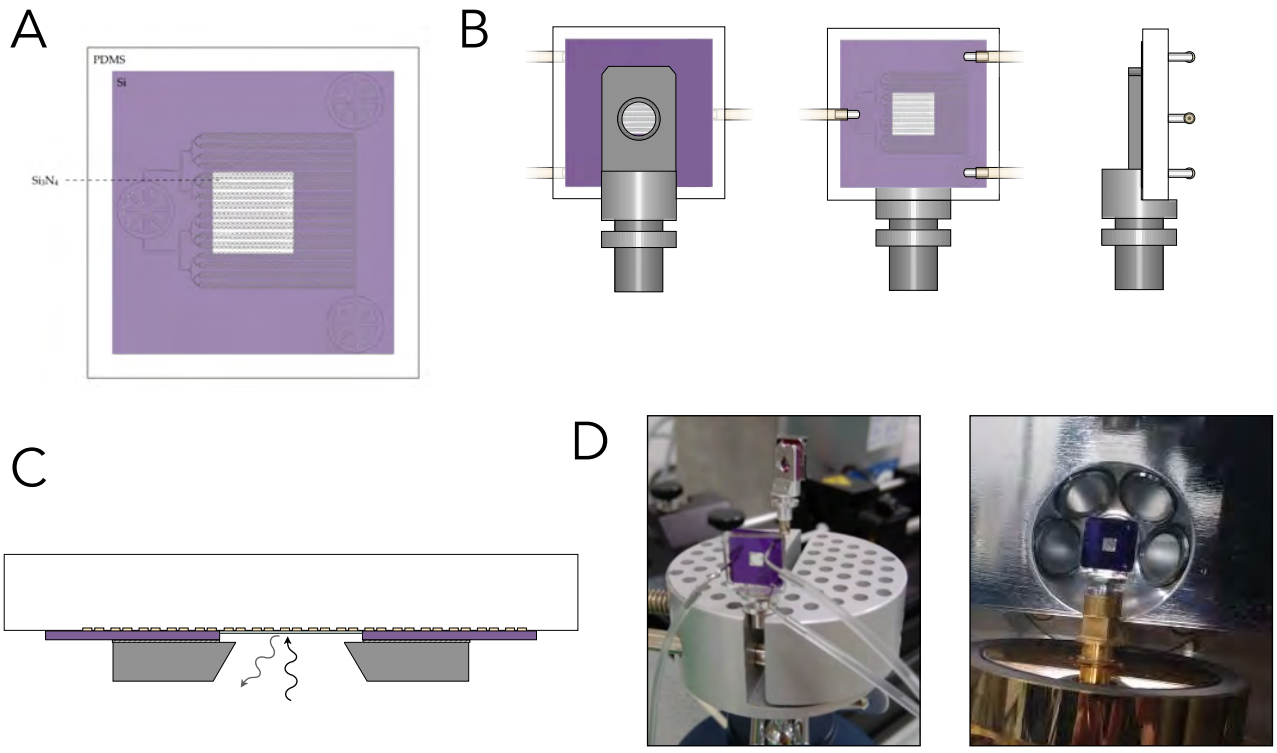

Figure 22. View of the microfluidic system inside the beamline. (A) Sketch of the top view of the microfluidic system, which is opposite to the beam and the X-ray detector. (B) Top, bottom and side view of the microfluidic system mounted on the sample holder (grey) with the inlet and outlet connections shown. (C) Transversal cut of the mounted microfluidic system. In A, B and C PDMS is shown in white; the silicon substrate of the Si_3N_4 window is shown in purple, and the Si_3N_4 window is shown as a transparent square in the centre of the purple substrate. B and C show as well the sample holder (grey) with a circular reading window, which is in contact with the silicon substrate. Moreover, in C the microchannels are shown (cream) as well as the X-rays. On a layer of double-sided tape is as well present (black-white stripes). (D) The first picture shows a mounted microsystem with the tubing connected into it. The second picture shows the microsystem with no tubing placed in the XRF set-up.The sample holder base is fixed into the hutch via a magnetic contact.

experiment has to be adapted, this being true for any experiment in general, of course, but with the particularity that synchrotrons generally have a more restricted sample set-up; particularly in terms of geometrical constraints. It should also be noted that, since beamtimes are not quickly granted, measurement times are scarce throughout the year and highly restrictive. This means that there is not a high margin of trial-error to try different settings as these are not places easily available nor accessible. For that reason, in this case the set-up design had to be thoroughly before its implementation as there would be little room for variation and improvement.

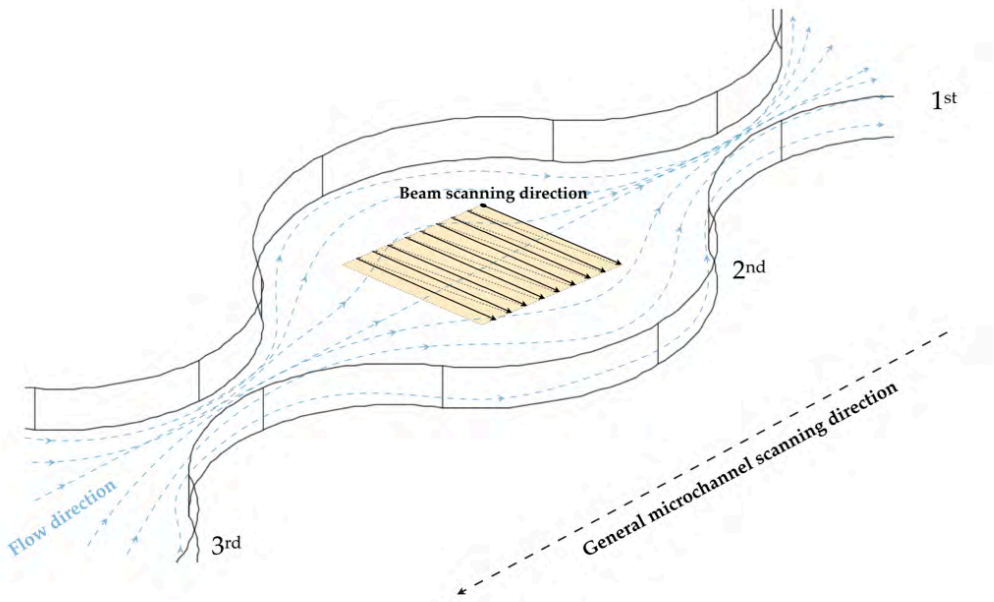

Figure 23. Beam scan direction. Sketch depicting the flow direction inside the microchannels (blue), the beam scanning direction (black) in a scanned area (yellow), and the order of chamber scanning (represented by the ordinal numbers). The microchamber is 100 μm wide, as indicated in Figure 21.

Originally, previous to the Diamond Nanoprobe beamline, a microfluidic system was designed for the BESSY mySpot beamline. Such microfluidic system was adapted from the microwells system described in the previous chapter, and it exclusively featured its fluidic layer, that is, an array of microchannels, but no actuable control layer (Figure 20). In such microsystem, the substrate was made of Kapton, which is a polyimide that is commercialised as film sheets of different thicknesses, and which is a suitable material for X-rays studies due to its X-ray transmittance as well as to its resistance to radiation damage. As the Kapton-PDMS coupling is not straightforward, the Kapton surface had to be functionalised and then bonded to the PDMS via click-chemistry. However, the Kapton film did not allow to obtain a clean transmitted light image as it absorbs visible light below 500 nm [98], thus making it difficult to observe the bacteria within the microchannels (data not shown). As it is of main importance to be able to locate the bacteria in the microchannels to determine where to perform the measurements, Kapton was discarded as bottom material. For that reason, when transitioning to the Diamond Nanoprobe beamline, Si_3N_4 was chosen as alternative material to fabricate the bottom of the microfluidic channel as it would be optically compatible not only with X-rays, but also with visible light to easily locate the bacteria inside the microfluidic system.

As stated before, synchrotrons have set-up restrictions and, in this case, the sample size that could be fit was very limited. In the Diamond beamline the microsystem has to be mounted onto a specific sample holder and had to be placed vertically (Figure 22). This restricted the size, weight and position of inlets and outlets of the whole microfluidic system, as well as the measurement operating window and the waste placement. The previous microfluidic systems had a size of roughly 2 cm x 3 cm x 0.5 cm, but unfortunately, such dimensions were simply too large for the new intended set-up. For that reason, when redesigning the microsystem, even though the structure of microchannels formed by chambers was kept in order to facilitate recognition of the microchannels during the measurements, the whole microsystem size had to be adapted. The size of the microfluidic system was

shrunk to 1 cm x 1 cm x 0.25 cm, being 1 cm x 1cm the dimensions of the silicon substrate on which the Si_3N_4 window is located. Moreover, the PDMS layer was kept very thin to reduce the microsystem weight. The microchannel height was kept to 10 µm with the chambers' width being 100 µm and the junctions among chambers being 25 µm wide. The microsystem was composed by 16 5mm-long microchannels arranged in a parallel fashion each featuring 34 chambers (Figure 21). The connections to the exterior were provided by one inlet and two outlets. It should be noted that the actual measuring window, that is, the Si_3N_4 window, has a size of 2.5 mm x 2.5 mm. This means that there is an excess of microchannels, but this was used to account for any possible misalignments and to ensure that as many chambers as possible fell within the reading window. Moreover, the presence of inlets and outlets allowed for the continuous flow of growth medium, which played a very important role not only in bacterial nutrient availability and waste product flushing, but also in relation to the scanning direction. The microchambers were scanned in the opposite direction to the liquid flow (Figure 23) in order to flush away any reactive species derived from X-ray irradiation to ensure that not-yet-measured bacteria were not subjected to such reactive species, as it could be highly detrimental for their physiology.

6.4.2. Bacterial immobilisation and XRF measurements

In order to elucidate whether there would be a distinguishable iron signal in the microfluidic systems and to assess their compatibility with the detection of iron, a 100 µM $FeCl_3$ solution was assayed to map different regions of the microsystem. As seen in Figure 24, when mapping a region with both the fluidic channel and the PDMS walls, a higher contrast indicating the detection of iron was observed in the area corresponding to the microchannels, whereas the PDMS walls presented a negligible signal. The other peaks present in the signal arose from silicon and argon. The argon peak was seen in both locations with the same intensity and arose from the air between the detector and the microsystem substrate. On the other hand, the silicon peak had a different

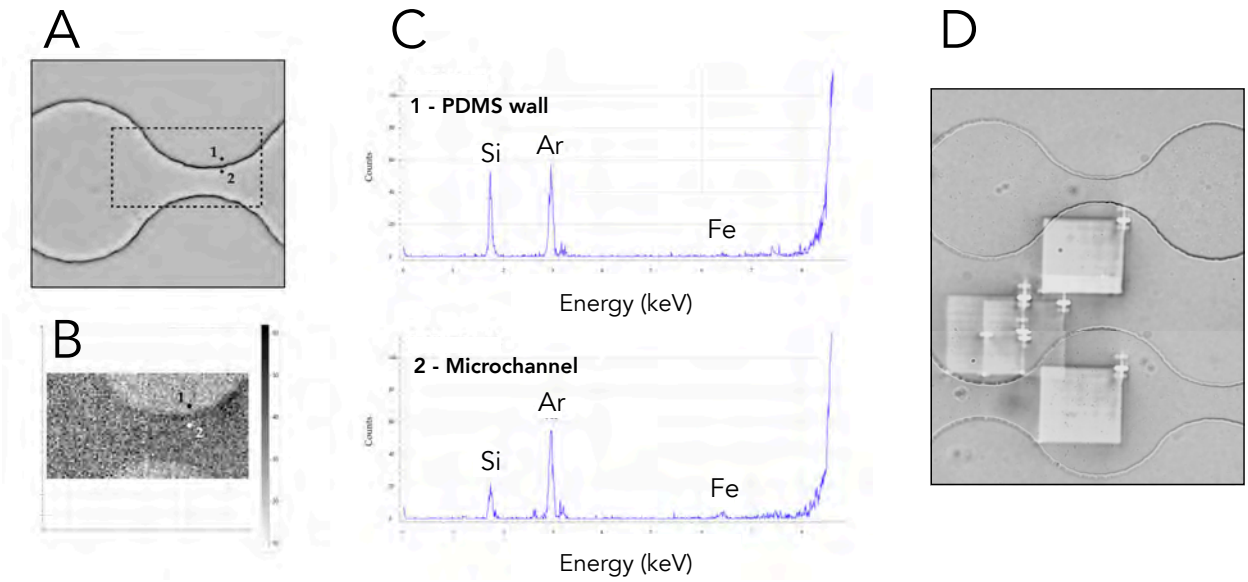

Figure 24. XRF mapping of a region hosting the fluidic channel and the PDMS wall. (A) Transmitted light image of the fluidic channel; the dashed line indicates the scanned area. (B) Iron intensity mapping of the scanned area. (C) XRF spectra arising from the PDMS wall and the microchannel (indicated in A and B by numbered dots). (D) Transmitted light image showing different areas after scanning (lighter square areas). The microchamber is 100 µm wide, as indicated in Figure 21.

intensity. The silicon is present in the Si_3N_4 window as well as in the PDMS; moreover, the mapped location inside the microchannel (2) would have in any case PDMS on the top, therefore, it is expected to see the silicon signal all over the microsystem.

When scanning an area in which immobilised bacteria bearing magnetosomes were present, it could be observed a higher iron signal which correlated with the presence of magnetosomes (Figure 24). It was also observed as well that after scanning a given area, it can easily seen by transmitted optical microscopy the area the X-ray beam has scanned (Figure 24D). For that reason, it should as well be specified that each area was scanned just once, and then the beam was moved towards the next area, to ensure that the bacteria that were read were still viable. Moreover, as depicted in Figure 23, it is important to note as well the way the scanning direction takes place in relation to the growth medium flow in the microchannels: the scanning of an area is performed in the direction opposite to the growth medium flow; the same is true for the general scanning inside the microsystem, where the chambers within a microchannel are scanned in a sequential order opposite to the flow.

As a proof-of-concept that bacteria with magnetosome chains can be observed with the present set-up, and also to initially calibrate the system, the images presented in Figure 25 were taken. It can be seen a set of immobilised bacteria with already full grown magnetosome chains, loaded with buffer (HEPES 10 mM) and having the device in static mode (that is, no flow). This verifies that bacterial iron could be observed with this new set-up, which appears as dark areas in the XRF image (Figure 25B,C).

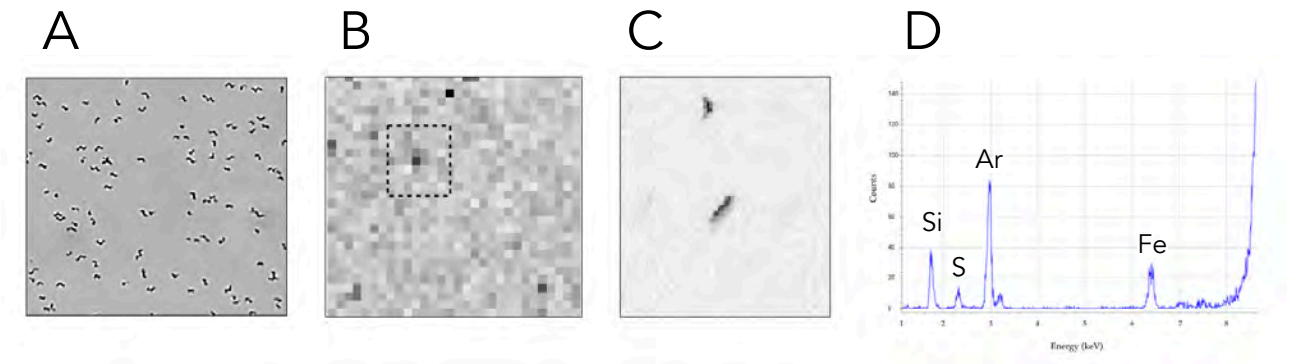

Figure 25. XRF mapping of immobilised bacteria bearing magnetosomes. (A) Transmitted light image of the fluidic channel with the immobilised bacteria. (B) XRF coarse mapping of the immobilised bacteria. (C) XRF fine mapping of the immobilised bacteria, where a bacterium can be seen in the center. (D) XRF spectrum in one of the high contrast pixels corresponding to the magnetosome-bearing bacteria. The sulphur signal comes from the presence of sulphur in the buffer (HEPES) as well as from the bacterium).

6.5. Discussion

The microfluidic system hereby presented was developed by adapting the fluidic layer of the microfluidic system presented in the previous chapter to obtain a system compatible with the *in situ* study of magnetosome biosynthesis via XRF. Therefore, the design was adapted from one intended to study the physical microenvironment to another intended to study the inner chemical microenvironment, all at the single-cell scale. For this, several considerations had to be made: the first of them is using a material that is not only transparent to

X-rays, but also to visible light in order to facilitate the navigation in the microsystem as well as the visualisation of the bacteria. In terms of the microchannel depth, the height was kept to 10 μm as shallow microchannels were intended in order to minimise the background signal arising arising from the growth medium. Given the fact that a 10 μm height is easy to fabricate and that from experience it was known that the fabrication of channels of such dimensions should yield proper results, the height was kept to 10 μm rather than trying to make the microchannels shallower. For shallower microchannels, moreover, the width of the chambers should be as well decreased to prevent the collapse of the structures.

It should be noted as well that the chamber configuration, despite being very practical to find the microchannels boundaries with the X-ray beam, had a main drawback when it came to the bacterial immobilisation. It is important to remember that the bacteria need to be immobilised to performed these measurements, as otherwise bacteria would swim away and no signal would be obtained from them. Bacteria are typically immobilised through chemical fixation or through drying on TEM grids or other substrates; however, such strategies kill the bacteria, thus making impossible to perform semi *in vivo* measurements, which was the aim of this platform. Consequently, alternative options which do not compromise the bacterial viability need to be used, such as trapping in a hydrogel matrix, i.e. agarose, or by immobilising onto a surface via electrostatic interactions with a cationic compound, such as PLL. From both strategies, surface coating with PLL was chosen as the surface of the microchannels can be easily coated with a solution of the polymer, whereas using a hydrogel would imply to have some liquid solution that gels inside the microchannels and which is not disrupted upon the constant supply of fresh growth medium. When the bottom of the microchannel is coated with PLL it will present a net positive charge such that, when the bacteria come into contact with it, as they have a net negative surface charge they will interact with the PLL and get immobilised on the surface. It is important to note that, even though bacteria can survive while immobilised on such surface, their viability might be compromised depending on the cationic polymer length used as they can alter the bacterial physiology and even show antibiotic activities [99, 100]. For that reason, it is recommended to check the viability of the bacteria and their motility after different times upon immobilisation. Going back to the initial issue of the chamber configuration impact on bacterial immobilisation, it seems that, as the liquid flows faster through the narrower junctions that connect the chambers, the bacteria are pushed by the flow in these junctions so in a flow focuser so that the probability of them sticking to the rest of the chamber is lower. This results in uneven distributions of bacteria throughout the microchannels. Consequently, to achieve a more even distribution of bacteria, a straight microchannel design might be more adequate than a chamber-like configuration.

The most important feature of the presented platform was that it allowed to keep the bacteria alive until the very moment of the data acquisition, therefore allowing a semi *in vivo* measurements. This is in stark contrast with the platforms that have been proposed until now to study the *in vivo* dynamics of magnetosome formation by TEM with liquid cells [93, 94], as they use closed platforms. In closed volumes, the bacteria will be subjected to ionising radiation and, even if not directly subjected to it, the vicinity of them will, potentially having a detrimental impact on the bacteria. However, the present system allows to circumvent the presence of any reactive oxygen species caused by the radiation by constantly flushing fresh growth medium in the opposite direction to which the system is scanned (Figure 22). The beam is positioned first in the part of the measuring window closest to the outlet for the first scan; then, the beam is moved to the next chamber on the same stream, which will be closer to the inlet. This will prevent the bacteria in the following measurement from being in contact with the reactive species caused during the previous measurement, as they will be flushed away towards the

A

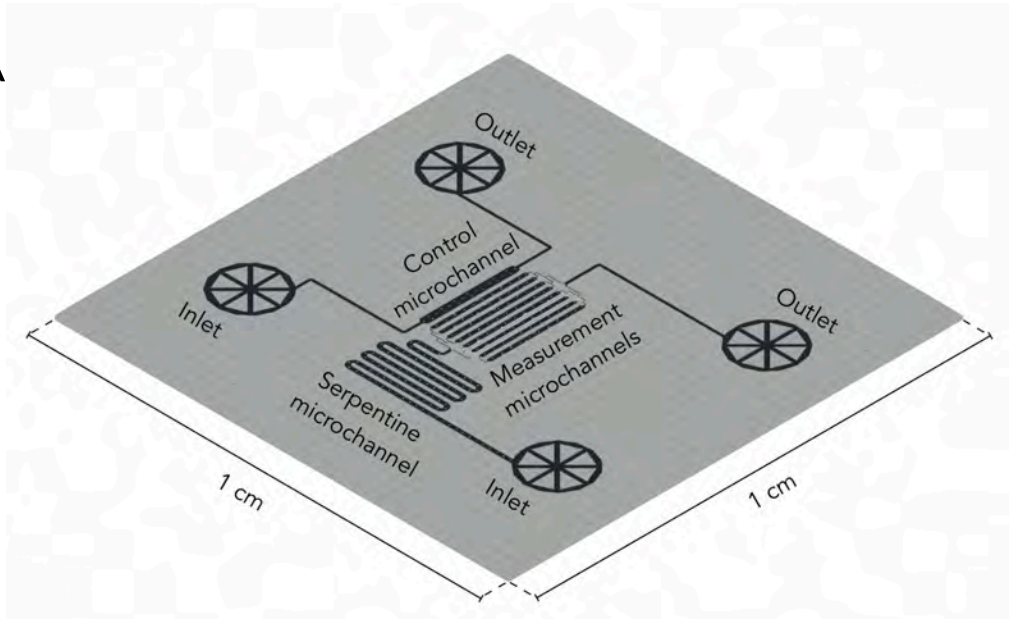
Outlet
Control microchannel
Inlet
Measurement microchannels
Outlet
Serpentine microchannel
Inlet
1 cm
1 cm

B

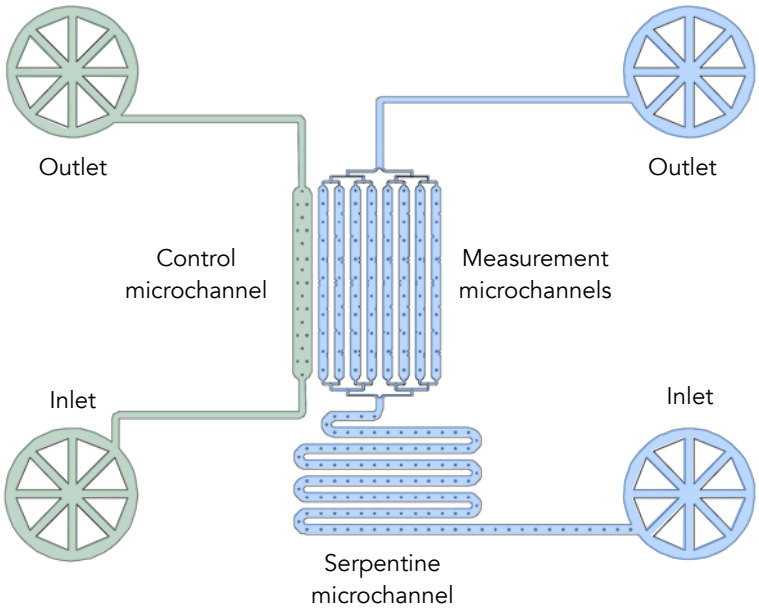
Outlet
Outlet
Control microchannel
Measurement microchannels
Inlet
Inlet
Serpentine microchannel

C

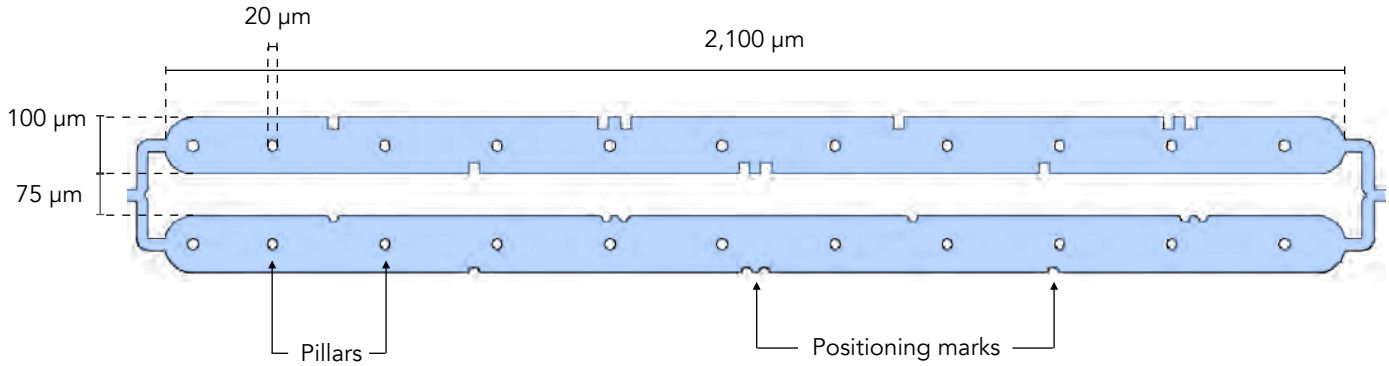
20 µm
2,100 µm
100 µm
75 µm
Pillars
Positioning marks

Figure 26. Improved microsystem design. (A) Sketch of the microsystem. The grey area represents the PDMS, whereas the black region represents the microchannels. It is cut of the same height as the microchannels. (B) Top view of the microchannels (shown in green and blue). Two independent sets of microchannels are shown: the control microchannel (left, green) and the measurement microchannels (blue, right), each set supplied by one inlet and and out outlet, respectively. The control microchannel is 200 µm wide, whereas the measurements ones are 100 µm wide. Notably, there is a reduction in the area occupied by the microchannels, a widening of them, straightening, and decrease in their number and length. It differs as well from the previous design on the presence of pillars, indentations on the walls, and a serpentine microchannel prior to the measurement microchannels. (C) Zoomed region of a measurement microchannel showing its straight shape as well as the presence of pillars.

outlet. Moreover, the fact that there are different independent microchannels where the bacteria are immobilised gives an additional level of protection against the reactive species, as the medium present in one of the microchannels will not be in contact with the medium present in the other ones. This allows to perform longer scans within the same device without compromising the viability of the yet non-scanned bacteria.

An improved version of the presented microfluidic system has as well been designed and been recently tested in the future during new synchrotron measurements (Figure 25). The new design differs from the presented one in the following aspects: (1) the microchannel amount has been reduced to the measuring window area, as the rest of the channels cannot be read, even though before there were so many to account for misalignments, (2) the microchannels are straight, rather than microchamber-like, to improve an even adhesion of bacteria in the whole microchannel area, (3) a independent microchannel where already magnetic bacteria has been added will serve as a positive control, (4) distinctive features in each microchannels for an the easier navigation in the microsystem during the measurements have ben implemented, (5) the inlets and outlets are all positioned to the sides to account for the balance of the mounted microsystem, (6) a serpentine channel previous to the standard microchannels has been added to allow for de-oxygenation of the growth medium before it comes into contact with the immobilised bacteria (magnetosome synthesis does not occur under aerobic conditions), and (7) a second layer has been added to the microsystem, this layer (gas layer) is placed on top of the fluidic channels, is separated from them by a thin PDMS membrane, and is meant to be used to flow N_2 through it to create an anoxic-to-microaerobic atmosphere to allow the magnetosome synthesis.

6.6. Conclusion and outlook

In the present chapter, a single-layered PDMS-based microfluidic system similar to the the fluidic layer of the microfluidic system presented in the previous chapter was designed. However, as it was intended for the study the inner chemical microenvironment of *M. gryphiswaldense* via XRF, the glass bottom was substituted by an alternative material more compatible suitable for such measurements. The device allowed to immobilise the bacterial cells onto the bottom of the microchannels and keep them alive until the moment of the measurement, thus allowing *in situ* measurements, compared to previous studies where the bacteria are measured when no longer alive, or have been damaged over the course of the measurement. Therefore, is is suitable to study biomineralization in MTB and could be envisaged to be used in the future with other MTB species as well as with other biomineralization organisms, such as algae. In any case, the system can be used to explore timescales in which magnetosome nucleation takes place, and to study the uptake rate at which the cells internalise the iron. For that reason, in the next chapter an alternative platform to address such a question is presented so that both platforms can be complementary to study the time ranges that define magnetosome biosynthesis.

7. Visualising the outer chemical microenvironment: confinement of single-cells in microwells

The present chapter deals with giving an alternative purpose to the microfluidic system previously presented in *Chapter 5*. In this case, instead of studying the impact of the physical microenvironment, the device is intended for studying the change in the outer chemical microenvironment as a direct result of bacterial uptake, namely the iron uptake kinetics of single magnetotactic cells.

7.1. Introduction

The previous chapter dealt with a microfluidic platform to study the *in vivo* dynamics of magnetosome formation in *M. gryphiswaldense*. However, as it was already implied while discussing that system, even though iron nucleation can be monitored via XRF, there are still a number of open questions that are required to understand the dynamics of magnetosome formation. One of them being the time delay between iron uptake and the start of magnetosome formation which, in other words, is the coupling between the outer chemical microenvironment and the inner chemical microenvironment.

To monitor the chemical microenvironment perturbations caused by one single-cell there are three requirements to be accomplished:

1) having a system where the level of detection is sensitive enough to detect changes in environmental fluctuations,
2) being able to decouple the effects of each bacterium caused into the environment, and
3) being able to locate the bacterium during the whole measurement.

To fulfil the first requirement, given that the amount of iron that a single *M. gryphiswaldense* cell uptakes is on the order of some femtograms of iron, the detection system would need to be very precise to accurately determine how much the amount of iron varies in the environment given that the retrieval of such a small amount of material will be fundamentally negligible. However, this situation changes if it occurs within a sufficiently small volume. In this case, the perturbations caused by the removal of a small amount of matter might cause a difference large enough in comparison with its surroundings. This means that if a bacterium supposed to be able to uptake some femtograms of iron is placed in a downscaled volume in the picoliter range, and an iron fluorescent sensor is added to the solution, the fluctuations in iron concentration will be high enough to be fluorescently detected. Therefore, a small volume would be of great interest for such studies.

For the second and third requirements, a closed and defined environment is needed. Therefore, the three requirements can be translated in a picoliter sized volume where a single bacterium can be confined. In

Chapter 5, such a platform had been already discussed, fulfilling all these requirements. For this reason, the present chapter deals with using the same platform with a whole different purpose: monitoring the external chemical microenvironment, instead of the physical one, for whose purpose it had been used before.

The approach to achieve this is to make use of a fluorescent iron sensor, calcein, to be able to quantify at the single-cell scale the amount of iron that has been removed from the growth medium. Conventional techniques that have been used for the determination of the iron uptaken by MTB from their environment has normally been carried by ICP [101, 102] or by the ferrozine assay [17, 103]. These methods rely on sampling growth medium from the cultures and analysing them, so they do not provide direct data on time, but there is, again, a time delay, and they are characterised by being end-point measurements as they are destructive and they require *high* amount of material where a big population of cells is analysed at the same time as they are not sensitive enough.

Lately, flow cytometry has emerged as well as an alternative strategy to monitor the amount of the chelatable pool of iron inside single *M. gryphiswaldense* cells with calcein, even though further development is still needed [104, 105] as calcein is not recommended for cytoplasmatic iron quantification [106]. Recently, ICP-MS has been as well introduced to quantify the total amount of iron present inside single *M. magneticum* cells [107]. However, this approach is destructive, and can solely be used for end-point measurements. To overcome this situation, the present chapter proposes the use of the microwells in conjunction with an *in vivo* fluorescent-based assay to detect the iron concentration outside the bacterium which allows to perform dynamic measurements without compromising the bacterial viability nor destroying the sample nor retrieving growth medium.

7.2. Objectives

The objective of this project is to measure the iron uptake kinetics of a magnetotactic bacterium by using a microfluidic platform that allows to capture single cells in confined spaces of specific and reproducible dimensions. This is intended to be done by monitoring the outer chemical microenvironment of the bacterium by means of a fluorescent assay.

7.3. Materials and methods

7.3.1. Materials

All the materials are the same as the ones specified in *Chapter 5*, except for the addition of calcein, for the fluorescent quantification of dissolved iron, and 1-palmitoyl-2-oleoyl-sn-glycero-3-phosphocholine (POPC) to coat the microwells, which was purchased from Avanti Lipids Polar Inc. (Alabaster, AL).

7.3.2. Microsystem operation and calcein quantification

The set-up is analogous to the one described in *Chapter 5*, with some small variations concerning the solutions used. Only the variations are described here. The microsystem fluidic and control layer were filled with standard growth medium by centrifugation (10 min at 900 RCF). The solution of interest (generally growth

medium with calcein) was flushed into the microfluidic systems at a flow rate of 15 μL·min^{-1} for 10 min, after which the control layer was actuated and data recording was started immediately.

Iron quantification was performed through the quantification of calcein fluorescence as described in Figure 26. Imaging parameters are specified in the *General materials and methods* section, with a digital zoom of 0.75.

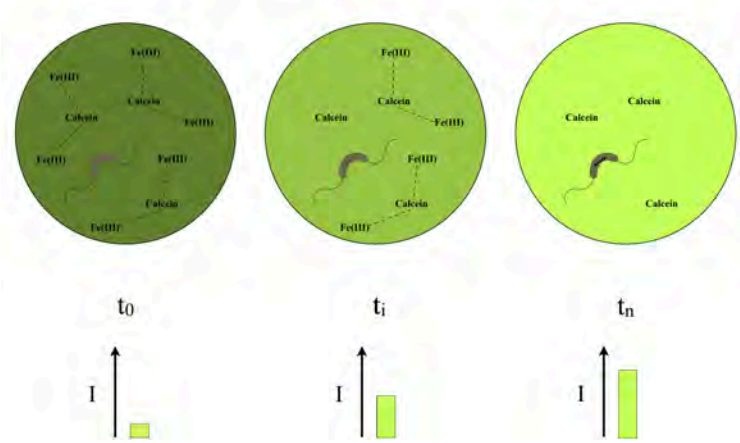

Figure 26. Iron uptake assay sketch. The figure shows the principle by which the dissolved iron is to be fluorescently quantified with calcein. At the initial stage, the bacterium has no iron inside, whereas its microenvironment has a given amount of iron coordinated to calcein. The fluorescence of calcein is quenched by the presence of iron. When the bacterium starts uptaking the iron from its microenvironment, less iron will be available to complex with calcein, whose concentration will be constant, and therefore less calcein will be quenched, giving a higher fluorescence signal readout.

7.4. Results

7.4.1. Microfluidic system and calibration curve

The total amount of iron available in each microwell size ranged from roughly 5 fg for the smallest size up to 140 fg for the biggest microwell diameter (Table 5) for an $FeCl_3$ concentration of 50 μM in the growth medium, which is the iron concentration used in standard MSR-1 growth medium. When creating a calibration curve for the calcein fluorescence vs the iron concentration, a linear relationship was observed for the concentrations of iron from 0 to 50 μM for a concentration of calcein of 25 μM (Figure 27A), indicating a coordination of iron:calcein 2:1, as previously reported [108]. The calibration curve performed inside the microwells yielded comparable results to the bulk ones for all the microwell sizes (Figure 27B), indicating that no effects due to the size of the microwell were taking place.

7.4.2. Growth medium component impact on fluorescence

The effect of the different MSR-1 standard growth medium components was studied by removing each one of the components (Figure 28). Only the removal of two components, sodium pyruvate and $FeCl_3$, yielded a

Table 5. Microwell dimensions and iron availability. The table gives the volumes for the different microwell sizes (all of them with a height of 10 µm) and the total mass of iron available in them for a $FeCl_3$ concentration of 50 µM.

Microwell dimensions		$[FeCl_3]$ = 50 µM
Diameter (µm)	Volume (pL)	Iron mass (fg)
15	1.77	4.94
23	4.15	11.59
30	7.07	19.74
45	15.09	42.14
80	50.27	140.37

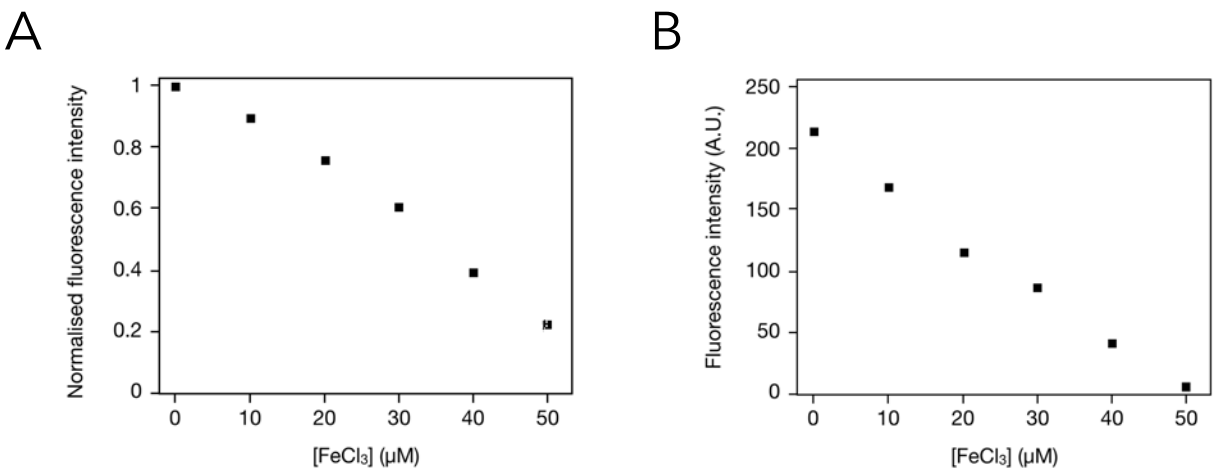

fluorescence increase in the solution. From these, $FeCl_3$ (50 µM) made the fluorescence increase by over 200%, whereas the removal of sodium pyruvate (27 mM) only increased the fluorescence by roughly 25% . Except for HEPES, which showed no effect on fluorescence, the removal of the remaining components always resulted all in a decrease of the fluorescent signal, with a more accused decrease for the soya peptone. In terms of solution colour, it was observed that calcein in buffer yielded a yellow solution, whereas it yielded an orange colour when added to the growth medium, except when no iron was present, case in which the solution remained yellow in colour. It should be noted that the removal of sodium pyruvate (27 mM) increased the fluorescent up to 25%, whereas the removal of $FeCl_3$ (50 µM) modulated the fluorescence by over 200%; in other words, despite the fact that sodium pyruvate modulated calcein fluorescence by a less than a fourth of in comparison with $FeCl_3$, the concentration of sodium pyruvate was 540 times higher than the one of $FeCl_3$.

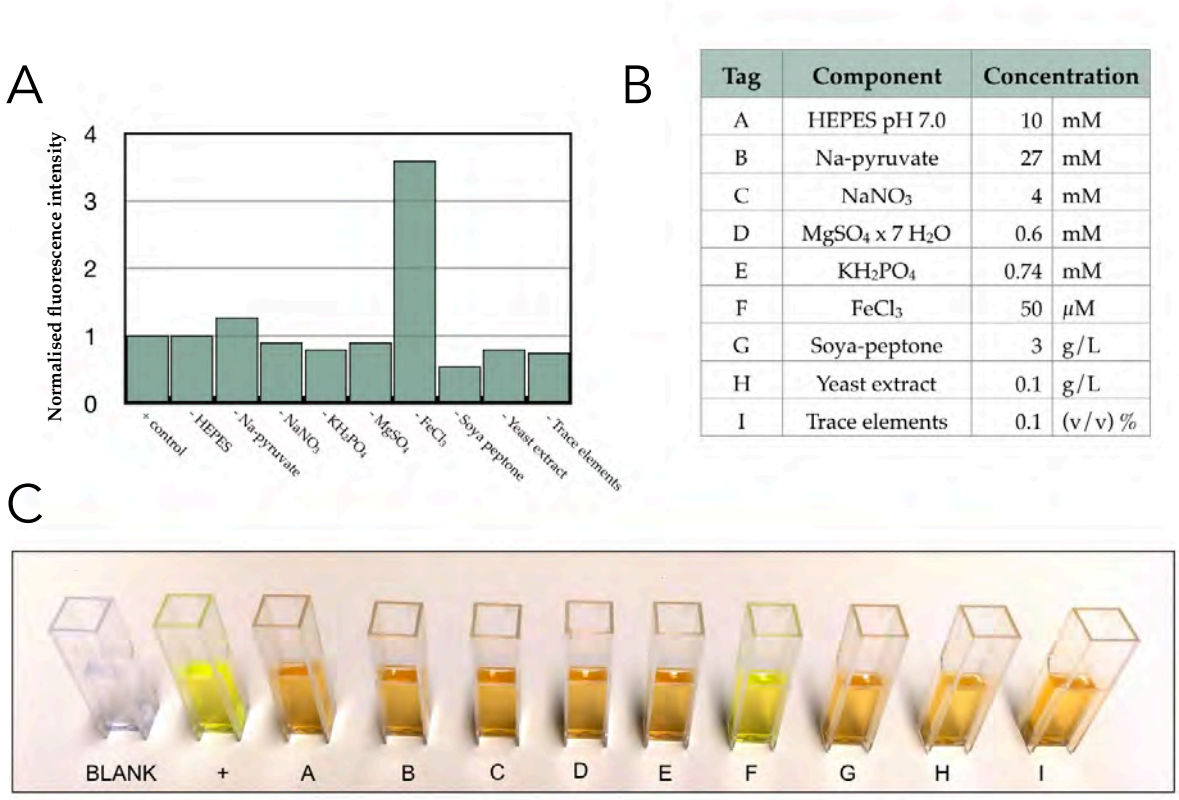

Tag	Component	Concentration	
A	HEPES pH 7.0	10	mM
B	Na-pyruvate	27	mM
C	$NaNO_3$	4	mM
D	$MgSO_4$ x 7 H_2O	0.6	mM
E	KH_2PO_4	0.74	mM
F	$FeCl_3$	50	µM
G	Soya-peptone	3	g/L
H	Yeast extract	0.1	g/L
I	Trace elements	0.1	(v/v) %

Figure 28. Growth medium components effect on calcein fluorescence. (A) Calcein fluorescence intensity upon removal of each growth medium component. The control had all the components. (B) Table indicating the concentration of each component in the medium. (C) A-I: Growth medium colour upon removal of each component. Blank: distilled water. +: positive control of calcein in water. Calcein concentration was always 25 µM.

7.4.3. Fluorescence readings in the microwells

When observing the microwells with bacteria and the growth medium with 25 µM calcein and 50 µM iron to assess the iron uptake by *M. gryphiswaldense*, it was observed that the fluorescence signal in the microwells increased over time until reaching saturation approximately 2 h after closing the microwells (Figure 29). However, it was observed that this signal was not dependent on the presence of bacteria in the microwells, as the signal increased as well when no bacteria were present. Unexpectedly, this effect was not observed when the microwells were filled with calcein in growth medium not containing any iron source. In any case, bacteria isolated in the microwells were observed to decrease their motility until not presenting any swimming behaviour after a few hours following the closure of the microwells. This was the main reason for which the microwells were opened and closed every 10 min when performing the bacterial swimming studies in *Chapter 5*.

To try to counteract this effect, two different strategies were tested: swelling the microsystem and coating the microchannel walls with lipids. Swelling the microsystem consisted in filling both the control and the fluidic layer with growth medium, incubate the microsystem during 1 h at room temperature, then rinsing with more solution and then starting the measurements as previously done. This strategy prevented the major fluorescent

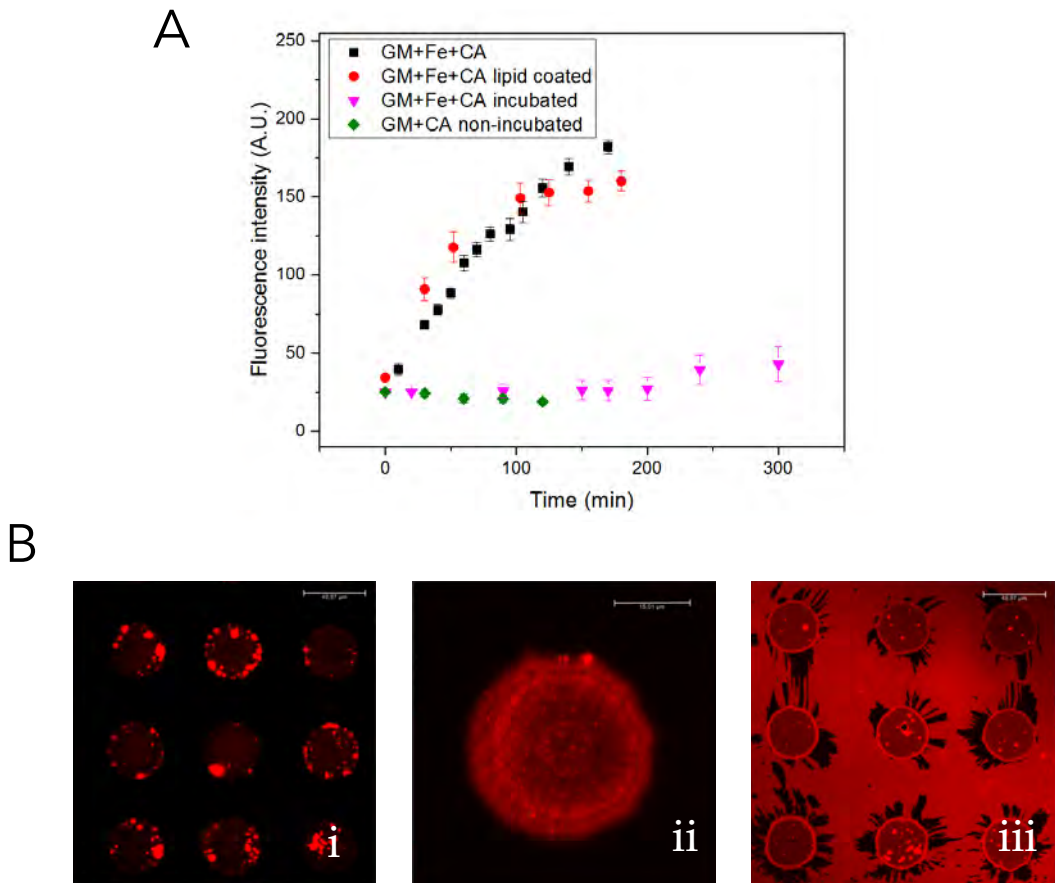

Figure 29. Calcein fluorescence evolution over time in the microwells and coating. (A) Calcein fluorescence intensity over time in the microwells filled with growth medium and calcein and: with 50 μM $FeCl_3$ and not swelled (black), with 50 μM $FeCl_3$ and previously swelled during 1 h (pink), with 50 μM $FeCl_3$ and coated with lipids (red), and without 50 μM $FeCl_3$ and not-swelled (green). (B) Fluorescent images showing the microwell lipid coating in red. In (i) the microwells are observed with some lipid vesicles inside them; (ii) shows the coated ceiling of a microwell, and (iii) shows the mud-crack like pattern in the lipid coating for the actuated microwells.

variations that had been previously observed and significantly delayed the time in which fluorescence started rising again (Figure 29A), postponing the fluorescence increase start to over 3 h, compared to the instantaneous fluorescence increase in the previous case. Moreover, the increase rate was significantly decrease. This should have been enough to detect fluorescence changes in bacteria uptaking iron in the smallest microtraps. However, as the exact reason for the fluorescence changes could not be determined, and as the exact change in environmental conditions for each component could not be exactly determined either, the impact this would have on bacterial physiology was unknown. Furthermore, this would have meant that results obtained in such conditions would not have been significant nor representative due to the lack of environmental control. Consequently, the strategy was discarded as it was critical to have a system with no fluorescence variations with control of the environmental conditions.

The second strategy consisted in coating the microchannel walls with phospholipids by bursting lipid vesicles inside the microchannels. This strategy provided a full coating of the microchannels, even though uneven (in the sense that all the walls were covered, but some had a denser lipid coating than others) (Figure 29B). However, fluorescence intensity kept on increasing over time as well (Figure 29A). Besides, this approach eventually resulted in lipid vesicles staying inside the microwells which could not be flushed out. Even though this seemed to be compatible with the bacterial viability as observed by their active swimming, it implied that the net volume inside the microwells could not be calculated exactly due to the lipid vesicle presence and that it varied from one microwell to another (Figure 29B), which was an undesirable feature as a precise iron quantification could only be performed in a well known volume. Moreover, upon pressurisation, the lipid coating in the pressurised PDMS surrounding each microwell started disappearing over time with a mud-crack like pattern. Whether this surface cracking had any link with the fluorescence intensity increase is unknown though. Consequently, this strategy was not adapted either.

7.5. Discussion

7.5.1. Growth medium effect on fluorescence

As observed in Figure 28, the removal of different growth medium components affected the fluorescence intensity measured at 514 nm. An increase in fluorescence upon removal of the component, indicates that the component was quenching the calcein fluorescence, whereas a fluorescence decrease upon removal, would indicate that the component was either intrinsically fluorescent or competing with calcein for iron. Autofluorescence within a non-photosynthetic, non-specifically-fluorescent standard cell, such as *M. gryphiswaldense*, generally arises from aromatic amino acids (tryptophan, tyrosine, phenylalanine), which have their fluorescence peak in the UV [109], and cofactors such as NADH and NADPH (with their peak in the blue) [110, 111], and flavins, such as FMN, FAD or riboflavin (with their peak in green) [112]. At a wavelength of 525 nm, in *E. coli* growth medium, it has been observed that over 80% of the autofluorescence proceeded from the flavins [113]. In the case of standard MSR-1 growth medium, both yeast extract and soya peptone are complex ingredients in the growth medium whose exact composition is undefined, but which in both cases originate from cell lysates. As cell lysates, they will contain the aforementioned fluorescent compounds and, more concretely, they will therefore provide green fluorescence to the medium due to the presence of flavins. As the flavins are present in an undefined concentration, will be consumed by the bacterium, might change redox state and might be degraded over time, it might be complicated to precisely assess their fluorescence contribution. Therefore, both the soya peptone as well as the yeast extract were omitted from the growth medium supplemented with calcein for quantification purposes, in order to avoid cross-readings.

Standard MSR-1 growth medium is as well supplemented with trace elements for the bacterial optimal growth [66], the presence of EDTA in the trace element solution might compete with calcein for iron coordination [114]. Consequently, more calcein would be free and unquenched, thus giving more fluorescence. On the other hand, the trace metal solution contains other metals that could as well get coordinated with calcein and would then create cross-readings. At pH 7, calcein gets strongly quenched as well by Co^{2+}, Cu^{2+}, Ni^{2+} and Mn^{2+} [115],

all present in the trace metal solution. Therefore, to avoid misreadings arising from these, the trace metal solution was as well omitted from the growth medium supplemented with calcein.

The presence of sodium nitrate, potassium phosphate and magnesium sulphate slightly increase the fluorescence of the medium, which might be ascribed to the observation that dissolved organic matter fluorescence intensity is slightly increased at higher ionic strengths [116]. A converse effect is observed for sodium pyruvate, which is in good agreement with previous reports that point towards fluorescence quenching due to the presence of pyruvate [117, 118]. Another key aspect of the calcein supplemented growth medium is that the standard iron source (Fe(III)-citrate) was replaced by $FeCl_3$, as citrate acts as an iron chelator that competes with calcein for iron. This said, when observing Figure 28, the component that has the highest impact on calcein fluorescent is with no doubt $FeCl_3$, meaning that the rest of variables can be deemed to have a minimal impact on the fluorescent readout as the whole component will not be totally consumed. Nevertheless, it could be as well thought that *M. gryphiswaldense* might secrete into its environment some flavins or other fluorescing compounds as well as redox active compounds or small organic acids that might interfere with the fluorescence readouts, but this is an uncertainty inherent to the measurement.

7.5.2. Growth medium effect on bacteria

The removal and/or substitution of the growth medium, which is optimised for the growth of *M. gryphiswaldense*, not surprisingly gives lower cell yields along with a slower growth rate. As soya peptone and yeast extract are sources of vitamins, amino acids and nitrogen, it is not surprising to thus observe such effect. The change from Fe(III)-citrate to $FeCl_3$ and calcein did not yield any remarkable effect on magnetosome biosynthesis, presumably because the iron stayed available for the bacterium with no interference from the calcein. It should be pointed out, though, that different chelating agents might impact the iron uptake of the bacterium, specially strong chelating agents, such as EDTA, might even prevent the bacterium from uptaking iron, as it has been reported in the magnetotactic spirillum *M. mageticum* AMB-1 [119]. However, the concentrations of chelating agent used in this thesis did not compromise the bacterial uptake.

7.5.3. Fluorescence over time

When confining the bacteria in the microwells along with the calcein supplemented growth medium, an increase in the fluorescence signal should have indicated that either iron had been uptaken from the bacterium microenvironment, so that a higher proportion of calcein is free, that is, unquenched. However, as depicted in Figure 29, the fluorescence intensity increased over time despite the absence of bacteria in the microwells, which points to an external cause microsystem-related strongly influencing the signal. Plausible explanations are: 1) the concentration of iron had decreased, either by sequestration by other species, by leaving the compartment, or by converting itself into another phase (precipitation); 2) the amount of calcein had increased; 3) the amount of flavins had increased; 4) an anoxic atmosphere had been reached; 5) iron on its reduced form had been produced; 6) a lensing effect was taking place;.

PDMS thin films have been previously used to fabricate microlenses [120, 121], meaning that the deflection of the PDMS control layer upon actuation could actually cause a lensing effect inside the microwells. However, given the fact that the microwells were analysed with confocal microscopy with reflected light so that the light only went though the glass bottom and no PDMS was in the light path, it seems unlikely that any lensing

effect was the cause for these changes. Moreover, a lensing effect cause can be discarded by the time dependence of the fluorescence changes, and by the fact that when no iron was present no such effect was observed.

The option of an increase in fluorescent material does not seem probable as the amount of calcein or other fluorescent material should not increase, neither the quencher concentration should decrease. Moreover, PDMS by itself is not fluorescent and should therefore not provide any significant additional fluorescence.

Oxygen is a well known fluorescence quencher [122, 123]. The oxygen removal from the microwell would decrease the fluorescence collisional quenching and would result in a visible fluorescence increase; yet, by comparing this to the differences in fluorescence obtained in oxic and anoxic conditions, it can be seen that the fluorescence increase is far below the range of the one seen in the microwells (data not shown). Moreover, despite the fact that the water in the control layer is pressurised with nitrogen, the time the gas would take by simple diffusion to reach the microwells would be far above the time in which the observation were made. Therefore, a substitution of oxygen for nitrogen in the microwell does not seem either a reason for the fluorescence increase.

PDMS hydrophobic nature can result on the partitioning of several compounds from the aqueous solution into the polymer matrix [85, 124]. This means that components of the growth medium could partition in there; however, given their hydrophilicity, they should stay within the aqueous solution. Moreover, the only component that, upon partitioning into the PDMS, would yield a fluorescence increase as high as the one seen would be calcein. However, calcein does not permeate PDMS, and it would need to become dissociated from the complexed iron to become more fluorescent. Moreover if calcein partitioned into the PDMS, the fluorescence intensity in the microwell should decrease, which is not the observed case.

PDMS is known to be water vapour permeable [125], so that osmolarity changes can take place upon evaporation of the water in the microchannels [86]. This would hint towards the fact that swelling the microsystem previous to the measurements would reduce the fluorescence increase rate. However, upon evaporation, the proportion of different solutes should remain constant among them, so that proportion calcein-should not change. Moreover, water jackets have been previously used in microfluidic systems to prevent osmolarity changes [126], and are similar to the control layer used in this microsystem. Therefore, the control layer of the presented microsystem should act as a water jacket as well that prevents an osmolarity shift inside the microwell. For this, this option did not seem much plausible either.

Another point to be made is that Sylgard 184, the PDMS brand that was used throughout the experiments, is composed by a base and a curing agent that, when combined, polymerise the base monomers due to a platinum-based catalyser in the curing agent [127, 128]. There is a then a possibility that either the uncross linked monomers or the platinum leach into the microwell. Uncrosslinked PDMS monomers have a mass of 74.15 Da and are known to leach into microchannels [129, 130] and impact the normal cellular physiology [130, 131]. Whether the uncrosslinked PDMS monomers or the platinum leach into the microwells could affect the solution equilibrium affecting the final fluorescence intensity is not known, though.

7.5.4. Microsystem coating

As explained before, the microsystem was coated with phospholipids in order to check whether they had any impact on fluorescence changes, and the microsystem was as well swelled with water. Importantly, whereas the coating did not buffer enough the fluorescence changes, swelling the microsystem had a substantial impact on the fluorescence variation over time by slowing down the increase in fluorescence and making it more sustained over time. This could point towards water vapour evaporation in the microwell, which would be in line with the fact that the bacteria do not seem to survive over time in the microwells (survival assessed by motility). It should be also noted that in other bacteria, such as *E. coli*, such shifts might not have had such a big impact on the cells. However, as stated before, as the valves from the control layer is should preclude any evaporation and, therefore, osmolarity shifts.

When coating with lipids, it was seen an uneven coating, even though it should be noted that the whole system was actually coated (observed as a fluorescent signal) but at different intensities. The lipids were seen to be compatible with bacteria viability. However, despite thorough flushing of the microsystem with fresh medium, it was not possible to completely remove the lipid vesicles from the microsystem. This of course makes the assessing of fluorescence intensity more complicated, as different amounts of vesicles inside the microwell will result in differential amounts of total iron, despite having an equal initial concentration, as the resulting volume fo the microwell will be lower. Moreover, the lipid coating did not prevent fluorescent changes. Furthermore, it was observed that a mud-crack-like pattern (seen as by a loss of fluorescence) arose at the rim of the actuated microwells, and that this rim increased its area over time. It was observed as well from the lipid coating images that some non-fluorescent grooves were present in the actuated valves. Chances are that these grooves emerge from the SU-8 master mould itself, as eventually SU-8 can have cracks on its surface that, depending on the application, can have a major impact on the applications downstream. These cracks arise mainly from stresses and may be transferred then to the PDMS surface which, upon tension, could start tearing. It has been indeed reported previously the presence of cracks on PDMS surfaces (upon intense plasma activation, as well) [132, 133], with consequent salt deposition on them, which could affect the concentration of the environment due to impurities present in the PDMS [132]. The presence of such cracks might have an influence in the fluorescence intensity shifts observed during the measurements, even though it could not be determined.

7.6. Conclusion and outlook

In the present chapter, the microwell platform presented in *Chapter 6* was intended to be used for iron uptake fluorescent assays at the single-cell scale to monitor the outer chemical microenvironment of the bacterium and study its iron uptake kinetics. The platform had previously proven to be convenient for the study of the interplay between the magnetic field, the bacterial swimming speed and wall curvature, as it allowed to confine single bacterial cells in very defined volumes and perform short term measurements. However, when implementing it to study the chemical microenvironment rather than the physical one, the microsystem failed to provide an understandable platform for the fluorescence study of iron uptake rates. As the cause could not be determined, the present system was abandoned for such purpose and an alternative platform based on lipid vesicles was adopted, as presented in the following and last chapter.

8. Visualising the outer chemical microenvironment: confinement of single-cells in lipid vesicles

The present chapter deals with the use of giant unilamellar vesicles (GUVs) as an alternative platform to the PDMS-based microwells presented in the previous chapter to trap single MSR-1 cells to study their iron uptake kinetics via a fluorescent assay.

8.1. Introduction

As exposed in the previous chapter, individual *M. gryphiswaldense* cells can be isolated in confined compartments in the pL range (3 to 50 pL) based of PDMS-glass microwells. However, if a fluorescent-based assay for the iron uptake determination was to be performed, such platform did not seem appropriate. For this reason, in the present chapter GUVs (i.e. unilamellar lipid vesicles with diameters >1 μm) are used as an alternative system in which to encapsulate single bacteria and determine their iron uptake rates.

Lipid vesicles have become very useful and versatile tools for many different purposes, such drug encapsulation [134], gene transfection [135], and membrane structureal studies [136]. Lately, an increasing trend has emerged which uses GUVs as a means to create very controlled and simple cell-like systems as a means of facilitating a bottom-up approach to the construction of artificial cells [137]. The two most important characteristics that make GUVs appealing for such objective are their assembly out of natural constituents, lipids, which provide a physicochemical barrier which leads to the second important characteristic: the ability to compartmentalise chemical reactions. These two features make GUVs a plausible alternative to substitute microwells for the intended measurements.

GUVs had not been used as a means of encapsulating bacteria until very recently, as observed by the fact that only four publications addressing this strategy have been reported until now [138-141]. The present chapter, thus, provides new insight on the questions that can be addressed when applying this platform.

8.2. Objectives

The objective of this chapter is to establish a GUV-based platform for magnetotactic bacteria encapsulation to determine the iron uptake kinetics of *M. gryphiswaldense* bacteria at the single-cell scale, thus overcoming the pitfalls encountered in the platform encountered in the previous chapter.

8.3. Materials and methods

8.3.1. Materials

Chloroform, mineral oil, PBS, and the densifying agents sucrose, glucose, polyvinyl alcohol (PVA) (M_w=145 kDa) and polyethylene glycol (PEG) (M_w=8 kDa) were purchased from Sigma–Aldrich (Germany). The lipids 1-palmitoyl-2-oleoyl-sn-glycero-3-phosphocholine (POPC) to create the GUVs, biotinylated-phosphatidylethanolamine (biotinylated-PE) to immobilise the GUVs, and 1,1'-dioctadecyl-3,3,3',3'-tetramethylindodicarbocyanine (DiD) to label the GUVs were purchased from Avanti Lipids Polar Inc. (Alabaster, AL). Streptavidin and bovine serum albumin conjugated with long chain biotin (biotinylated-BSA) for GUV immobilisation were purchased from Calbiochem (Germany) and Thermo Scientific (USA), respectively. The 96-well microtiter plates with glass bottom, where the assays were performed, were purchased from Corning (Germany). *Magnetospirillum gryphiswaldense* MSR-1 cultures, growth medium components and calcein were obtained as detailed in the *General materials and methods* section.

8.3.2. Lipid stocks preparation

POPC, biotinylated-PE and DiD lipid mixture stocks were dissolved in chloroform to a final lipid concentration of 8 mM with a molar relation of 98.7:1.2:0.1 POPC:biotinylated-PE:DiD. The stocks were stored in glass vials with rubber stoppers and spacers or a screw-tap at -20 °C until their use. For its use, 75 µL of the lipid mixture were dried under a N_2 flow, and were desiccated under vacuum during 1 h. Subsequently, 1.5 mL of mineral oil were added to the vial, and the solution was then sonicated during 45 min to dissolve the lipids. After the sonication, the vials were shortly vortexed, and were incubated overnight in a dark place at room temperature. After the incubation, the ready-to-use lipid oil stocks were stored at 4 °C until further use.

8.3.3. Inner and outer solution preparation

The exact compositions of the different inner and outer solutions are indicated in the *General materials and methods* section. In any case, it should be noted that all the solutions used were filter-sterilised through a pore diameter of 0.200 µm to remove any microorganism, and N_2-bubbled previous to their use to create an anoxic solution. The composition of the standard inner and outer solution mainly used in the experiments is however specified as follows.

The outer solution composition is specified in Table 1; it is comparable to the one of the standard MSR-1 growth medium, but without the soya peptone, yeast extract nor trace metals, and by exchanging the iron source from Fe(III)-citrate to $FeCl_3$, keeping the same concentration. The inner solution composition is specified in Table 1; this solution is analogous to the outer solution, but presents calcein and PVA as additional components. It is worth noting that PVA was added as a powder to the already N_2-bubbled and filtered growth medium solution, and that the solution containing PVA was not further filtered to ensure that no PVA was lost during the filtration process. If bacteria were added to the inner solution, a culture of generally iron-depleted bacteria (two passes in no iron medium) was centrifuged at 5,000 RCF during 10 min at 4 °C, the supernatant was discarded and the pellet was resuspended into the inner solution up to the bacterial concentration required. Once the bacteria had been resuspended, the rest of the procedure was carried immediately to avoid any data acquisition delay and

decrease as much as possible the gap between resuspending the iron-depleted bacteria into iron-rich medium and the initiation of the measurements. The time delay between both could be cut down to 10 min.

8.3.4. GUV production and bacterial encapsulation

The GUV production and bacterial encapsulation was performed via the phase transfer method [142] (Figure 30A). All the steps, unless otherwise stated, were carried under anaerobic conditions in an atmosbag as magnetotactic bacteria require low oxygen tensions for the synthesis of magnetosomes. For GUV immobilisation (Figure 30B), 20 µL biotinylated-BSA (1 $mg \cdot mL^{-1}$, PBS, 1x, pH 7.5) were placed in a microwell of the 96-well plate, were incubated at room temperature during 30 min, and were subsequently rinsed three times with PBS (1x, pH 7.5). If biotinylated-BSA had been used, 20 µL of streptavidin (50 $\mu g \cdot mL^{-1}$, PBS, 1x, pH 7.5) were added to the well and were incubated during 30 min at room temperature; subsequent to this, the well was rinsed again three times with outer solution (the whole step was not performed if BSA had been used). If no GUV immobilisation was necessary, BSA was used instead of biotinylated-BSA and the streptavidin step was omitted. After this, 50 µL of N_2-bubbled outer solution were added into the well, and 20 µL of lipid oil stocks were careful placed on top of the outer solution. The well was then incubated during 30 min to allow for the formation of a phospholipid monolayer at the oil-water interface. After this, 100 µL of lipid oil stock were placed into an Eppendorf tube, and 2 µL of outer solution were added to the solution. It can be seen that the drop of outer solution precipitates to the bottom of the tube staying biphasic. Then, the Eppendorf was 3 times rasped onto the hole-bearing part of an Eppendorf rack, which yielded an emulsion of water-in-oil droplets. 50 µL of the emulsion were carefully placed on top of the solution in the well so that the phospholipid monolayer does not get disturbed. Directly after this, the borders of the microwell were greased with petroleum jelly and a glass coverslip was placed on top

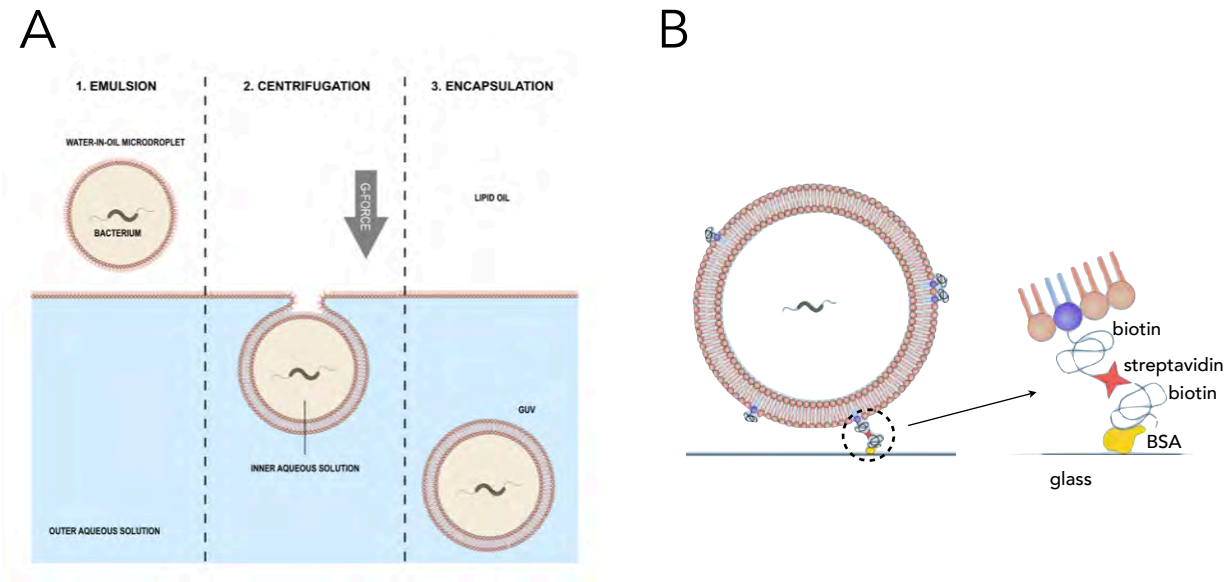

Figure 30. Phase transfer method to encapsulate bacterial cells and immobilise the GUVs. (A) Sketch showing the phase transfer method. A water-in-oil emulsion is prepared with the water containing bacteria (1). By centrifugation the microdroplets are forced go through a phospholipid monolayer (2), resulting in the formation of lipid vesicles having as inner solution the water solution with the bacterium (3). (B) Sketch showing the immobilisation of a GUV onto a glass surface through biotinylated-PE (PE in purple, and biotin as a black thread), streptavidin (pink) and biotinylated-BSA (BSA in yellow, and biotin as a black thread).

of the microwell to seal it and prevent O_2 to diffuse into the well. With no further delay the 96-well plate was centrifuged at 600 RCF during 3 min at 20 °C to force the microdroplets through the phospholipid monolayer through the phase transfer method [142] (Figure 30) (this last step was not carried in the atmosbag).

8.3.5. GUV imaging

GUVs imaging parameters are specified in the *General materials and methods* section. Overall, they were imaged with a 488 nm laser for calcein fluorescence, and a 638 nm laser for DiD visualisation. A digital zoom of 2.00 was applied to record the images of the GUVs.

8.4. Results

8.4.1. GUV production

GUV production with PVA 1 % (w/v) yielded the highest proportion of vesicles within 7-20 µm in diameter (Figure 31), which accounts for resulting iron mass availabilities ranging from roughly 0.2-12 fg. Consequently, given the iron availability sizes between 10 and 15 µm would be the most adequate to detect fluorescence changes, 5 µm probably not having enough iron (Figure 31).

A

GUV dimensions		[$FeCl_3$] = 50 µM
Diameter (µm)	Volume (pL)	Iron mass (fg)
5	0.07	0.18
10	0.52	1.46
15	1.77	4.93
20	4.19	11.7
25	8.18	22.85

B

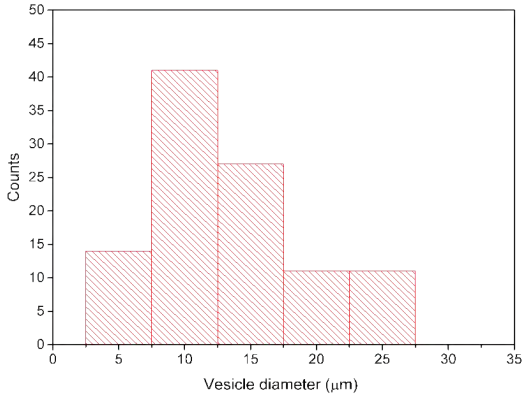

Figure 31. Iron availability in GUVs and GUV size distribution. (A) Amount of available iron for different GUV dimensions for an iron concentration of 50 µM. (B) Size distribution of the GUVs produced with PVA 1 % (w/v).

8.4.2. Encapsulation of calcein in GUVs

A calibration curve for calcein and iron analogous to the one performed in the microwells in the previous chapter (Figure 27) was also performed inside the GUVs (Figure 32). Again, the calibration curve yielded a linear relationship, but notably, compared to the calibration curves performed in the fluorometer (bulk) and in the microwells (small volumes), the calibration curve gave a higher dispersion for each fluorescent value, as seen by the error bars (which were barely present in the other two curves), which grew bigger with lower concentrations of iron (Figure 32A). In any case, no correlation between the fluorescence intensity and the GUV size was observed,

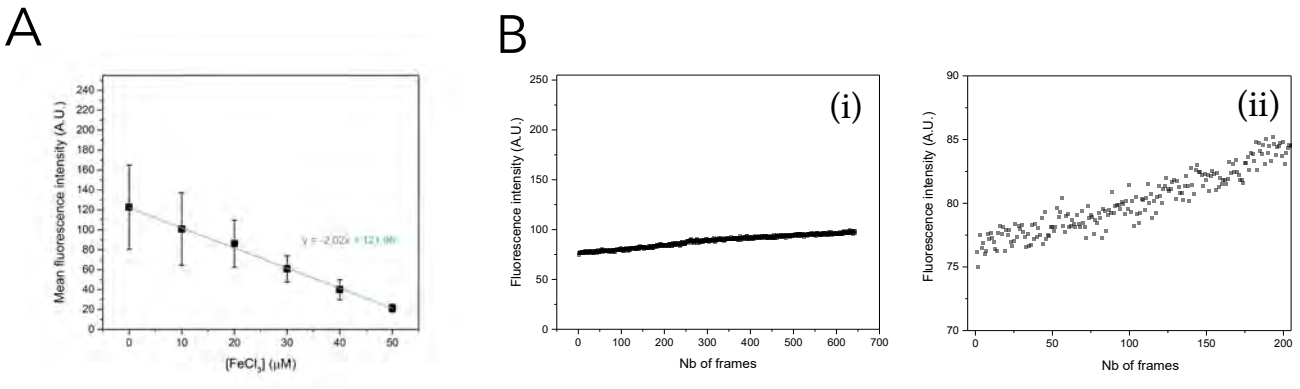

Figure 32. Calibration curve for iron and calcein inside the GUVs. (A) Calibration curve for different concentrations of $FeCl_3$ against 25 μM calcein. (B) Fluorescence increase inside a GUV bearing upon sustained irradiation of a GUV at λ_{em}= 488 nm. In (i), the fluorescence increase is shown over the full dynamic range of the microscope (represented by the 0-255 scale of arbitrary units) for 650 frames, whereas (ii) shows the fluorescence increase in only the first 200 frames within a defined part of the microscope dynamic range (70-90 A.U.).

indicating that size did not interfere with the fluorescence readout. When performing a photobleaching study to determine how many times the GUV could be irradiated before losing fluorescence intensity, it was observed that the GUV intensity increase with an increasing number of irradiations (Figure32B).

8.4.3. Inner solution impact on *M. gryphiswaldense*

As the GUVs' inner solution needs to have a densifying agent to allow the microdroplets through the phospholipid bilayer, three different densifying agents were tested: sucrose (a disaccharide, and the most commonly used agent for GUV production) [136], and the polymers PVA and PEG (Figure 33A). From these, the disaccharide sucrose had the most detrimental impact on bacterial growth, with concentrations over 250 mM abolishing bacterial growth. PVA decreased bacterial growth with increasing concentrations without fully inhibiting bacterial growth; and PEG yielded comparable growth yields to the control, even though for the lowest concentration of PEG, a slighter higher growth yield was even observed. Despite the fact that PEG did not compromise bacterial growth, PVA was selected as densifying agent of choice at 1 % (w/v) due to the higher yield of GUVs produced with it in comparison to PEG . Parallel to this, the densifying agents were studied as well as carbon sources to determine whether *M. gryphiswaldense* could uptake them and therefore change the osmolarity of the medium during growth (Figure 33B). The different carbon sources assayed were sucrose, glucose, PVA and PEG as agents used for densifying the medium; pyruvate as the standard carbon source; citrate as the standard iron complexing agent in standard MSR-1 growth medium; and a negative control with no carbon source. From all the assayed sources, the only source that promoted bacterial growth was pyruvate, whereas all the rest yielded levels comparable to the negative control with no carbon source. From such results, it can be concluded that *M. gryphiswaldense* does not have the ability to support its carbon requirements with any of the densifying agents.

Despite growth being an important parameter to assess bacterial fitness, the aim of the present project was to determine the iron uptake of the bacteria. Consequently, the impact of the selected inner solution of the

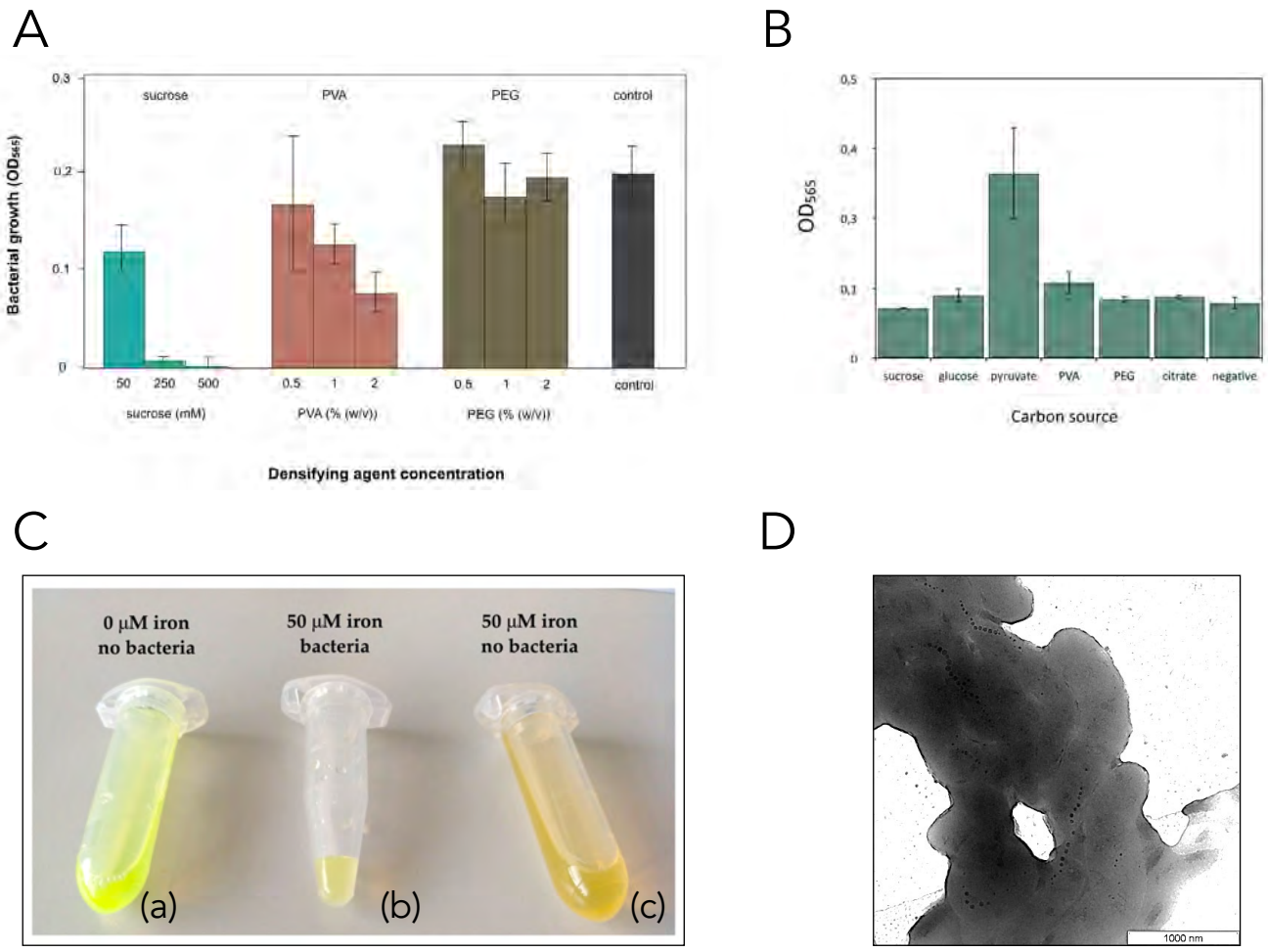

Figure 33. Bulk culture of *M. gryphiswaldense* in different conditions. (A) Bulk 10 mL cultures with different concentrations of densifying agents after 24 h at room temperature and no shaking. The control had no densifying agent. (B) Bulk 10 mL cultures with the different standard *M. gryphiswaldense* carbon sources and the densifying agents as a carbon source after 24 h at from temperature and no shaking. The control had no carbon source (negative control). (C) Bulk cultures in Eppendorf tubes after 3 days of incubation at room temperature and no shaking. Tube (a) was filled with growth medium, 1 % (w/v) PVA, 25 µM calcein, but no iron source. Tube (c) was filled with growth medium, 1 % (w/v) PVA, 25 µM calcein and 50 µM $FeCl_3$. Tube (b) was filled with the same solution as tube (c), but bacteria were added to it to an OD_{565} of 0.3. (D) TEM image from the tube (b).

GUVs (growth medium supplemented with 25 µM calcein, 50 µM $FeCl_3$, and 1 % (w/v) PVA) in a bulk culture was as well examined (Figure 33C,D). *M. gryphiswaldense* was resuspended in inner solution and incubated for 3 days. Along with it, two controls (one with iron and one without iron) with no bacteria were as well incubated; one showing an orange colour arising from the complexing of iron by calcein, whereas the other showing the calcein yellow colour as no iron was present. Initially, the tube with bacteria presented an analogous colour to the control tube with 50 µM iron. However, after 3 days, it could be observed how the orange colour had diminished and had veered towards a more yellowish colour, which generally indicates a lower concentration of iron in solution (Figure 33C). Accordingly, the TEM images arising from the culture showed that bacteria were able to produce magnetosomes despite the fact that they were in the inner solution bearing PVA. Consequently, as magnetosome synthesis was taking place, such inner solution was subsequently used for the posterior measurements.

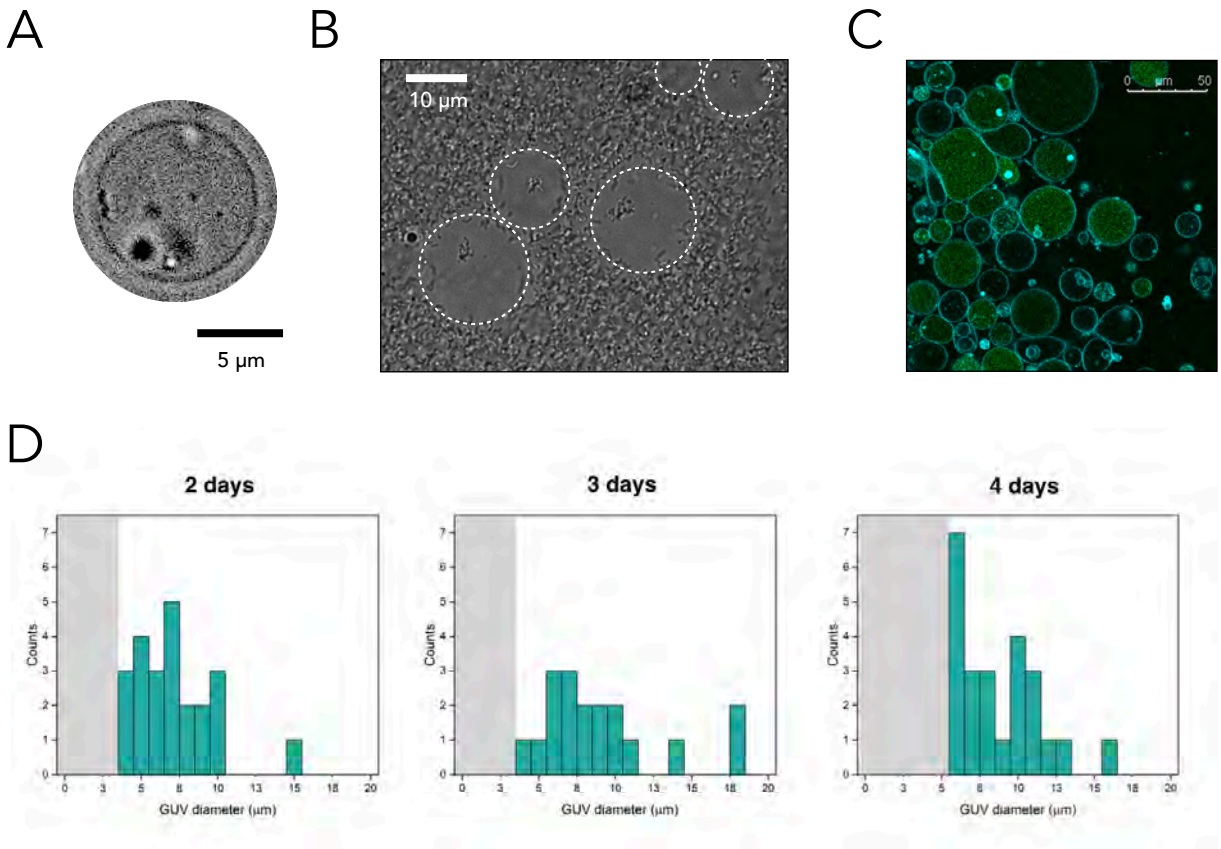

Figure 34. *M. gryphiswaldense* encapsulation in GUVs. (A) Single bacterial cell encapsulated inside a GUV. (B) Transmission image of GUVs (dashed circles) incubated over 4 days. It is observed that outside the GUVs microorganisms have grown filling all the field of view. (C) Fluorescent image of GUVs to whose outer solution ampicillin 100 µL·mL^{-1} had been added. (D) Histograms showing a population of GUVs of different sizes with motile encapsulated bacteria over the course of several days. The counts indicate the amount of GUVs for a certain size inside which motile bacteria were observed. The grey area indicates the region of GUV sizes in which motile bacteria were no longer present.

8.4.4. Encapsulation of *M. gryphiswaldense* in GUVs

Bacteria were encapsulated inside the GUVs via the phase transfer method, with some GUVs hosting one single bacterium (Figure 34A). However, as observed in the same figure, as GUVs showed some debris, the assessment of non-motile bacteria could be complicated as they could be confused with debris. For that reason, measurements were only performed with bacteria clearly showing active motion. In any case, the GUVs showed to be stable over the course of days and provide a robust environment against external microorganisms, which could not penetrate the GUVs, which conserved their integrity (Figure 34B). Ampicillin was tested to kill the external microorganisms developing over long cultivations, but its addition deformed and fluidised the GUVs (Figure 34C), which was an unwanted feature. Consequently, no antibiotics were used for the measurements. Concerning the bacterial viability inside the vesicles, the bacteria remained viable (as assessed by their motility) over the course of several days (Figure 34D). As such time range is far above the intended experimental length (6-12 h), it can therefore be assumed that the bacterial viability will not be compromised by any lack of nutrients or waste product build-up during the course of the iron uptake measurements when GUVs with diameters bigger than 4 µm are studied.

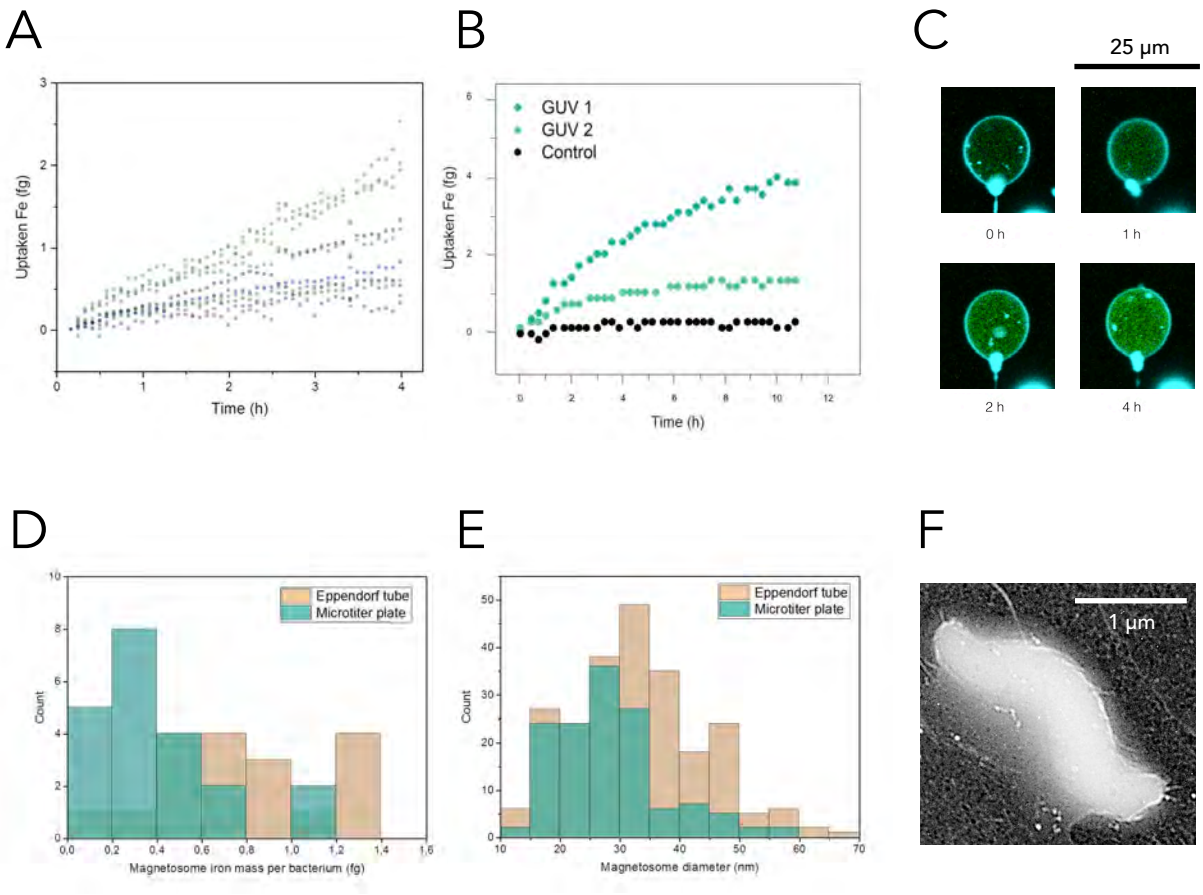

Figure 35. *M. gryphiswaldense* iron uptake in GUVs. (A) Iron uptake of several single bacteria over the course of 4 h. (B) Iron uptake for two different single bacteria (GUV1 and GUV2) over the course of 11 h. A negative control GUV with no bacterium is shown in black. (C) Fluorescent images of a GUVs with a single bacterium over time. (D) Comparison between the iron mass in the bacteria encapsulated in GUVs (microtiter plate, in green) and in bulk (Eppendorf tube, in pink) as measured by quantifying the magnetosomes from TEM images, as the one in (F). (E) Comparison between the magnetosome size in the bacteria encapsulated in GUVs and in bulk as measured by quantifying the magnetosomes from TEM images. (F) TEM image of a bacterium cultured in a GUV.

8.4.5. *M. gryphiswaldense* iron uptake rates in GUVs

As the calcein-iron assay for quantification purposes had been previously validated, it was used along with encapsulated bacteria to calculate their iron uptake rates based on the vesicle fluorescence intensity increase (Figure 35C). As it can be expected from cell heterogeneity, single bacterial cells exhibited different iron uptake rates (Figure 35A, Table 6) ranging from 0.08 to 0.63 fmol·cell^{-1}·h^{-1}, and uptaken iron masses ranging from 0.32 up to 2.53 fg after 4 h. The iron uptake traces for these first 4 h had a linear shape, in contrast to traces observed for longer time ranges, where a saturation of the iron uptake over time could observed as the traces reached a plateau (Figure 35B). The bacteria-devoid control GUV showed no fluorescence intensity increase, as expected, as the concentration of iron within the GUV should remain constant.

TEM comparisons between bacteria cultured in the GUVs, and bacteria cultured in the inner solution in bulk showed that bacteria cultured in bulk had a higher content of iron than the ones cultured in the GUVs (Figure

35D). Also, it should be pointed that the iron mass values calculated from TEM images magnetosome measurements (iron mass calculated by considering each magnetosome a sphere) yielded iron masses significantly lower than the yields obtained by the fluorescent assay, as TEM images gave iron masses shifted towards 0-0.4 fg Fe, whereas the calcein assay gives masses above 0.32 fg. In terms of magnetosome size, the bacteria cultured in GUVs have diameters shifted to smaller values compared to the bacteria cultured in bulk, which would be in accordance with bacteria bearing less iron due to magnetosomes being smaller. However, it should be noted though, as seen in Figure 35F, that, in the TEM images coming from GUV-encapsulated bacteria, magnetosomes did not appear as clear and with as much contrast as in the TEM images coming for standard cultures or from bulk culture in inner solution (Figure 33D).

Table 6. *M. gryphiswaldense* iron uptake rates in GUVs. Iron uptake rates and total iron uptaken calculated for the traces displayed in Figure 35A, and for the two bacterium traces showed in Figure 35B.

Iron uptake rate (Fe fmol · cell^{-1} · h^{-1})	0.63	0.51	0.48	0.33	0.30	0.21	0.15	0.15	0.13	0.08
Uptaken iron mass after 4 h (fg · cell^{-1})	2.53	2.02	1.94	1.33	1.22	0.82	0.60	0.41	0.53	0.32
Uptaken iron mass after 11 h (fg · cell^{-1})	4.00	1.48								

8.5. Discussion

8.5.1. GUV formation

The lipid vesicles used for this measurements were created via the phase transfer method and fall within the range of what is known as giant unilamellar lipid vesicles (GUVs), which defines lipid vesicles beyond 1 μm in diameter (the classification defines as well small and large unilamellar lipid vesicles, SUVs and LUVs, respectively, which fall within the range of 20-100 nm and 100-1,000 nm, respectively) [143]. For the encapsulation of microorganisms, it is therefore necessary to work with GUVs due to microorganism size restrictions for standard microorganisms, even though for the lower limit of life, it might be possible to work with LUVs as well. However, GUVs have another advantage compared to SUVs and LUVs, not only in terms of encapsulation of microorganisms, but also because GUVs can be observed under standard microscopes without resorting to very high magnifications (100x, for example). This implies that it is possible to visualise these objects in a simple way in order to determine the exact fluorescence inside each of them in a differential way. If using LUVs and, specially SUVs, techniques other than confocal microscopy need to be relied onto as direct observation will not be possible. One of these techniques would be fluorometry via a fluorometer, which tells the average fluorescence of the vesicles, but does not account/show intervesicle differences. In such a system it would not be possible to account for inter vesicle differences and it would not be possible to perform independent measurements as it is necessary in this case.

The method of choice to produce the lipid vesicles was the phase transfer method in which a water-in-oil emulsion of water microdroplet surrounded by phospholipids is forced to pass through a phospholipid monolayer [142]. There are, however, other methodologies to prepare GUVs, such as swelling [144], electroformation [145]

and microfluidic flow focusing [146, 147]. Bacteria encapsulation involves the handling of a living organism in order to study its physiology, accordingly, the method of use has to preserve as far as possible the physiology and native conditions of the organism. For that reason, swelling could not be use as it is slow and neither could electroformation, as electric pulses are known to induce pores in the bacterial membrane [148]. Microfluidic flow focusing is, however, a reasonable alternative as it preserves the natural environment of the microorganism. Moreover, microfluidic formation fo GUVs offers two main advantages over the present method: size monodispersity and high-throughput [147]. Nevertheless, when forming microfluidic-aided GUVs, special care should be taken when handling the GUVs, as they would need to be in microaerobic-anaerobic conditions for the proper forming of magnetosomes. Secondly, special attention has to be put as well on stability, as it was observed that the GUVs formed by this method were not stable over the needed course of time (data not shown). In any case, this method would help to get over the inherent polidispersity of the phase transfer method. Monodispersity would help in analysis purposes as the size analysis would be much simpler, and the high-throughput would allow to screen for far much more GUVs and more data could be acquired.

Another characteristic of the phase transfer method that could be overcome with microfluidics is the fact that the phase transfer GUVs are produced through a density gradient, meaning that some compounds (densifying agents) have to be added to the standard bacterial growth medium to force the microdroplets through the phospholipid monolayer. The addition of such compounds alters the original growth medium composition and they need to be tested to ensure that they do not impact the bacterial physiology.

Another main point is the osmolarity of the medium and the densifying agent added, as they will be directly related not only to the resulting GUV yield [149], but also to the bacterial survival. For low osmolarities, as the ones needed for *M.* gryphiswaldense growth (50-80 mOsmol·kg^{-1}), the GUV yield is much smaller than for osmolarities above 300 mOsmol·kg^{-1}. However, such high osmolarities compromised the viability of this bacterial species, most probably resulting from an osmotic shock to the bacterium, natural to freshwater. It should be pointed out, though, that other bacteria can dwell in environment with higher osmolarities without this compromising their physiology, as it is the case of *E. coli*, which is usually cultured in osmolarities ranging form 250-300 mOsmol·kg^{-1} [141, 150].

The anchoring of the GUVs onto a glass surface to allow the monitoring of specific GUVs over time was performed via a biotin-streptavidin coupling. For this, biotinylated-PE was added to the GUV composition, even though it should be noted that an excessive amount of PE could result in GUV leakages due to membrane destabilisation.

8.5.2. GUV visualisation

The calibration curve for calcein-iron showed an increased fluorescence variability with decreasing iron concentrations, compared to previous calibrations curves performed both in bulk and inside the microwells. Surprisingly, the fluorescence intensity distribution is notably different for different iron concentrations, decreasing with increasing iron concentrations. It should be noted as well that the GUV calibration curve is slightly different to the other calibration curves in terms of composition, as it also has the densifying agent, PVA. PVA has been previously reported to interact with iron [151], even though it has not been reported to interact with calcein. This along with a differential encapsulation as well for PVA amount might result in the observed variability.

Nevertheless, and importantly, all the measurements were started in iron-rich conditions to allow bacterial iron uptake, that is, all the measurements were started in the region of lowest variability, thus reducing the error.

The photobleaching study to determine the number of frames that could be recorded from the GUVs before damaging the fluorophore with an inherent decrease in fluorescence intensity. Surprisingly, the sustained irradiation of the GUVs bearing calcein and iron invariably resulted in a fluorescence increase over time, even though after some time the increase would stop and the trend would be reversed, showing an intensity decrease. Moreover, such intensity increase was observed to depend on the laser wavelength the sample was irradiated with, being more pronounced for more shorter wavelengths. This is of special importance as the iron uptake assay relies on measuring the fluorescence increase, and this light-triggered effect could generate false positives. However, the effect could be reduced simply by using lower laser powers (which is as well beneficial for the bacterium, as an intense illumination could damage it). Moreover, if GUVs are imaged every 20 min, this would mean that after 12 h, they would have been irradiated 36 times. For the used laser power, the irradiation-triggered fluorescence increase does not significantly increase below 50 irradiations. It can therefore be estimated that the imaging process will not generate false positive whereas staying below this number of irradiations. On the other hand, the fact that irradiation increased the fluorescence intensity in a power- and wavelength-dependent manner points towards a photochemical reaction. Most probably, iron photoreduction takes place, resulting in the decarboxylation of the chelating moieties which can no longer complex iron, as reported for other iron organic ligands [152-154], whereas keeping the fluorescent body.

8.5.3. Iron uptake rates

The iron uptake rate for *M. gryphiswaldense* has been repeatedly reported in literature [8, 17, 18, 91]. The v_{max} for the iron uptake rates are generally expressed as iron masses per unit time per mg of bacterial dry weight, but can be extrapolated to amount of iron per cell, as has been adapted in Table 7.

From the iron uptake kinetics extracted from the GUV imaging, it is observed that iron uptake is fairly constant over the first few hours. With longer times, though, a decrease in uptaken iron is observed, as would be expected when either the cell iron requirement has been satisfied so that the cell does not uptake more iron, or when the concentration of dissolved iron is too low to saturate the bacterial iron transporters, which has been reported to happen to concentrations below 10 μM [17]. The fluorescent readouts indicated that the iron concentration in the presented GUVs stayed always above 30 μM. Therefore, the slowing down of the iron uptake points towards a satisfied iron cellular requirement, rather than to the exhaustion of iron availability.

It is interesting to compare the iron uptake rates estimated in literature, where the reported average iron uptake rate oscillates between 0.38-0.76 $fg \cdot cell^{-1} \cdot h^{-1}$ for cells cultured at 28 and 30°C (Table 7). The values measured in the GUVs ranged between 0.08-0.63 $fg \cdot cell^{-1} \cdot h^{-1}$, being slower than the the reported ones. It has been reported, though, that temperature affects *M. gryphiswaldense* iron uptake by slowing it down to almost one fourth when decreasing the temperature from 28°C to 20°C [91]. The GUVs were incubated at 23°C, meaning that the bacterial physiology could have been slowed down and the iron uptake rate decreased compared to the iron uptake rates measured at 28 and 30°C. Moreover, the encapsulated bacteria had in their growth medium PVA as well. Consequently, the growth conditions in the GUVs might not be as optimal as in the other cases. Therefore, the highest iron uptake rates calculated within the GUVs are in the rate of the iron uptake rates

Table 7. *M. gryphiswaldense* iron uptake rates. The following table compares the different measured iron uptake rates for *M. gryphiswaldense* reported in several studies, as well as the conditions under which the measurements were performed (iron concentration, temperature, iron-starvation).

Iron uptake rate ($fg \cdot cell^{-1} \cdot h^{-1}$)	Parameters	Iron depleted cells	References
0.66	50 μM, 30 °C	Yes	[8]
0.76	50 μM, 28 °C	Yes	[18]
0.38	100 μM, 28 °C	No	[91]
0.10	100 μM, 20 °C	No	[91]
0.46	50 μM, 28 °C	Unclear	[17]
0.08 - 0.63	50 μM, 23 °C, GUVs, calcein, PVA	Yes	This thesis

calculated for the optimal temperatures, and it would be then plausible to consider that when incubating the GUVs at 28°C rather than at 23°C, the iron uptake would increase, even maybe double. Such assumption would indicate that with the present assay, there will be several iron uptake rates that will be higher than the ones calculated in bulk. This would be in line with the fact that, when measuring in bulk the mass of bacteria present, cellular debris and non-magnetic cells are as well measured, despite the fact that they do not compute to the total count of iron uptake [8], thus lowering the resulting iron uptake rate.

It is interesting as well to compare the total iron mass and magnetosome size based on the magnetosome TEM images from cells cultured in GUVs as well as from those cultured in inner solution in bulk. The magnetosome-derived iron masses are lower for GUV-grown bacteria than for the bulk one and, in both cases, lower than the calculated uptaken iron. The reason for this could be that either some artifacts do not allow the proper visualisation, and therefore quantification, of the magnetosomes in the images (as it is the case for the GUV images, where the lipid vesicles create a high background). Otherwise, it could as be ascribed as well to the presence of intracellular iron pools other than magnetosomes, where iron is coordinated to proteins, as it has been previously hypothesised [155-157]. This would as well be in line with the fact that the amount of iron inside a *M. magneticum* single-bacterium has been reported through ICP-MS to yield iron masses of 0.2-2 fg per cell, even though TEM images show iron contents of 0.35-1.2 fg, based on the magnetosome images [107].

Concerning magnetite synthesis, magnetite has been observed after 1 h of iron induction, reaching their mature size after roughly 6 h [18]. From there, it can be subtracted that after two hours, the magnetosome diameter is 19.4 nm, with 17.8 magnetosomes per cell; which would translate into an iron amount of 0.49 fg of iron; and after 3-4 h, the magnetosome diameter had become 26.3, with 20.3 magnetosomes per cell, which would translate into 1.38 fg of iron. These iron masses per cell are in line with the results presented here, indicating that the assay is comparable to what has been previously observed for iron-starved cells, and that this platform is a good means to achieve the iron uptake time and individual resolution that had not been achieved previously for these measurements. Overall, based on the total amount of iron internalised by the cell over time and the iron decrease over time, the results here presented do not seem compatible with reports of fully grown

magnetosomes 15 min after induction [90], but are in lines with previously estimated time ranges for full magnetosome formation of some hours [158].

8.6. Conclusion and outlook

In this final chapter, an alternative method to microfluidic systems for the isolation of single-bacterial cells was presented where to monitor *in vivo* iron uptake measurements. This platform was shown to sustain bacterial life over days and to be compatible with fluorescent iron uptake measurements. Importantly, it allowed to track specific GUVs containing single bacteria over time to quantify their iron uptake, having the advantage over other method of not only showing the individual bacteria heterogeneity, as compared to bulk measurements, but also of allow dynamic measurements in single cells without compromising bacterial viability, as compared to end-point destructive techniques. Remarkably, the obtained uptake rates by this method were in the same range as the ones that have been previously reported in bulk.

In the future, however, microfluidics could be coupled to the GUV production to obtain in a high-throughput manner monodisperse GUVs to facilitate even encapsulation and data treatment. For the moment, more data needs to be retrieved to have substantial statistics over MTB population and, in the future, it would be very interesting to differentially study ferrous and ferric iron uptake. Moreover, besides being applicable to other biomineralising organisms such as coccolithophores, the platform can be envisaged as means of screening for magnetosome overproducers, which could then be retrieved from the most fluorescent GUVs, for culture in bulk, transcriptomics and genomics, to determine the features that improve magnetosome production.

9. Conclusion and outlook

Throughout this thesis, different microfluidic systems have been developed with the purpose of capturing magnetotactic bacteria single-cell resolution and heterogeneity at different levels and within different microenvironments. The ground for this relied on the fact that MTB have been generally studied by traditional methods, which rely on bulk cultures. Analysis of a bulk culture is usually a synonym of analysis of millions of cells at a time, being considered as a single organism that can equally represent all of them. However, given the high mutation rates bacteria are generally subjected to as well as gene expression stochasticity, it is not complicated to imagine that individuals will present variations among them. In the specific case of MTB, this is effect becomes notorious in the spontaneous apparition of non-magnetic mutants, bacteria with twinned magnetosomes, axial bacteria, or non-swimming bacteria, despite the fact that MTB are typically described as swimming organisms with a preferred magnetic orientation, which have a chain of iron-containing monodisperse single domain crystals. Moreover, the microorganism microenvironment has a profound impact on the environmental cues the bacterium senses and which decide the fate of the bacterium. However, bulk methods do not exert a tight control over each individual cell's microenvironment, as cells are constantly subjected to chemical gradients as well to the presence of surfaces. Therefore, even if all the cells within a bulk culture were identical clones, their development would highly depend on the microenvironment they are exposed to. Consequently, a deeper understanding of MTB calls to address each bacterial cell separately and in a clearly defined environment, as the only way to achieve a high enough resolution of the cellular processes.

Two general aspects that have drawn much attention into MTB are their ability to swim orienting themselves with the magnetic field, as well as their biomineralization ability. For the first, not only the ecological implications for their capacity to interact with their environment to position themselves in the optimal location in the water column to increase to exploit the best redox parameters for magnetosome biosynthesis, but also they potential applications as magnetically actuable microswimmers that can be directed to specific locations. On the other hand, the second aspect represents a paradigm of biologically-encoded tight control over an inorganic phase giving rise in physiological conditions to very defined crystalline structures that are tremendously difficult to achieve with such perfection and under such conditions with standard wet chemistry. Moreover, it is the simplest living system where magnetic field sensing has been observed, and which could potentially be contrasted with the magnetoreception system of higher organisms. Also, understanding its fully synthetic pathways would not only allow to mimic them to create such structures in the lab for all the processes that have been envisaged already for them (such as hyperthermia, contrasting agents or cell separation) [159], but also to understand the factors that regulate and alter such structures, therefore having new ground to study whether some magnetite nanoparticles found in fossils and asteroids could have been biogenically produced and under which conditions, as well as to understand the extent to which MTB contribute to the iron biogeochemical cycle. These two aspects, swimming and biomineralization, are indeed the ones that have fuelled the development of the microfluidic platforms exposed in the thesis to give a higher control over the microenvironment as well as a higher resolution.

When studying MTB motility, it is true that bacteria are tracked and observed as separate elements. However, bacteria swimming nearby and, most importantly, open platforms, make the actual tracking of single

individuals over longer time scales difficult to achieve as the bacterial trajectories might mingle together and bacteria might swim out of the field of view. This also might make difficult the assessment of bacteria swimming in different modes and the time it takes for them to switch from one to another. To simplify this, though, microfluidics can be brought as a means of placing the bacteria in a more confined space, or totally confined, as for the microwells in *Chapter 5*, where single bacteria can be totally isolated and their trajectories assessed individually for each bacterium over long times without losing track of them.

On the other hand, when studying magnetite biomineralisation, it is indeed true that standard *in vivo* techniques do not allow to resolve different bacteria. Some other techniques, such as TEM imaging, do allow the visualisation and separation of individual bacteria; however, such techniques deal with dead cells which, moreover, come from bulk cultures so no previous tracking of the organism has been performed. This leaves room for questions that require a higher resolution than the one provided by standard techniques, as for example, the time it takes to produce a magnetosome chain. From bulk cultures, it is assumed that all the bacteria will uptake iron at the same pace starting from time zero, but then when observing TEM images, it will be seen that some bacteria will not bear any magnetosomes, and others that will have magnetosomes in different maturation states. This can be hypothesised to be due to bacteria unable to produce magnetosomes and to bacteria in different growth stages, respectively. The microenvironment could be playing a role, though. However, to prove any of such hypothesis and to understand whether there is actually any decoupling between the uptake of iron and the magnetite nucleation, a single-cell has to be analysed, as exposed in the three last chapters.

So, overall, the purpose of this thesis was to provide some microfluidic tools that allow to define the bacterial microenvironment and study the MTB as precisely as possible. *Chapter 4* started by introducing a simple PDMS-glass platform that mimicked the physical microenvironment of *M. gryphiswaldense*, the sediment grains, that is, the highly packed environment in which the bacteria dwell, thus providing a platform that resembles more the actual environment of the bacteria, as swimming assays have been traditionally performed in non-crowded environments, which did not resemble the natural environment of the bacteria. With it, it was possible to study how different magnetic fields affected bacterial navigation in such environment and how the bacterium magnetic moment is optimised to navigate at magnetic fields intensities similar to the Earth's magnetic field intensity. This platform, though, did not intend to target the single-cell level, but just to recreate a more ecologically significant physical microenvironment.

As the sediment-mimicking platform did not allow for studying the interaction of the bacteria with the sediment as grain boundaries were heterogeneous, but such parameter is of uttermost importance to actually predict the behaviour of the bacteria in such environments, in *Chapter 5* an alternative platform was introduced to target the bacterium-wall interaction with a clearly defined physical microenvironment, and uncoupled from any other bacterial interactions. The platform, PDMS-glass based, added an additional level of control to the microsystem by adding a second independent layer of microchannels that could be actuated giving rise to very defined volumes (microwells) where single bacteria were confined. The highly defined conditions of the platform enabled the study of the interplay of the wall curvature, the magnetic field intensity and the bacterial speed, and showed that bacteria trajectories could be predicted based on those three parameters.

Besides the physical microenvironment, the chemical one was as well of interest to study the biomineralisation process. *Chapter 6* addresses the need of reducing the time gap between bacterial culture and

sample analysis, by proposing a platform for X-ray studies where iron nucleation can be studied in single-cells. The microfluidic system, despite having a similar shape to the microchannels from *Chapter 5*, was for such purpose fabricated with PDMS-Si_3N_4. The microsystem allowed to immobilisation of MTB cells onto the microchannels that were kept alive until the moment of the measurement, and allowing to focus on single bacterial singles. This allowed to feed the bacteria with an iron-rich solution to allow them to form magnetosomes, and then perform the measurement in single independent bacteria, thus fully eliminating any time delay between the magnetosome nucleation and the signal acquisition.

The aforementioned microfluidic system was designed to study the inner chemical microenvironment of the bacterium. However, magnetite nucleation would not take place with a previous iron uptake process by the cell. On that account, it is as well of interest to determine the iron uptake rates and uptaken iron mass by single bacteria. *Chapter 7* addresses this question by making use of the platform presented in *Chapter 5* as a means to isolate single bacterial cells in defined volumes to fluorescently determine the dissolved iron concentration in the bacterial vicinity, that is, to monitor the outer chemical microenvironment. Unfortunately, the platform did not fulfil the requirements necessary to perform such assay, as the microsystem repeatedly altered the fluorescence readouts. Consequently, this platform could not be employed for such purpose.

Chapter 8 closes with the introduction of an alternative platform to measure the bacterial iron uptake kinetics: giant lipid vesicles (GUVs). In such case, instead of isolating the bacteria inside PDMS-glass microwells, the bacteria were encapsulated in phospholipid vesicles. The GUVs provided, as the microwells, reduced volumes in the picoliter range suitable for the fluorescent assay. This platform enabled to monitor the iron uptake rate and total uptaken iron with a single-cell resolution whereas preserving the sample integrity.

Hopefully, throughout this thesis it was possible to show how the volume miniaturisation provided by microfluidics allowed for a control of the microenvironment that would not otherwise be achieved. And most importantly, how by altering a few parameters of a simple microfluidic system, utterly different platforms can arise, with these allowing to divert the purposes and techniques the microsystems can be used for, and finally giving ground for *in vivo* studies as divergent as magnetically-actuated swimming, iron nucleation or iron uptake, but in any case, moving towards the single-cell scale.

As a final word, it would be possible as well to envisage the platforms that have been presented along the thesis as a battery of systems to analyse bacteria at different levels, as for example to study MTB performance for bioremediation purposes, such metal removal from soil. As an example, the platforms presented in *Chapters 4* and *5* could be used to analyse how MTB would navigate the sediment previous and after metal uptake, and how the metal uptake would affect their magnetic response. With this, it would be possible to study how different concentrations of metals affect bacterial navigation, which could be exploited as well to determine how contaminated environments might affect MTB. From a chemical perspective, the platforms presented in *Chapter 6* and *8* could be then used to determine the uptake rate of such metals as well as their nucleation, thus giving some information on the time the bacteria would take to remove these metals and the amount they would be able to cope with, with its subsequent impact on bacterial motility. As stated, there is still plenty of room to adapt these microfluidic systems to assess plenty of open questions with the possibility to tackle them dow to the single-cell resolution.

Bibliography

1. Lowenstam, H.A., Minerals formed by organisms. Science, 1981. **211**(4487): p. 1126-31.

2. Faivre, D. and T.U. Godec, From bacteria to mollusks: the principles underlying the biomineralization of iron oxide materials. Angew Chem Int Ed Engl, 2015. **54**(16): p. 4728-47.

3. Navrotsky, A., Energetic clues to pathways to biomineralization: precursors, clusters, and nanoparticles. Proc Natl Acad Sci U S A, 2004. **101**(33): p. 12096-101.

4. Bellini, S., Su di un particolare comportamento di batteri d'acqua dolce. Istituto di Microbiologia dell'Università di Pavia, 1963.

5. Blakemore, R., Magnetotactic bacteria. Science, 1975. **190**(4212): p. 377-9.

6. Blakemore, R.P., *Magnetotactic bacteria.* Annu Rev Microbiol, 1982. **36**: p. 217-38.

7. Bazylinski, D.A., et al., Fe3O4 and FeS4 in a bacterium. Nature, 1993. **366**: p. 218.

8. Schubbe, S., et al., Characterization of a spontaneous nonmagnetic mutant of Magnetospirillum gryphiswaldense reveals a large deletion comprising a putative magnetosome island. J Bacteriol, 2003. **185**(19): p. 5779-90.

9. Ullrich, S., et al., A hypervariable 130-kilobase genomic region of Magnetospirillum gryphiswaldense comprises a magnetosome island which undergoes frequent rearrangements during stationary growth. J Bacteriol, 2005. **187**(21): p. 7176-84.

10. Lin, W., et al., Genomic expansion of magnetotactic bacteria reveals an early common origin of magnetotaxis with lineage-specific evolution. ISME J, 2018. **12**(6): p. 1508-1519.

11. Schuler, D., Genetics and cell biology of magnetosome formation in magnetotactic bacteria. FEMS Microbiol Rev, 2008. **32**(4): p. 654-72.

12. Frankel, R.B. and R.P. Blakemore, Magnetite and magnetotaxis in microorganisms. Bioelectromagnetics, 1989. **10**(3): p. 223-37.

13. Jogler, C. and D. Schuler, Genomics, genetics, and cell biology of magnetosome formation. Annu Rev Microbiol, 2009. **63**: p. 501-21.

14. Wolfe, A.M.S.a.R.S., Chemotactic, magnetotactic and tactile behaviour in a magnetic spirillum. FEMS Microbiology Letters, 1984. **22**: p. 171-177.

15. Bennet, M., et al., Influence of Magnetic Fields on Magneto-Aerotaxis. PLoS One, 2014. **9**(7).

16. Lefevre, C.T., et al., Diversity of magneto-aerotactic behaviors and oxygen sensing mechanisms in cultured magnetotactic bacteria. Biophys J, 2014. **107**(2): p. 527-538.

17. Schüler, D. and E. Bauerlein, Iron-limited growth and kinetics of iron uptake in Magnetospirillum gryphiswaldense. Arch Microbiol, 1996. **166**: p. 301-307.

18. Faivre, D., et al., Environmental parameters affect the physical properties of fast-growing magnetosome. Amer Mineral, 2008. **93**: p. 463-469.

19. Rosenfeldt, S., et al., Probing the nanostructure and arrangement of bacterial magnetosomes by small-angle x-ray scattering. Appl Environ Microbiol, 2019.

20. Gravesen, P., J. Branebjerg, and O.S. Jensen, *Microfluidics - a review.* J Micromech Microeng, 1993. **3**: p. 162-182.

21. Manz, A., N. Graber, and H.M. Widmer, Miniaturized Total Chemical Analysis Systems: a Novel Concept for Chemical Sensing. Sens Actuators, 1990. **B1**: p. 244-248.

22. Manz, A., et al., Design of an Open-tubular Column Liquid Cbromatograpb Using Silicon Chip Technology. Sens Actuators, 1990. **B1**: p. 249-255.

23. Van De Pol, F.C.M. and J. Branebjerg, *Micro Liquid-Handling Devices - A Review*, in *Micro System Technologies 90*. 1990, Springer: Heidelberg. p. 799-805.

24. Lüdi, H., et al., Flow injection analysis and in-line biosensors for bioprocess control: a comparison. J Biotechnol, 1992. **25**(1-2): p. 75-80.

25. Manz, A., et al., Planar chips technology for miniaturization and integration of separation techniques into monitoring systems: Capillary electrophoresis on a chip. J Chromatogr A, 1992. **593**(1-2): p. 253-258.

26. Holmes, D. and S. Gawad, The Application of Microfluidics in Biology, in Microengineering in Biotechnology. Methods in Molecular Biology (Methods and Protocols), M. Hughes and K. Hoettges, Editors. 2009, Humana Press: Totowa, NJ.

27. Abou-Hassan, A., O. Sandre, and V. Cabuil, *Microfluidics in inorganic chemistry.* Angew Chem Int Ed Engl, 2010. **49**(36): p. 6268-86.

28. Tabeling, P., Recent progress in the physics of microfluidics and related biotechnological applications. Curr Opin Biotechnol, 2014. **25**: p. 129-34.

29. Liu, Z., N. Banaei, and K. Ren, Microfluidics for Combating Antimicrobial Resistance. Trends Biotechnol, 2017. **35**(12): p. 1129-1139.

30. Lee, S., L.J. Wu, and J. Errington, Microfluidic time-lapse analysis and reevaluation of the Bacillus subtilis cell cycle. Microbiologyopen, 2019. **8**(10): p. e876.

31. Li, J. and F. Lin, Microfluidic devices for studying chemotaxis and electrotaxis. Trends Cell Biol, 2011. **21**(8): p. 489-97.

32. Wang, L. and P.C. Li, Microfluidic DNA microarray analysis: a review. Anal Chim Acta, 2011. **687**(1): p. 12-27.

33. Li, L. and R.F. Ismagilov, Protein crystallization using microfluidic technologies based on valves, droplets, and SlipChip. Annu Rev Biophys, 2010. **39**: p. 139-58.

34. Huang, C.J., et al., Integrated microfluidic systems for automatic glucose sensing and insulin injection. Sens Actuators B Chem, 2007. **122**(2): p. 461-468.

35. Franssila, S., et al., *Chapter 27 - Microfluidics and BioMEMS in Silicon*, in *Handbook of Silicon Based MEMS Materials and Technologies*. 2015, William Andrew Applied Science Publishers. p. 565-581.

36. Burshtein, N., et al., 3D-printed glass microfluidics for fluid dynamics and rheology. Curr Opin Coll Interf Sci, 2019. **43**: p. 1-14.

37. Matellan, C. and A.E. Del Rio Hernandez, Cost-effective rapid prototyping and assembly of poly(methyl methacrylate) microfluidic devices. Sci Rep, 2018. **8**(1): p. 6971.

38. Narayan, S., et al., Low-pressure bonding of monolithic SU-8 microfluidic devices. J Micromech Microeng, 2018. **28**(12).

39. Goy, C.B., R.E. Chaile, and R.E. Madrid, Microfluidics and hydrogel: A powerful combination. Reactive and Functional Polymers, 2019.

40. Akyazi, T., L. Basabe-Desmonts, and F. Benito-Lopez, Review on microfluidic paper-based analytical devices towards commercialisation. Anal Chim Acta, 2018. **1001**: p. 1-17.

41. Convery, N. and N. Gadegaard, *30 years of microfluidics*. Micro and Nano Engineering, 2019. **2**: p. 76-91.

42. Schüler, D., R. Uhl, and E. Bäuerlein, A simple light scattering method to assay magnetism in Magnetospirillum gryphiswaldense. FEMS Microbiol Lett, 1995. **132**(1-2): p. 139-145.

43. Widdel, F. and F. Bak, *Gram-Negative Mesophilic Sulfate-Reducing Bacteria*, in *The Prokaryotes*, A. Balows, et al., Editors. 1992, Springer: New Yprk, NY.

44. Willey, J., L. Sherwood, and C.J. Woolverton, *Prescott's Microbiology*. 10th ed. 2017: McGraw Hill.

45. Frankel, R.B., et al., Magnetotactic bacteria at the geomagnetic equator. Science, 1981. **212**(4500): p. 1269-70.

46. Li, W., et al., A Magnetospirillum strain WM-1 from a freshwater sediment with intracellular magnetosomes. World J Microbiol Biotechnol, 2007. **23**(10): p. 1489-1492.

47. Lefevre, C.T., et al., A cultured greigite-producing magnetotactic bacterium in a novel group of sulfate-reducing bacteria. Science, 2011. **334**(6063): p. 1720-3.

48. Koziaeva, V.V., et al., Magnetospirillum kuznetsovii sp. nov., a novel magnetotactic bacterium isolated from a lake in the Moscow region. Int J Syst Evol Microbiol, 2019. **69**(7): p. 1953-1959.

49. Nakagawa, T., et al., Eelgrass Sediment Microbiome as a Nitrous Oxide Sink in Brackish Lake Akkeshi, Japan. Microbes Environ, 2019. **34**(1): p. 13-22.

50. Bazylinski, D.A. and C.T. Lefèvre, Magnetotactic Bacteria from Extreme Environments. Life (Basel), 2013. **3**(2): p. 295-307.

51. Martins, J.L., et al., Salinity dependence of the distribution of multicellular magnetotactic prokaryotes in a hypersaline lagoon. Int Microbiol, 2009. **12**: p. 193-201.

52. Petermann, H. and U. Bleil, Detection of live magnetotactic bacteria in South Atlantic deep-sea sediments. Earth and Planetary Science Letters, 1993. **117**(1-2): p. 223-228.

53. Lefevre, C.T., et al., Characterization of bacterial magnetotactic behaviors by using a magnetospectrophotometry assay. Appl Environ Microbiol, 2009. **75**(12): p. 3835-41.

54. Mao, X., et al., Magneto-chemotaxis in sediment: first insights. PLoS One, 2014. **9**(7): p. e102810.

55. Popp, F., J.P. Armitage, and D. Schuler, Polarity of bacterial magnetotaxis is controlled by aerotaxis through a common sensory pathway. Nat Commun, 2014. **5**: p. 5398.

56. Codutti, A., Behaviour of magnetic microswimmers: Simulations for natural swimmers and synthetic propellers, in Biomaterials. 2019, Potsdam Universität: Potsdam (Germany). p. 154.

57. Merkel, T.C., et al., Gas sorption, diffusion, and permeation in poly(dimethylsiloxane). Journal of Polymer Science Part B: Polymer Physics, 1999. **38**(3): p. 415-434.

58. Wentworth, C.K., A Scale of Grade and Class Terms for Clastic Sediments. The Journal of Geology, 1922.

59. Krummel, A.T., et al., Visualizing Multiphase Flow and Trapped Fluid Configurationsin a Model Three-Dimensional Porous Medium. American Institute of Chemical Engineers, 2013. **59**(3).

60. Tuson, H.H. and D.B. Weibel, *Bacteria-surface interactions.* Soft Matter, 2013. **9**(18): p. 4368-4380.

61. Johnston, I.D., et al., Mechanical characterization of bulk Sylgard 184 for microfluidics and microengineering. J Micromech Microeng, 2014. **24**(3).

62. Liu, M., et al., Thickness-dependent mechanical properties of polydimethylsiloxane membranes. J Micromech Microeng, 2009(19).

63. Ren, Y., et al., Emergent heterogeneous microenvironments in biofilms: substratum surface heterogeneity and bacterial adhesion force-sensing. FEMS Microbiol Rev, 2018. **42**(3): p. 259-272.

64. Donzel, C., et al., Hydrophilic Poly(dimethylsiloxane) Stamps for Microcontact Printing. Adv Mater, 2000. **13**(15).

65. Breisch, S., et al., Selective chemical surface modification of fluidic microsystems and characterization studies. J Micromech Microeng, 2004. **14**(4).

66. Madigan, M., et al., *Brock. Biology of Microorganisms*. 13th ed. 2012, San Francisco, CA: Pearson.

67. Matsunaga, T., et al., Complete genome sequence of the facultative anaerobic magnetotactic bacterium Magnetospirillum sp. strain AMB-1. DNA Res, 2005. **12**(3): p. 157-66.

68. Rexius-Hall, M.L., J. Rehman, and D.T. Eddington, A microfluidic oxygen gradient demonstrates differential activation of the hypoxia-regulated transcription factors HIF-1alpha and HIF-2alpha. Integr Biol (Camb), 2017. **9**(9): p. 742-750.

69. Fan, L.M., et al., Bacterioplankton community analysis in tilapia ponds by Illumina high-throughput sequencing. World J Microbiol Biotechnol, 2016. **32**(1): p. 10.

70. Finlay, C.C., et al., International Geomagnetic Reference Field: the eleventh generation. Geophysical Journal International, 2010. **183**(3): p. 1216-1230.

71. Faivre, D., et al., Development of cellular magnetic dipoles in magnetotactic bacteria. Biophys J, 2010. **99**(4): p. 1268-73.

72. Laboratory, D.P.N.N., Magnetic attraction for fish, crabs? Study examines whether magnetic fields from aquatic power sources affect animals, in ScienceDaily. 2010.

73. Popp, T., et al., Immediate responses of the cockroach Blaptica dubia after the exposure to sulfur mustard. Arch Toxicol, 2018. **92**(1): p. 337-346.

74. Hassan, H.A., et al., Influence of the magnetic field on the two-dimensional control of Magnetospirillum gryphiswaldense strain MSR-1, in IEEE/RSJ International Conference of Intelligent Robots and Systems (IROS). 2016.

75. Rismani Yazdi, S., et al., Migration of magnetotactic bacteria in porous media. Biomicrofluidics, 2018. **12**.

76. Stanton, M.M., et al., Magnetotactic Bacteria Powered Biohybrids Target E. coli Biofilms. ACS Nano, 2017. **11**(10): p. 9968-9978.

77. Felfoul, O., et al., Magneto-aerotactic bacteria deliver drug-containing nanoliposomes to tumour hypoxic regions. Nat Nanotechnol, 2016. **11**(11): p. 941-947.

78. Esquivel, D.M. and H.G.P. Lins de Barros, *Motion of magnetotactic microorganisms.* J Exp Biol, 1986. **121**: p. 153-163.

79. Maerkl, S.J. and S.R. Quake, A systems approach to measuring the binding energy landscapes of transcription factors. Science, 2007. **315**(5809): p. 233-7.

80. Vanapalli, S.A., et al., Microfluidic valves with integrated structured elastomeric membranes for reversible fluidic entrapment and in situ channel functionalization. Lab Chip, 2009. **9**(10): p. 1461-7.

81. Robinson, T., et al., Microfluidic trapping of giant unilamellar vesicles to study transport through a membrane pore. Biomicrofluidics, 2013. **7**(4): p. 44105.

82. Volpetti, F., J. Garcia-Cordero, and S.J. Maerkl, A microfluidic platform for high-throughput multiplexed protein quantitation. PLoS One, 2015. **10**(2): p. e0117744.

83. Ostapenko, T., et al., Curvature-Guided Motility of Microalgae in Geometric Confinement. Phys Rev Lett, 2018. **120**(6): p. 068002.

84. Narinder, N., J.R. Gomez-Solano, and C. Bechinger, Active particles in geometrically confined viscoelastic fluids. New Journal of Physics, 2019. **21**.

85. van Meer, B.J., et al., Small molecule absorption by PDMS in the context of drug response bioassays. Biochem Biophys Res Commun, 2017. **482**(2): p. 323-328.

86. Heo, Y.S., et al., Characterization and resolution of evaporation-mediated osmolality shifts that constrain microfluidic cell culture in poly(dimethylsiloxane) devices. Anal Chem, 2007. **79**(3): p. 1126-34.

87. Barber-Zucker, S., N. Keren-Khadmy, and R. Zarivach, From invagination to navigation: The story of magnetosome-associated proteins in magnetotactic bacteria. Protein Sci, 2016. **25**(2): p. 338-51.

88. Schuler, D. and E. Baeuerlein, Dynamics of iron uptake and Fe3O4 biomineralization during aerobic and microaerobic growth of Magnetospirillum gryphiswaldense. J Bacteriol, 1998. **180**(1): p. 159-62.

89. Komeili, A., et al., Magnetosome vesicles are present before magnetite formation, and MamA is required for their activation. Proc Natl Acad Sci U S A, 2004. **101**(11): p. 3839-44.

90. Staniland, S., et al., Rapid magnetosome formation shown by real-time x-ray magnetic circular dichroism. Proc Natl Acad Sci U S A, 2007. **104**(49): p. 19524-8.

91. Moisescu, C., et al., Iron Uptake Kinetics and Magnetosome Formation by Magnetospirillum gryphiswaldense as a Function of pH, Temperature and Dissolved Iron Availability. Geomicrobiology Journal, 2011. **28**(7): p. 590-600.

92. Moisescu, C., Ardelean, II, and L.G. Benning, The effect and role of environmental conditions on magnetosome synthesis. Front Microbiol, 2014. **5**: p. 49.

93. Woehl, T.J., et al., Correlative electron and fluorescence microscopy of magnetotactic bacteria in liquid: toward in vivo imaging. Sci Rep, 2014. **4**: p. 6854.

94. Firlar, E., et al., Investigation of the magnetosome biomineralization in magnetotactic bacteria using graphene liquid cell - transmission electron microscopy. Nanoscale, 2019. **11**(2): p. 698-705.

95. Reisz, J.A., et al., Effects of ionizing radiation on biological molecules--mechanisms of damage and emerging methods of detection. Antioxid Redox Signal, 2014. **21**(2): p. 260-92.

96. Hoang, M.V., H.J. Chung, and A. Elias, Irreversible bonding of polyimide and polydimethylsiloxane (PDMS) based on a thiol-epoxy click reaction. J Micromech Microeng, 2016. **26**.

97. Pushie, M.J., et al., Elemental and chemically specific X-ray fluorescence imaging of biological systems. Chem Rev, 2014. **114**(17): p. 8499-541.

98. Liu, Y., et al., New poly(amide-imide)s with trifluoromethyl and chloride substituents: Synthesis, thermal, dielectric, and optical properties. Eur Polym J, 2017. **94**: p. 392-404.

99. Conte, M., et al., Antimicrobial activity of various cationic molecules on foodborne pathogens. World J Microbiol Biotechnol, 2007. **23**(12): p. 1679-1683.

100. Colville, K., et al., Effects of poly(L-lysine) substrates on attached Escherichia coli bacteria. Langmuir, 2010. **26**(4): p. 2639-44.

101. Wang, Q., et al., Iron response regulator protein IrrB in Magnetospirillum gryphiswaldense MSR-1 helps control the iron/oxygen balance, oxidative stress tolerance, and magnetosome formation. Appl Environ Microbiol, 2015. **81**(23): p. 8044-53.

102. Olszewska-Widdrat, A., et al., Reducing Conditions Favor Magnetosome Production in Magnetospirillum magneticum AMB-1. Front Microbiol, 2019. **10**: p. 582.

103. Calugay, R.J., et al., Siderophore production by the magnetic bacterium Magnetospirillum magneticum AMB-1. FEMS Microbiol Lett, 2003. **218**(2): p. 371-5.

104. Fernandez-Castane, A., et al., Flow cytometry as a rapid analytical tool to determine physiological responses to changing O2 and iron concentration by Magnetospirillum gryphiswaldense strain MSR-1. Sci Rep, 2017. **7**(1): p. 13118.

105. Fernandez-Castane, A., et al., Development of a simple intensified fermentation strategy for growth of Magnetospirillum gryphiswaldense MSR-1: Physiological responses to changing environmental conditions. N Biotechnol, 2018. **46**: p. 22-30.

106. Hasinoff, B.B., The intracellular iron sensor calcein is catalytically oxidatively degraded by iron(II) in a hydrogen peroxide-dependent reaction. J Inorg Biochem, 2003. **95**(2-3): p. 157-64.

107. Amor, M., et al., Single-cell determination of iron content in magnetotactic bacteria: implications for the iron biogeochemical cycle. Environ Microbiol, 2019.

108. Thomas, F., et al., Calcein as a fluorescent probe for ferric iron. Application to iron nutrition in plant cells. J Biol Chem, 1999. **274**(19): p. 13375-83.

109. Teale, F.W.J. and G. Weber, Ultraviolet Fluorescence of the Aromatic Amino Acids. Biochem J, 1956. **65**(3): p. 476-482.

110. Estabrook, R.W., Fluorometric measurement of reduced pyridine nucleotide in cellular and subcellular particles. Anal Biochem, 1962. **4**: p. 231-45.

111. Eng, J., R.M. Lynch, and R.S. Balaban, Nicotinamide adenine dinucleotide fluorescence spectroscopy and imaging of isolated cardiac myocytes. Biophys J, 1989. **55**(4): p. 621-30.

112. Bessey, O.A., O.H. Lowry, and R.H. Love, The fluorometric measurement of the nucleotides of riboflavin and their concentration in tissues. J Biol Chem, 1949. **180**(2): p. 755-69.

113. Mihalcescu, I., et al., Green autofluorescence, a double edged monitoring tool for bacterial growth and activity in micro-plates. Phys Biol, 2015. **12**(6): p. 066016.

114. Ahmad, S. and G.S. Rao, EDTA: an alternative spectrophotometric reagent for iron estimation. J Anal Toxicol, 1997. **21**(2): p. 172-3.

115. Breuer, W., et al., Transport of iron and other transition metals into cells as revealed by a fluorescent probe. Am J Physiol, 1995. **268**(6 Pt 1): p. C1354-61.

116. Esteves, V.I., E.B. Santos, and A.C. Duarte, Study of the effect of pH, salinity and DOC on fluorescence of synthetic mixtures of freshwater and marine salts. J Environ Monit, 1999. **1**(3): p. 251-4.

117. Gachko, G.A., et al., Fluorescence quenching of tryptophan in aqueous solutions by pyruvate. Zhurnal Prikladnoi Spektroskopii, 1988. **47**(5): p. 748-753.

118. Peng, H.L. and R. Callender, Mechanism for Fluorescence Quenching of Tryptophan by Oxamate and Pyruvate: Conjugation and Solvation-Induced Photoinduced Electron Transfer. J Phys Chem B, 2018. **122**(25): p. 6483-6490.

119. Alphandery, E., et al., The effect of iron-chelating agents on Magnetospirillum magneticum strain AMB-1: stimulated growth and magnetosome production and improved magnetosome heating properties. Appl Microbiol Biotechnol, 2012. **96**(3): p. 663-70.

120. Shih, T.K., et al., Fabrication of PDMS (polydimethylsiloxane) microlens and diffuser using replica molding. Microelectronic Engineering, 2006. **83**(11-12): p. 2499-2503.

121. Sun, R., et al., Manufacturing PDMS micro lens array using spin coating under a multiphase system. J Micromech Microeng, 2017. **27**.

122. Pringsheim, P., *Fluorescence and Phosphorescence*. 1949, New York, N.Y.: Interscience Publishing Co.

123. Arik, M., N. Çelebi, and Y. Onganer, Fluorescence quenching of fluorescein with molecular oxygen in solution. J Photochem Photobiol A, 2005. **170**(2): p. 105-111.

124. Toepke, M.W. and D.J. Beebe, PDMS absorption of small molecules and consequences in microfluidic applications. Lab Chip, 2006. **6**(12): p. 1484-6.

125. Blume, I., et al., Vapour sorption and permeation properties of poly (dimethylsiloxane) films. Journal of Membrane Science, 1991. **61**: p. 85-97.

126. Cui, X., et al., Microfluidic long-term differential oxygenation for bacterial growth characteristics analyses. RSC Advances, 2014(32).

127. Ortiz-Acosta, D. and C. Densmore, Sylgard® Cure Inhibition Characterization. Los Alamos National Laboratory.

128. Collins, A.M., Chapter 5 - Physical Techniques, in Nanotechnology Cookbook. 2012. p. 205-253.

129. Lee, J.N., C. Park, and G.M. Whitesides, Solvent compatibility of poly(dimethylsiloxane)-based microfluidic devices. Anal Chem, 2003. **75**(23): p. 6544-54.

130. Regehr, K.J., et al., Biological implications of polydimethylsiloxane-based microfluidic cell culture. Lab Chip, 2009. **9**(15): p. 2132-9.

131. Halldorsson, S., et al., Advantages and challenges of microfluidic cell culture in polydimethylsiloxane devices. Biosens Bioelectron, 2015. **63**: p. 218-231.

132. Schirrer, R., P. Thepin, and G. Torres, Water absorption, swelling, rupture and salt release in salt-silicone rubber compounds. J Mater Sci, 1992. **27**: p. 3424-3434.

133. Tooley, W.W., et al., Thermal fracture of oxidized polydimethylsiloxane during soft lithography of nanopost arrays. J Micromech Microeng, 2011.

134. Akbarzadeh, A., et al., Liposome: classification, preparation, and applications. Nanoscale Res Lett, 2013. **8**(1): p. 102.

135. Balazs, D.A. and W. Godbey, Liposomes for use in gene delivery. J Drug Deliv, 2011. **2011**: p. 326497.

136. Dimova, R., Giant Vesicles and Their Use in Assays for Assessing Membrane Phase State, Curvature, Mechanics, and Electrical Properties. Annu Rev Biophys, 2019. **48**: p. 93-119.

137. Supramaniam, P., O. Ces, and A. Salehi-Reyhani, Microfluidics for Artificial Life: Techniques for Bottom-Up Synthetic Biology. Micromachines (Basel), 2019. **10**(5).

138. Elani, Y., et al., Constructing vesicle-based artificial cells with embedded living cells as organelle-like modules. Sci Rep, 2018. **8**(1): p. 4564.

139. Morita, M., K. Katoh, and N. Noda, Direct Observation of Bacterial Growth in Giant Unilamellar Vesicles: A Novel Tool for Bacterial Cultures. ChemistryOpen, 2018. **7**(11): p. 844.

140. Trantidou, T., et al., Functionalizing cell-mimetic giant vesicles with encapsulated bacterial biosensors. Interface Focus, 2018. **8**(5): p. 20180024.

141. Juskova, P., et al., "Basicles": Microbial Growth and Production Monitoring in Giant Lipid Vesicles. ACS Appl Mater Interfaces, 2019. **11**(38): p. 34698-34706.

142. Pautot, S., B.J. Frisken, and D.A. Weitz, Production of Unilamellar Vesicles Using an Inverted Emulsion. Langmuir, 2003. **19**: p. 2870-2879.

143. Rideau, E., et al., Liposomes and polymersomes: a comparative review towards cell mimicking. Chem Soc Rev, 2018. **47**(23): p. 8572-8610.

144. Reeves, J.P. and R.M. Dowben, Formation and properties of thin-walled phospholipid vesicles. J Cell Physiol, 1969. **73**(1): p. 49-60.

145. Meleard, P., L.A. Bagatolli, and T. Pott, Giant unilamellar vesicle electroformation from lipid mixtures to native membranes under physiological conditions. Methods Enzymol, 2009. **465**: p. 161-76.

146. Hu, P.C., S. Li, and N. Malmstadt, Microfluidic fabrication of asymmetric giant lipid vesicles. ACS Appl Mater Interfaces, 2011. **3**(5): p. 1434-40.

147. Arriaga, L.R., et al., Ultrathin shell double emulsion templated giant unilamellar lipid vesicles with controlled microdomain formation. Small, 2014. **10**(5): p. 950-6.

148. Miller, J.F., W.J. Dower, and L.S. Tompkins, High-voltage electroporation of bacteria: genetic transformation of Campylobacter jejuni with plasmid DNA. Proc Natl Acad Sci U S A, 1988. **85**(3): p. 856-60.

149. Moga, A., et al., Optimization of the Inverted Emulsion Method for High-Yield Production of Biomimetic Giant Unilamellar Vesicles. Chembiochem, 2019. **20**(20): p. 2674-2682.

150. Morita, M., K. Katoh, and N. Noda, Direct Observation of Bacterial Growth in Giant Unilamellar Vesicles: A Novel Tool for Bacterial Cultures. ChemistryOpen, 2018. **7**(11): p. 845-849.

151. Ma, C., et al., Effect of PVA Concentration on Structure and Performance of Precipitated Iron-Based Catalyst for Fischer-Tropsch Synthesis. J Braz Chem Soc, 2017. **28**(8).

152. Kunhle, J.A., R.E. Lundin, and A.C. Waiss, Photodecarboxylation of Dicarboxylic Acids in the Presence of Iron(III) Chloride. J.C.S. Chem. Comm., 1972.

153. Budac, D. and P. Wan, Photodecarboxylation: mechanism and synthetic utility. Photobiology A: Chemistry, 1992. **67**(2): p. 136-166.

154. Chen, J. and W.R. Browne, *Photochemistry of iron complexes.* Coordination Chemistry Reviews, 2018. **374**: p. 15-38.

155. Uebe, R., et al., Deletion of a fur-like gene affects iron homeostasis and magnetosome formation in Magnetospirillum gryphiswaldense. J Bacteriol, 2010. **192**(16): p. 4192-204.

156. Komeili, A., Molecular mechanisms of compartmentalization and biomineralization in magnetotactic bacteria. FEMS Microbiol Rev, 2012. **36**(1): p. 232-55.

157. Amor, M., et al., Iron uptake and magnetite biomineralization in themagnetotactic bacteriumMagnetospirillum magneticumstrain AMB-1: An iron isotope study. Geochimica et Cosmochimica Acta, 2018. **232**: p. 225-243.

158. Faivre, D., et al., Environmental parameters affect the physical properties of fast-growing magnetosomes. American Mineralogist, 2008. **93**: p. 463-469.

159. Vargas, G., et al., Applications of Magnetotactic Bacteria, Magnetosomes and Magnetosome Crystals in Biotechnology and Nanotechnology: Mini-Review. Molecules, 2018. **23**(10).